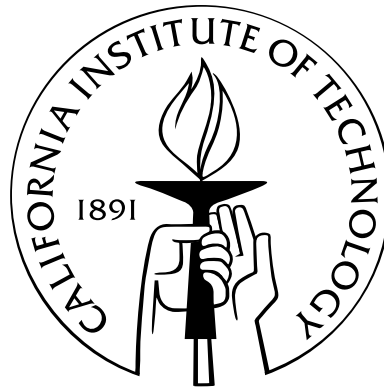


Axel Rover Tethered Dynamics and Motion Planning on Extreme Planetary Terrain

Thesis by
Pablo Abad-Manterola

In Partial Fulfillment of the Requirements
for the Degree of
Doctor of Philosophy



California Institute of Technology
Pasadena, California

2012

Defended July 8, 2011

© 2012

Pablo Abad-Manterola

All Rights Reserved

To my family.

Acknowledgements

This dissertation would be little longer than a title page were it not for the support and encouragement of all the friends and colleagues that I have been fortunate enough to spend my time with here at Caltech. First and foremost, I would like to express my most heartfelt gratitude to my mentors, Dr. Joel Burdick and Dr. Issa Nesnas, for giving me the opportunity to fulfill my childhood dream of designing, building, and testing extra-planetary robotic explorers.

I would also like to thank fellow graduate students Jeffrey Edlund, Melissa Tanner, Paul Hebert, and all members of the Burdick research group for their help and advice. Summers with *Axel* attracted many undergraduate students who helped with experiments and became good friends: Tom Oliver, Kevin Noertker, Johanna Cecava, Michelle Jiang, Nam Nguyen, Chun Che Peng, Albert Wu, Frankie Mangini, Kent Koyanagi, and Ruslan Kurdyumov.

It was truly a pleasure working with *Axel* as the project grew to draw from the diverse talents of the JPL community. The following people, *Axel* team members past and present, deserve much of the credit for the rover's recent and remarkable achievements: Jaret Matthews, Robert Peters, Jack Morrison, Benjamin Solish, Bob Anderson, Jack Dunkle, Srikanth Saripalli, Pan Conrad, and Robert Miyake. This research would not have been possible without a fellowship from the National Science Foundation, and I sincerely thank the NSF for sponsoring me while I worked on this project.

Finally, I am forever grateful for the support of my mother, my father, and my sister. For your love, your strength, and your sacrifices, I owe to you a debt that cannot be repaid in a single lifetime.

Thank you.

Abstract

Some of the most appealing science targets for future exploration missions in our solar system lie in terrains that are inaccessible to state-of-the-art robotic rovers such as NASA's *Opportunity*, thereby precluding in situ analysis of these rich opportunities. Examples of potential high-yield science areas on Mars include young gullies on sloped terrains, exposed layers of bedrock in the Victoria Crater, sources of methane gas near Martian volcanic ranges, and stepped delta formations in heavily cratered regions. In addition, a recently discovered cryovolcano on Titan and frozen water near the south pole of our own Moon could provide a wealth of knowledge to any robotic explorer capable of accessing these regions.

To address the challenge of extreme terrain exploration, this dissertation presents the *Axel* rover, a two-wheeled tethered robot capable of rappelling down steep slopes and traversing rocky terrain. *Axel* is part of a family of reconfigurable rovers, which, when docked, form a four-wheeled vehicle nicknamed *DuAxel*. *DuAxel* provides untethered mobility to regions of extreme terrain and serves as an anchor support for a single *Axel* when it undocks and rappels into low-ground.

Axel's performance on extreme terrain is primarily governed by three key system components: wheel design, tether control, and intelligent planning around obstacles. Investigations in wheel design and optimizing for extreme terrain resulted in the development of grouser wheels. Experiments demonstrated that these grouser wheels were very effective at surmounting obstacles, climbing rocks up to 90% of the wheel diameter. Terramechanics models supported by experiments showed that these wheels would not sink excessively or become trapped in deformable terrain.

Predicting tether forces in different configurations is also essential to the rover's mobility. Providing power, communication, and mobility forces, the tether is *Axel*'s lifeline while it rappels steep slopes, and a cut, abraded, or ruptured tether would result in an untimely end to the rover's mission. Understanding tether forces are therefore paramount, and this thesis both models and measures tension forces to predict and avoid high-stress scenarios.

Finally, incorporating autonomy into *Axel* is a unique challenge due to the complications that arise during tether management. Without intelligent planning, rappelling systems can easily become entangled around obstacles and suffer catastrophic failures. This motivates the development of a novel tethered planning algorithm, presented in this thesis, which is unique for rappelling systems.

Recent field experiments in natural extreme terrains on Earth demonstrate the *Axel* rover's potential as a candidate for future space operations. Both *DuAxel* and its rappelling counterpart are rigorously tested on a 20 meter escarpment and in the Arizona desert. Through analysis and experiments, this thesis provides the framework for a new generation of robotic explorers capable of accessing extreme planetary regions and potentially providing clues for life beyond Earth.

Contents

Acknowledgements	iv
Abstract	v
List of Figures	x
List of Tables	xiii
1 Introduction	1
1.1 A Brief History of Space Robotics	1
1.2 Future Science Targets	4
1.3 The Challenge of Robotic Operation in Extreme Terrain	9
1.4 A Survey of Extreme Terrain Rovers	10
1.5 Thesis Outline and Contributions	12
2 <i>Axel</i> Rover	13
2.1 Mission Architecture Trade-Offs	13
2.1.1 Mother-Daughter System	13
2.1.2 Single-Vehicle System	14
2.1.3 Multiple Mobile Assets	14
2.1.4 Multiple Fixed Assets	15
2.1.5 Architecture Selection	15
2.2 The <i>Axel</i> Concept	15
2.3 First-Generation <i>Axel</i> Prototype	17
2.3.1 Proof of Concept	17
2.3.2 Artificial Lunar Crater Tests	20
2.3.3 Long Traversals	22
3 Wheel Design	25
3.1 Cleated Wheels	25

3.2	Grouser Wheels	26
3.3	Analysis and Experiments	27
3.3.1	Obstacle Traversal	27
3.3.2	Sinkage	30
3.3.3	Efficiency	32
3.4	Paddle-Rim Wheels	35
4	Tethered Motion Planning	38
4.1	Related Work	38
4.2	Rover Dynamics	39
4.2.1	Euler-Lagrange Equations	40
4.2.2	Holonomic and Non-Holonomic Constraints	41
4.2.3	Non-Conservative Forces and the Power Dissipation Method	43
4.2.4	Application to <i>Axel</i>	45
4.3	Modeling Extreme Terrain	50
4.4	Obstacle Detection	51
4.5	Algorithm	54
4.5.1	Summary of the Problem	54
4.5.2	Ascent/Descent Approach	57
4.5.3	Ascent Path Planning	57
4.5.4	Homotopies of Ascending Paths	60
4.5.5	Constructing Anchor Reachable Sets	62
4.6	Simple Example	64
4.7	Shackleton Crater	67
5	Tether Tension Prediction	75
5.1	Tension on Steep Slopes	75
5.2	Climbing Precipices	79
5.3	Tension in the Field	81
6	<i>Axel 2</i> and <i>DuAxel</i>	84
6.1	<i>Axel 1</i> Shortcomings	84
6.2	Second-Generation <i>Axel</i> Prototype	85
6.3	The <i>DuAxel</i> Architecture	87
6.4	Extreme Terrain Field Tests	88
6.4.1	Vulcan Quarry	89
6.4.2	Arizona Desert	91

6.4.3	3D Terrain Scanning	95
7	Conclusion	98
7.1	Future Work	99
	Bibliography	102

List of Figures

1.1	Sojourner rover on Mars	3
1.2	New gully deposit in Mars' Centauri Montes region	5
1.3	New gully deposit in Mars' Terra Sirenum region	5
1.4	Cape St. Vincent, Victoria Crater, Mars	6
1.5	Stepped delta formations on the surface of Mars	7
1.6	Martian methane release	8
1.7	Evidence of a cryovolcano on Titan	8
2.1	Axel rover concept	16
2.2	Original Axel hardware	18
2.3	Proof-of-concept tests	18
2.4	Artificial lunar crater	21
2.5	Sampling on the artificial lunar crater	21
2.6	First-generation Axel prototype	23
2.7	Axel 1 traversing a rock	23
2.8	Axel 1 ascent/descent over simulated crater promontory	24
3.1	Axel with mountain bike tires	26
3.2	Axel with 5-grouser wheels	27
3.3	Circular wheel model traveling over rock	28
3.4	Grouser wheel model traveling over rock	29
3.5	Submerged flat plate from Bekker model	31
3.6	Wheel sinkage diagrams	32
3.7	Grouser wheel sinkage data	33
3.8	Grouser wheel and bike tire comparison: power vs time	34
3.9	Grouser wheel and bike tire comparison: energy consumption vs speed	34
3.10	Paddle-rim wheel design	35
3.11	Paddle-rim wheel traversing a rock	36
3.12	Paddle-rim wheel efficiency data	36

4.1	Axel model	46
4.2	LRO Shackleton crater data	50
4.3	Shackleton crater 3-plane model	51
4.4	Compatible points	53
4.5	Shallow terrain obstacle detection	55
4.6	Steep terrain obstacle detection	56
4.7	Ascent problem schematic	58
4.8	Algorithm pseudo-code	59
4.9	Boundary triangulated 2-manifold	61
4.10	Sleeve construction	62
4.11	BTM with sleeves	63
4.12	Discretized sleeve	64
4.13	Example: terrain model	65
4.14	Example: reachable sets	66
4.15	Example: boundary triangulated manifold	66
4.16	Shackleton crater obstacles	68
4.17	Shackleton BTM	70
4.18	BTM details	71
4.19	Sleeve examples	72
4.20	Shackleton reachable sets	73
4.21	Reachable sets with varying traction	74
5.1	Tethered Axel on a slope free-body diagram	76
5.2	Theoretical tether tension	77
5.3	Tether tension data overlaid on theoretical model	78
5.4	Axel climbing a ledge	79
5.5	Tension and torque climbing a ledge	80
5.6	Tether tension vs anchor point height	81
5.7	Descent tension data	82
6.1	Axel 2	85
6.2	Instrument module	86
6.3	DuAxel CAD rendering and prototype	87
6.4	DuAxel in rappelling mode	88
6.5	Vulcan quarry descent	90
6.6	Leg deployment mechanism	91
6.7	DuAxel on rough terrain	92

6.8	Arizona, day 1	92
6.9	Arizona, day 2	93
6.10	Tether snagging in the field	94
6.11	Riegl 3D laser scanner	95
6.12	3D scanner data	96
6.13	2D scanner data	96

List of Tables

2.1	Untethered maximum energy cost	19
5.1	Static tether tension experiments	78

Chapter 1

Introduction

This thesis details the design and development of a new extreme terrain rover prototype named *Axel*. *Axel* is a minimalistic robot designed to explore hard-to-reach regions on the Moon and Mars. The rover employs a tether to rappel down steep terrain using mobility akin to a yo-yo. Early proof-of-concept tests conducted at the Jet Propulsion Laboratory (JPL) are discussed, noting changes and improvements which eventually led to extreme-environment testing in the Arizona desert. This thesis evaluates the rover's performance by measuring efficiency, sinkage, and its ability to traverse obstacles. Later chapters also discuss modeling steep-terrain rover dynamics with holonomic tether constraints, and outline a new algorithm for tethered motion planning. The work presented in this thesis lays the foundation for a new generation of robotic explorers capable of operating autonomously on steep terrain and providing access to previously unreachable regions in our solar system, which could eventually lead to groundbreaking scientific discoveries.

1.1 A Brief History of Space Robotics

The first man-made satellite, *Sputnik 1*, reached Earth orbit on October 4th, 1957, marking a major milestone in human history and ushering in the dawn of the Space Age. The event shocked the world and sparked a political panic in the United States, which responded by establishing the National Aeronautics and Space Administration (NASA) in 1958. Motivated by the fear of falling behind the Soviet Union, the United States deployed its own satellite, *Explorer 1*, within four months of the *Sputnik* launch. The Space Race had begun.

In the years that followed, the competition between the United States and the Soviet Union led to rapid developments in both the technology that was launched into space and the rockets needed to deploy it. While *Sputnik 1* carried only two simple radio transmitters, *Sputnik 3*, which launched only 6 months later, carried twelve instruments measuring, among other things, magnetic fields and the composition of the Earth's upper atmosphere. Future iterations of both Russian and American satellites quickly became more sophisticated until the early 1960s, when President John F. Kennedy

redefined the ultimate goal of the Space Race to be the “landing of a man on the Moon and returning him safely to Earth.”

To achieve this goal, NASA employed the Jet Propulsion Laboratory to survey the Moon and engineer unmanned missions designed to test the feasibility of soft landings. Beginning with the *Ranger* program in 1961, unmanned impact vehicles *Rangers 1-6* attempted to obtain close-up photographic images of the moon before crashing onto the surface. These first six vehicles failed, however, and it wasn't until *Ranger 7* in 1964 that JPL successfully received its first near-Moon pictures.

The *Surveyor* program, started in 1966, represents the beginning of American space robotics. The first vehicle, *Surveyor 1*, successfully traveled to the Moon and decelerated just before impact in order to come to rest carefully on the surface. In addition to proving the feasibility of lunar landings, the *Surveyor* spacecraft tested critical engineering challenges such as descent guidance, control, and engine throttling. Several *Surveyor* missions also carried robotic shovels designed to test the consistency of the Moon's regolith¹. Seven *Surveyor* vehicles (five of them successful) paved the way for NASA's manned *Apollo* missions. Following the path laid out by these robotic pioneers, Neil Armstrong, on July 20th, 1969, stepped off the *Eagle* and onto the Moon, becoming the first human to set foot on the lunar surface.

Five subsequent *Apollo* missions successfully landed astronauts on the Moon, ending with *Apollo 17* in 1972. With the Space Race to the Moon at an end, the Soviet Union shifted its focus to the design and manufacture of orbital space stations. Manned missions to the Moon, after all, proved to be both expensive and dangerous. At the same time, NASA began development of a reusable orbital spacecraft known as the Space Shuttle, and it also pioneered space exploration beyond Earth.

Bolstered by the technical expertise gained during the successes and failures of the 1960s, JPL engineered a variety of robotic spacecraft to investigate the planets, moons, asteroids, and comets of our solar system. The *Pioneer 10* and *11* vehicles explored the outer planets and eventually left the solar system. *Vikings 1* and *2* launched in 1975, both successfully deployed landers on the surface of Mars. Launched in 1989, *Magellan* and *Galileo* studied Venus and Jupiter, respectively. In 1997, *Cassini-Huygens* departed Earth to explore the ringed planet Saturn and its many moons. Two years later, the *Stardust* space probe began its mission to collect and send back samples from the comet Wild 2.

1997 marked another milestone for NASA/JPL when it successfully landed the first roving vehicle on another planet. Although the Soviet Union had already managed to send rovers to the Moon in the 1970s, it twice failed to land rovers on Mars. The 1997 NASA/JPL mission, designated Mars *Pathfinder*, consisted of a lander carrying a small six-wheeled robotic rover nicknamed

¹*Regolith* is defined as a layer of loose, heterogeneous material covering solid bedrock. It is commonly used as a synonym for lunar dust.



Figure 1.1: *Sojourner* rover on Mars

Sojourner (Figure 1.1). The rover operated for 83 sols², during which time it took over 500 pictures and conducted chemical composition analysis of several sites around the lander using an on-board spectrometer. The rover also tested new surface navigation algorithms and demonstrated the performance of the rocker-bogie³ mobility architecture.

Building upon the success of the Mars *Pathfinder* Mission, NASA/JPL built two more robotic rovers, the *Spirit* and *Opportunity*, as part of the Mars *Exploration* Rover (MER) mission [1]. The primary goal of this mission was to search among Martian rocks and soil for clues of past water activity on the Red Planet.

Landing on Mars in January of 2004, the twin MERs were not expected to last more than 90 sols due to anticipated dust coverage of the solar panels. The Martian wind, however, frequently blew dust off the rovers during what were called “cleaning events”. As a result, NASA/JPL extended the mission lifespan. In May of 2009, however, the *Spirit* rover became trapped in a patch of soft soil. Unable to move and adjust the tilt of the solar panels, *Spirit* could not effectively recharge its batteries, and the rover sent its last communication to Earth on March 22, 2010, after 2,210 sols of operation.

The *Opportunity* rover, on the other hand, continues its exploration of Mars to this day. As of June 1st, 2011, *Opportunity* has traveled over 30 km throughout its journey on the Red Planet [1]. Together with *Spirit*, the twin MERs have collected a vast amount of scientific data on the geology of Mars, bringing us closer to determining whether or not life could ever have existed outside of Earth.

Despite their sophistication, neither *Spirit* nor *Opportunity* actually carried the scientific instruments necessary to detect the organic compounds characteristic of life. To address this and learn

²A *sol* is a Mars solar day. It has a mean period of 24 hours 39 minutes 35.244 seconds, roughly 3% longer than an Earth solar day [13].

³The rocker-bogie suspension architecture consists of two rows of three wheels in parallel. Two wheels on each side of the suspension are connected to each other and can “rock” back and forth relative to the chassis. The third wheel is the drive wheel on each side of the suspension, referred to as the “bogie” (Figure 1.1).

more about the possibility of life on Mars, NASA/JPL plans to deploy the robotic rover *Curiosity* as part of the Mars Science Laboratory (MSL) mission [2]. Scheduled for launch in November of 2011, *Curiosity* will carry more than ten times the weight of scientific instruments than those carried by the MER rovers [62]. The rover will be expected to operate for at least a full Martian year (668 sols), and it will have the capability to travel a greater distance than any previous Mars rover.

While a human astronaut on Mars might be able to provide more insight and conduct more scientific experiments than a robotic rover, there are many safety concerns associated with human space travel. Specifically, humans traveling in space require life-support systems, are adversely affected by microgravity, are susceptible to radiation, and suffer from depression and other psychological problems during long missions confined in small spaces. Furthermore, transporting humans to the surface of Mars would require new entry, descent, and landing technology capable of safely delivering travelers within close proximity (tens of meters) of pre-deployed support systems [23]. The safety concerns, in addition to the high cost of developing new human transportation technology, make robots better suited for space exploration. However, given that a soft patch of soil proved enough to trap *Spirit*, a new generation of robust robotic rovers will be needed in order to explore the more challenging terrains found in our solar system and provide clues for life beyond Earth.

1.2 Future Science Targets

Some of the most appealing science targets for future exploration missions in our solar system lie in terrains that are inaccessible to state-of-the-art robotic rovers such as NASA's MER and MSL vehicles, thereby precluding in situ analysis of these rich opportunities. A few potential science opportunities are summarized below.

Between 1999 and 2000, the Mars Global *Surveyor's* Mars Orbiter Camera (MOC) detected youthful gullies on sloped terrains found on Mars' middle and high latitudes. The gullies appeared so young, in fact, that scientists hypothesized some were still active. To test this hypothesis, engineers at JPL directed the MOC to re-examine the gullies during the spring and summer of 2005, and they discovered two separate light-toned deposits that had not been present 5 years earlier. Specifically, unnamed craters in the Centauri Montes (Figure 1.2) and Terra Sirenum (Figure 1.3) regions revealed deposits approximately 20 percent brighter than the surface previously imaged in 1999, and the deposits exhibited characteristics consistent with liquid water transporting fine-grained sediment [3, 4]. Together, the new deposits discovered by the MOC confirm the presence of active geologic flows on Mars, but while they hint at the possibility of liquid water sources beneath the surface, the evidence is not conclusive. In order to better understand these deposits, it is necessary to sample them directly at their source, which requires the development of new robotic technologies capable of accessing these areas.

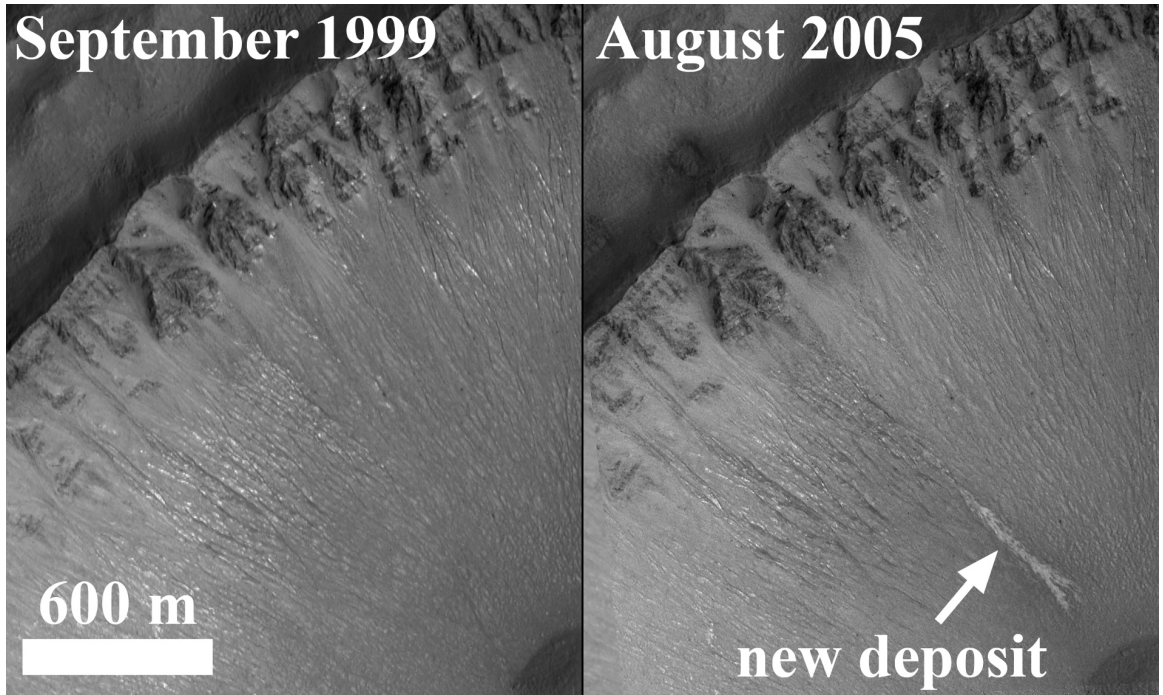


Figure 1.2: Photos from the MOC show a new gully deposit in an unnamed crater in the Centauri Montes region of Mars.

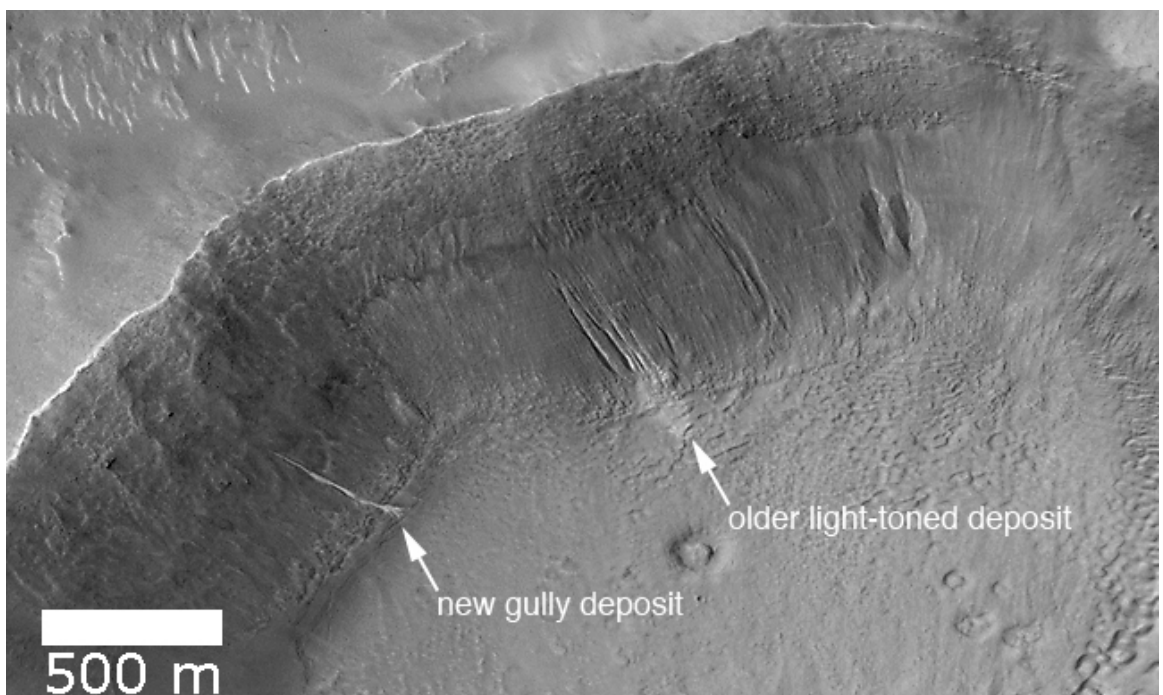


Figure 1.3: Picture from the MOC shows a a new gully deposit in an unnamed crater in the Terra Sirenum region.

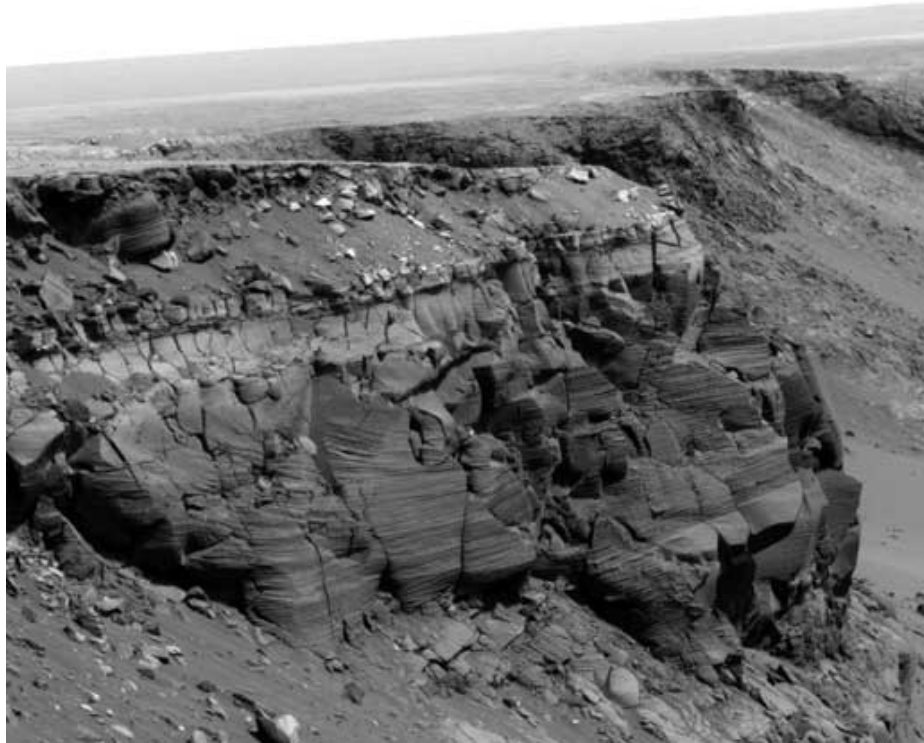


Figure 1.4: Picture taken by the *Opportunity* rover shows exposed layers of bedrock in Cape St. Vincent, Victoria Crater, Mars.

The *Opportunity* rover discovered exposed layers of bedrock in Cape St. Vincent, part of Mars' Victoria Crater (Figure 1.4) [5]. If studied closely, the bedrock layers can be read like the pages in a book, revealing the geologic history of the Red Planet.

The Thermal Emission Imaging System (THEMIS) mounted aboard NASA's 2001 Mars *Odyssey* robotic orbiter captured high-resolution images of stepped delta formations on the surface of Mars (Figure 1.5). Experiments reproducing the observed morphology of these deltas suggest that they formed after water released suddenly from underground reservoirs [39]. Taking measurements and samples at the site of these stepped deltas might provide a wealth of information about the history of water on Mars.

In 2003, scientists detected substantial plumes of methane in the northern hemisphere of Mars (Figure 1.6). Methane, however, survives only a few years in the Martian atmosphere, and so this discovery hints at a still-active chemical process. On Earth, most of the methane release is a by-product of the reactions that occur when organisms digest nutrients. But other purely geological processes, like iron oxidation, also release methane. While the source of the Martian methane remains unknown, it is possible that it comes from microscopic life residing far below the surface, where the warmer temperature may provide a safe haven for liquid water [59]. One of the primary goals of the MSL mission is to take precision measurements of the methane in order to distinguish between a

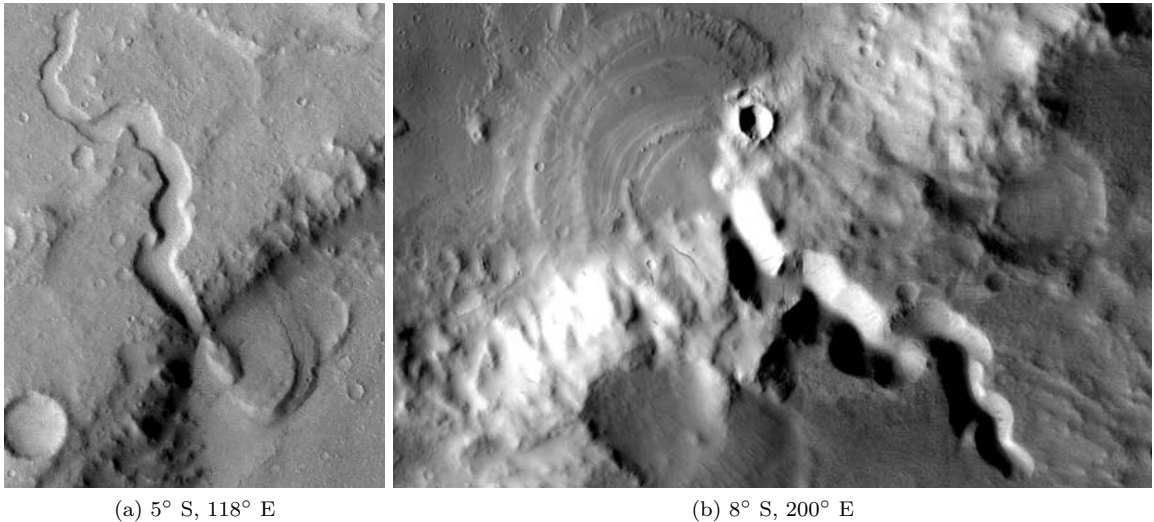


Figure 1.5: THEMIS images show examples of stepped delta formations in two separate Martian craters, which likely formed after a sudden liquid release from an underground reservoir. Martian latitude and longitude for each crater is given.

geochemical and a biological origin. Peak emissions of the gas, however, fall over the regions known as Tharsis, Arabia Terra, and Elysium. Tharsis is home to the solar system's largest known volcano, Olympus Mons, which is three times as tall as Mount Everest. Arabia Terra is densely cratered, and the volcanic rise known as Elysium is also the site of several volcanoes [15]. Traversing these areas and accessing the source of the methane plumes will be an important objective for future Mars rovers.

Methane gas was also detected by the *Cassini-Huygens* probe in the lower atmosphere of Saturn's largest moon, Titan [52]. Before *Cassini-Huygens*, scientists believed that the most likely source of this methane was the large hydrocarbon ocean. A recent flyby of the Sotra Facula region of Titan, however, revealed evidence of an ice volcano, or cryovolcano, which could also be the source of the methane gas (Figure 1.7). *Cassini-Huygens* detected two peaks, each more than 1,000 meters tall, and several craters as deep as 1,500 meters. Scientists hypothesize that the cryovolcanic ejecta could be a mixture of methane and water ice, but its exact nature will be impossible to determine without on-the-ground measurements [38].

In 2009, NASA launched the Lunar Crater Observation and Sensing Satellite (LCROSS). After sending a projectile to impact the Moon's surface, LCROSS analyzed the ejected debris and detected water ice in a permanently shadowed region of the Cabeus crater, located near the Moon's south pole [22]. This water will be a critical resource for future manned missions and extended human operations on the lunar surface. The exact quantity and extractability of these water ice reservoirs remains uncertain, however, and a robotic rover, capable of accessing the dark and cold regions deep within the craters, would allow NASA engineers to determine the viability of future lunar colonies.

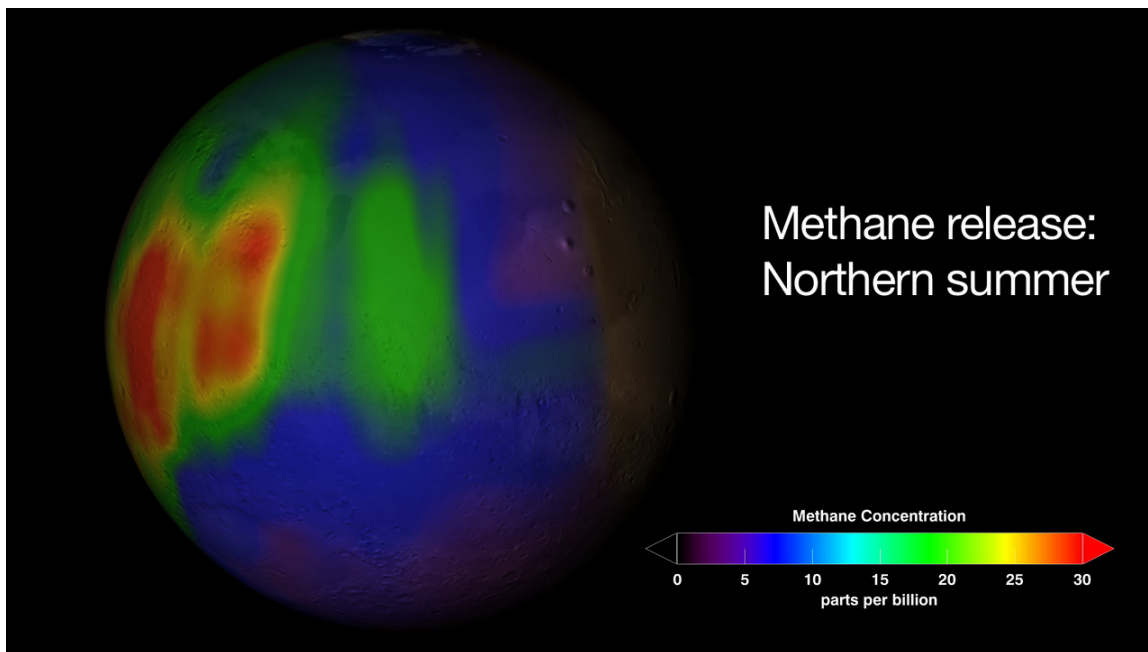


Figure 1.6: Martian methane release detected in January of 2009

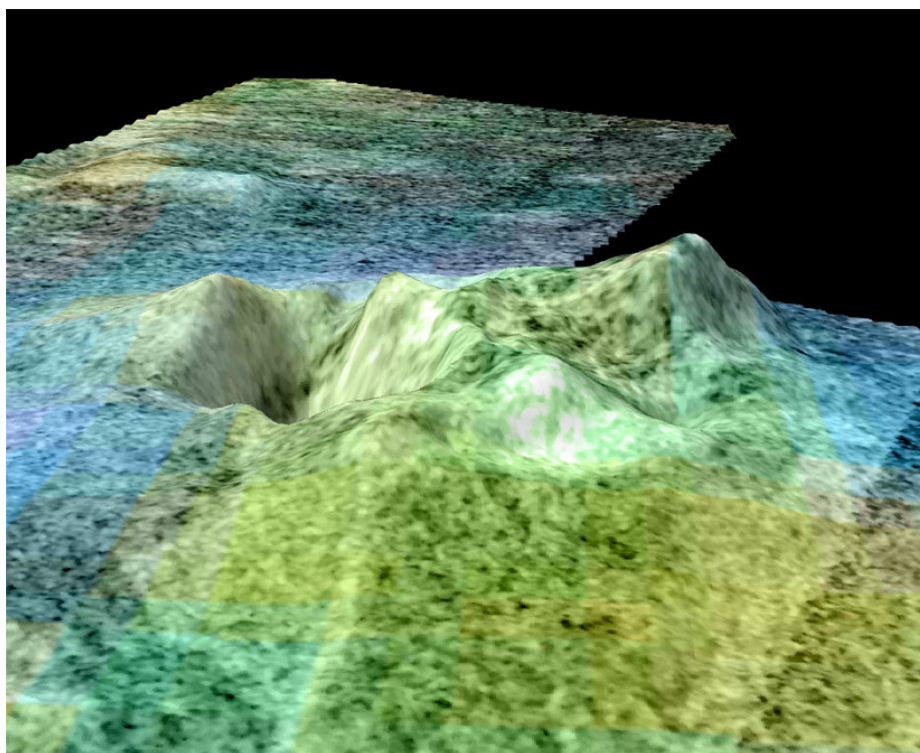


Figure 1.7: Image based on data from NASA's Cassini spacecraft shows what scientists believe to be a cryovolcano on the surface of Saturn's largest moon, Titan. Topography has been vertically exaggerated by a factor of 10.

Any of the aforementioned locations would serve as an excellent target for future robotic missions. Unfortunately, in space exploration, targets yielding greater science almost always correlate with greater risk, which forces NASA/JPL to perform a careful balancing act between a mission's safety, cost, and its science return. There are still many unsolved engineering challenges associated with operating a rover over rugged terrain in and around craters, canyons, and cryovolcanoes. By addressing these challenges, it is possible to reduce the risk of operating in extreme terrain and access the most scientifically promising regions in our solar system.

1.3 The Challenge of Robotic Operation in Extreme Terrain

Most robotic rover technology has been designed to explore rocky but relatively flat regions of planetary surfaces, and it is not intended for terrains such as deep craters, canyons, fissures, gullies, and cryovolcanoes. As outlined in Section 1.2, however, there are many scientific objectives out of reach of current state-of-the-art rovers, located in what is called *extreme terrain*. Extreme terrain is defined as terrain having one or more of the following characteristics: steep slopes, loose soil, tall precipices, lack of direct sunlight, and extreme cold.

Steep slopes and loose soil, as can be seen in Mars' Victoria crater (Figure 1.4), reduce the traction forces the rover can generate, greatly decreasing the terrain's traversability. Using the conventional rocker-bogie rover architecture present on the *Sojourner*, MER, and MSL rovers, slip can increase significantly on steep grades and certain areas become inaccessible.

Another characteristic of extreme terrain, tall precipices pose a significant danger to rovers. On rugged and collapsible regions, robotic explorers could accidentally fall dozens or hundreds of meters. Even in low-gravity environments such as on Mars and the Moon, a large drop could severely damage the rover. Rovers operating on extreme terrain should therefore be robust and capable of descending safely over tall precipices.

Additionally, rovers traversing steep and rugged terrain are at a higher risk of tip-over. In 1992, the eight-legged walking robot *Dante II* successfully descended into Alaska's Mt. Spurr volcano using a winch-cable system [18]. On the ascent trip, however, the rover fell on its side under the influence of large lateral tether forces and was unable to right itself. Extreme terrain rovers can reduce the risk of tip-over by lowering the center of mass and planning safe routes around obstacles. Alternatively, one could design a rover capable of operating in a vertical or upside-down configuration, thereby eliminating the dangers of tip-over altogether. Wind, slippery ice, loose rocks, and many other environmental factors can cause tip-over, and since these variables cannot be controlled, tip-over needs to be taken into consideration when designing an extreme terrain rover. More generally, robotic mobility engineering for extreme terrain must combine both novel mechanical design features and active planning and control algorithms.

Extreme terrain is also characterized by limited access to sources of energy due to lack of direct sunlight. For example, the Cabeus crater, described in Section 1.2, is located near the Moon's south pole and therefore lies in almost perpetual darkness, precluding the use of solar power. Even if the crater did have consistent access to sunlight, cold-traps like caves and crevices along the crater's walls would still be very difficult to investigate for prolonged periods of time. Rough terrain consisting of tall peaks and deep craters or canyons naturally restricts the passage of sunlight, and rovers hoping to explore these regions must be able to survive on a limited energy budget. Such terrains also present challenges for Earth-based communications with the rover, especially in the absence of an orbiting communication satellite.

Finally, a problem that is unique to robots exploring in cold regions is heat dissipation. In addition to traditional vehicle engineering in ultra-cold climates, robotic explorers designed for these environments must minimize thermal pollution to nearby terrain so as not to affect the scientific analysis of volatile components.

1.4 A Survey of Extreme Terrain Rovers

The development of robots that can traverse rough and steep terrain is not a new subject, and many prior efforts have contributed to the current understanding of the potential strategies for extreme terrain robotic mobility. Both legged and wheeled robots, as well as tethered and untethered robots, have been proposed for exploring extreme terrestrial and planetary terrains, several of which have been built and fielded. The *Dante II* robot [18] was a tethered legged concept specifically engineered to descend into active volcanoes. The *Athlete* robot is a combination wheel and legged robot designed to handle cargo in support of sustained human presence on the moon. It was also demonstrated traversing rocky and sloped terrain at a number of analog sites in California and Arizona, including Black Point Lava Flow [65]. For slopes greater than 20° , however, *Athlete* would require a tether. Other robots have been proposed that would use leg-mounted active anchors in lieu of tethers [17]. In either case, the inherent complexity that arises from large numbers of actuators needed by a capable multi-legged rover has greater potential for mission failure, particularly on very steep terrains. Moreover, typical power and mass constraints of space systems and the extreme thermal environment of cold traps make the engineering of leg actuators, sensors, and electrical harnesses for sustained operation in such an environment daunting at best.

In addition to these legged robots, a number of wheeled robots have also been proposed and several prototypes have been built and fielded. A recurring mechanism configuration uses a four-wheeled rocker suspension or a scissor-like active suspension that can lift each wheel independently off the ground. Such platforms were designed to control/lower the center of mass to provide great stability. One such example is a grapefruit sized rover, dubbed *Nanorover*, that was proposed for

exploring the surface of an asteroid [64]. This rover had a symmetric design and was capable of operating in an upside-down configuration. It actively controlled its center and was even capable of hopping on low-gravity bodies. Follow-on to this work also included the possibility of tethering the *Nanorover* to a *Sojourner* class rover for future Mars missions.

An architecturally similar rover is the *Scarab* rover, which demonstrated an inch-worming maneuver that synchronized wheel and suspension mechanism motion to traverse high-slip terrains [19]. Despite this ability to overcome high slip on slopes, steeper slopes are likely to require an external force, such as the one generated from the use of a tether. A tether, for example, could pull out a rover ensnared in sand at the bottom of a crater.

A robotic system developed at JPL, *Cliffbot*, demonstrated the capability of a four-wheeled tethered rover design [55]. This architecture required a minimum of three rovers. Two rovers would traverse the rim of the crater while a third rover, which was tethered to the other two, would descend into the crater. Lateral mobility with two tethers would generally be greater at a close distance to the rim, but this advantage diminishes as the rover descends deeper into the crater. The *Cliffbot* used the rim rovers to manage the tethers, which, unlike rovers that pay out their own tether, risks higher abrasion as the tether constantly scrapes the rocks. Moreover, *Cliffbot* cannot recover from tip-over, and the problem of planning the motions of two tethers adds extra complexity.

In addition to these four-wheeled rovers, a number of previous efforts have recognized the potential of two-wheel rovers for steep terrains. Several of these efforts have converged on a robotic body morphology consisting of a simple axial body with two wheels and a caster. Such designs appeared as far back as the early seventies. More recent morphologies include the *Scout* [60] robots that were eventually adapted for military applications. A similar tethered rover with three large inflatable wheels was proposed for future Mars missions [44].

The family of *Axel* rovers was initially developed at the turn of the century to provide modularity and separation between the mobility elements that are more likely to fail and the science payloads carried by the mobility elements [50, 36]. In 2006 the original *Axel* rover was retrofitted with a tether and adapted for extreme terrain mobility on slopes [51]. With its symmetric design, such a configuration demonstrated potential for robust and flexible mobility and operations on challenging terrain (see Chapter 2). Its single tether was managed by the same mechanism that controls the caster arm and the instrument orientation. The *Cesar* rover, which was motivated in part by the *Axel* concept, had a similar configuration to the untethered version of *Axel* and has demonstrated versatile mobility over a range of terrains [24]. Some of the unique characteristics of *Axel* include its caster link that can rotate continuously around its body, serving multiple purposes: tether management, instrument pointing, and straight line mobility as an alternate to driving the wheels, which could be valuable in case of a wheel actuator failure. The *Axel* concept can be extended to a *DuAxel* configuration (Chapter 6), where an *Axel* docks and undocks with a central module, enabling

both untethered mobility away from landers and towards the extreme terrains, and tethered mobility within a crater. *Axel* also has high-mobility grouser wheels, and later versions of *Axel* added a degree of freedom to decouple body pitch from tether management to enable instrument suite reorientation while hanging from a tether. Recent versions also included improved tether management and tether tension sensing.

1.5 Thesis Outline and Contributions

This thesis is organized as follows. Chapter 1 provides background and motivation, Chapter 2 summarizes different mission architectures for extreme terrain and outlines the development of the *Axel* rover, and Chapter 3 details the design of *Axel*'s grouser wheels for extreme terrain and evaluates their performance. Chapter 4 models the rover's dynamics and details a new motion planning algorithm for navigating extreme terrain with a tether. Chapter 5 analyzes the forces experienced by the tether, Chapter 6 presents the second generation *Axel* prototype and the *DuAxel* concept, and Chapter 7 provides concluding statements.

The thesis' contributions are: 1) details on the design of a new extreme terrain rover concept named *Axel*, 2) evaluation of the rover's performance during experiments conducted at JPL and in rough terrains, 3) modeling of the rover's dynamics, including holonomic inequality tether constraints, and 4) a novel motion planning algorithm for tethered rovers operating on extreme terrain.

Chapter 2

Axel Rover

This chapter examines the trade-offs between different mission architectures for exploration of extreme planetary terrains. The analysis is used to provide the justification for a single-axle tethered rover concept to provide access to science targets located in extreme terrain regions. Following the single-axle concept, the development of the first-generation *Axel* prototype is described, along with field experiments that test and validate the rover.

2.1 Mission Architecture Trade-Offs

Missions to extreme terrain can vary greatly in their objectives. Examples of potential exploration missions in our solar system include:

- the collection of measurements from flat, sloped, rough, and high-slip terrains,
- acquiring measurements of layered stratigraphy along multiple transects,
- and sustained exploration of low ground, such as a cold trap or crater floor.

The analysis in this section examines the trade-offs of various approaches attempting to fulfill the preceding objectives. It assumes a solar-powered surface exploration mission and does not consider mission architectures that have access to a nuclear power source.

2.1.1 Mother-Daughter System

The phrase mother-daughter describes systems comprised of a mother-ship that lands and explores moderate terrain and high ground, and one or more daughter-ships that explore extreme surface features and the low ground, e.g., craters. By leveraging assets on the mother-ship (such as energy sources, long-range communication, and on-board scientific analysis systems), the daughter-ship can be made lighter and simpler, and multiple daughter-ships can explore areas in parallel. A daughter-ship would often require a tether for two reasons: 1) the daughter-ship requires mechanical support

(i.e., an anchoring point) in order to descend into unknown and challenging terrain, and 2) the daughter-ship needs a source for power and communication in permanently shadowed areas.

The benefit of this architecture is that multiple daughter-ships can leverage the mother-ship's infrastructure for power generation and Earth communication, thus limiting the cost incurred by additional daughter-ships. Furthermore, multiple daughter-ships provide redundancy, lowering the risk of mission failure. On the other hand, this approach requires management of kilometers of tether over unknown terrain and has a higher risk if the daughter is relied upon to achieve the mission's minimum scientific requirements.

Within the mother-daughter mission architecture, there are two further options: 1) both the mother and the daughter are mobile, and 2) the mother is fixed while the daughter is mobile. The first option offers more flexibility for finding locations with good access to solar energy and optimizing communication to Earth. Although the second option enables a somewhat simpler design, the mission would require pin-point landing with a landing uncertainty ellipse in the hundreds of meters, and the daughter-ship would be limited to exploring an area around the mother constrained by the length of the tether. The first option, where the mother would carry the daughter to the edge of the extreme terrain, would only require precision landing with an uncertainty ellipse of several kilometers.

2.1.2 Single-Vehicle System

While a single-vehicle system can potentially explore both high and low ground, such a vehicle must be able to self-anchor and descend into a crater. In order to sustain exploration of permanently shadowed regions, the vehicle's anchor would also have to provide power and communication. The single-vehicle system would benefit from a tether for the same reasons listed in Section 2.1.1.

The single-vehicle architecture is arguably both simpler and cheaper than a mother-daughter system. However, self-anchoring increases mission risk, and without an ultra-reliable de-anchoring mechanism, a single vehicle will be limited to only a few crater descents. Furthermore, this mission concept does not readily incorporate the redundancy afforded by multiple vehicles to reduce overall mission risk.

2.1.3 Multiple Mobile Assets

Consider a system comprised of mobile assets (as few as three and up to around half a dozen), each loaded with an identical science package. These assets arrive at the surface either (a) via a single lander, where they disperse and explore in multiple directions, or (b) are deposited at disparate points via the landing system. By dividing up the exploration task, each mobility asset need only cover a portion of the targeted surface area.

Multiple mobile assets can survey a large area in a relatively short period of time. Asset redundancy reduces mission risk and lowers the manufacturing cost of each unit. However, the system's overall mass increases since each asset requires its own power, science, and communication equipment. Furthermore, high redundancy results in an increased operational cost, and each asset would require a smaller, lower performance instrument package.

2.1.4 Multiple Fixed Assets

With multiple fixed assets, a large number (e.g., in the tens) of non-mobile units would be delivered to the planetary surface in order to acquire measurements at disparate locations. These fixed assets can potentially sample large areas quickly, are robust to terrain challenges, and afford a large amount of redundancy to reduce mission risk. However, fixed assets would be limited to collecting measurements at discrete locations and would require a smaller, lower-cost (and lower performance) instrument package, limiting the science that could be performed. Assembling many explorers increases the mission's cost and mass, and the assets would have to survive very high impacts when being deployed. The landing itself would have to be very precise, requiring pin-point landing, and deployment could contaminate a considerable area around the lander, potentially polluting the scientific measurements.

2.1.5 Architecture Selection

Given the design constraints mentioned in Section 1.3, the jointly mobile mother-daughter system appears to offer the most benefits with the fewest drawbacks. While crater access adds significant risk to the mission concept, this risk can be minimized by using multiple daughter-ships. The large mother-ship provides mechanical support to the daughter, and it can be located in sunlit areas to supply power and relay communications from the low-ground exploration rover. Scientific instruments can be distributed between the mother and daughter, with the mother carrying larger, more expensive instruments and the daughter carrying smaller devices capable of functioning in more extreme environments. This approach appears to maximize scientific return while at the same time reducing mission risk and minimizing cost and mass.

2.2 The *Axel* Concept

In order to provide access and in situ sampling in extreme terrains, JPL and the California Institute of Technology (Caltech) have collaborated to develop the *Axel* rover [51, 10]. For extreme terrain exploration, the *Axel* rover is conceptualized as a mobile daughter-ship that could work with different mother-ship designs, thereby enabling *Axel* to serve as a potential component in a diverse range of missions.

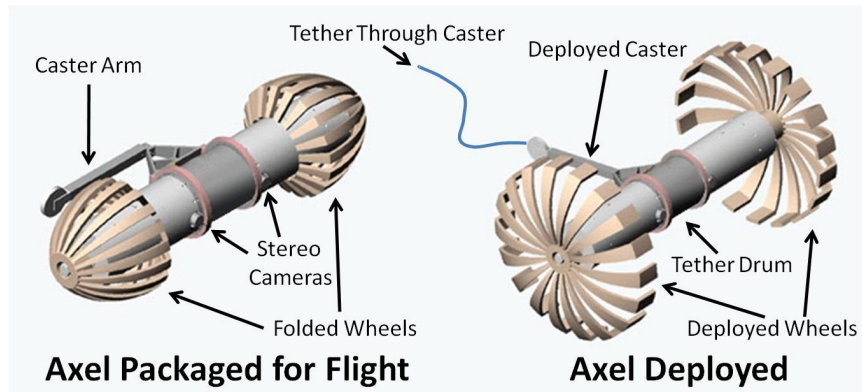


Figure 2.1: The *Axel* rover concept in a stowed configuration packaged for flight (left) and in a deployed configuration (right)

Axel embodies a rappelling robot concept that is designed to operate in extreme terrain via the use of a mother anchor platform. The minimalistic *Axel* rover consists of two wheels connected by a central cylindrical body (from which *Axel* derives its name), a caster arm, and an actively controlled tether passing through the caster arm. In addition to controlling the tether, the caster arm provides a reaction force against the terrain needed to generate forward motion when traveling on flat ground. Figure 2.1 shows a versatile *Axel* rover concept, which can be stowed to conserve volume during transport and then deployed for full functionality. Since *Axel*'s body acts as a winch (the tether is wound and unwound around the central body or a central drum as it rotates relative to the wheels), the host platform requirements are reduced to a simple mount, through which power and communication may optionally be routed.

Robust mobility in extreme terrains is enabled by the combination of *Axel*'s tether and its wheel design (see Chapter 3). The tether provides climbing and anchoring forces on steep slopes or cliffs when wheel traction is not possible or insufficient. The grouser wheels provide good traction in sandy and loose soil, and they also enable *Axel* to climb over obstacles that are a significant fraction of the wheel diameter.

Axel's minimalist design satisfies many of the severe constraints imposed by space mission design and provides many advantages for exploring extreme terrain. The first advantage is that it adds flexibility in mission deployment scenarios. Because of its low mass, *Axel* could be mounted as an add-on daughter-ship to a larger mission. With only a few actuators—one for each wheel and one or two for the caster arm and body rotation—*Axel* is relatively cheap to manufacture, facilitating the deployment of several redundant copies on a single mission. In addition, since *Axel* requires only a simple mount, *Axel* could be anchored by a larger rover or a lander.

Another advantage of *Axel*'s simple design is a reduced failure rate. Fewer motors lead to fewer moving parts, which in turn increases mechanical robustness. Since *Axel* is intended to operate on very risky terrain, reducing the possible internal failures is vital to mission success. With all the

motors' rotation axes aligned, both the caster arm motor and wheel motors can drive the rover in a straight line, thus providing redundancy in case of an actuator failure.

Furthermore, *Axel's* symmetric body makes it indifferent to tip-over scenarios. Since the robot has no preferred right-side-up state, *Axel* cannot be immobilized by tumbling into an inverted configuration.

Axel's central body also houses and protects all of its hardware and electronic components. This eliminates the need to run wiring outside of the body, reducing heat loss, simplifying thermal design, and helping *Axel* maintain a constant internal temperature, even in the cold environments of the outer solar system. This thermal engineering approach also allows for lower cost avionics and actuator components.

By routing the tether through the caster arm and wrapping it around a central cylinder, *Axel's* own body acts as the reel of a winch. Unreeling in this manner, the tether is laid over the terrain as *Axel* descends, and it is collected as the rover returns to the host. In contrast to a winch mounted on the host, our approach minimizes abrasion on the tether from rocks and cliff faces.

The *Axel* rover embodies a minimalistic, symmetric, and low-cost tethered design philosophy that is well-suited to pioneer extreme terrain exploration in future missions to the outer solar system.

2.3 First-Generation *Axel* Prototype

The first generation *Axel* prototype, or *Axel 1* for short, was adapted from an original *Axel* concept [50] that was designed to be a modular vehicle which carried science payload modules. Figure 2.2a shows the original reconfigurable vehicle concept. Unfortunately, due to budget limitations, only one rover was ever built (Figure 2.2b), and the project was shelved in 2004. In 2006, however, increasing interest in accessing extreme terrains led to a re-evaluation of *Axel's* potential as a rappelling rover. It was hypothesized that its cylindrical design would easily adapt into a winch system, which could be used to raise and lower the robot along steep slopes.

2.3.1 Proof of Concept

After repairing and replacing malfunctioning and broken components, affixing a tether to the system, and rewriting the control software, proof-of-concept tests were conducted in the Mars Yard at JPL [51]. Driving down the vertical front face of the observer balcony and onto sloped sandy terrain, *Axel* demonstrated the feasibility of a simplistic three-motor rappelling robot (Figure 2.3).

Tethered operation was tested on various slopes with different ground types. Approximately 15 runs were conducted on a 3 m stretch of 15°-20° slopes consisting of packed dirt. Another 8 runs were conducted on a 5 m slope varying in inclination from 0°-40° (Figure 2.3). The experiments took place in the JPL Mars Yard, covering terrain consisting of loosely packed sand on a slope

(a) Modular *Axel* concept(b) Original *Axel* hardwareFigure 2.2: Original modular *Axel* concept and hardware in the JPL Mars Yard.(a) *Axel 1* rappelling off the observer balcony(b) *Axel 1* affixed with tether, safety rope, power cable, and sampling device

Figure 2.3: The *Axel 1* proof-of-concept tests conducted at the JPL Mars Yard. *Axel* was powered by an external power supply and required a safety tether in case of malfunction, resulting in two extra cables. Figure 2.3a shows Issa Nesnas (left) operating the video camera, Pablo Abad-Manterola (center) controlling the rover with a laptop, and Jeffrey Edlund (right) managing the safety tether.

Rover	Drive Mode	Ground Type	Inclination	Max Energy Cost ± Std Error ($J/(kg * m)$)
Axel	Rolling	Loose Sand	0°	35.55 ± 1.05
Axel	Tumbling	Loose Sand	0°	19.71 ± 0.46
Axel	Rolling	Packed Dirt	13°	35.84 ± 0.5
Axel	Tumbling	Packed Dirt	13°	28.42 ± 2.03
Rover	Drive Mode	Ground Type	Inclination	Avg Energy Cost ($J/(kg * m)$)
Rocky 8	Rolling	Loose Sand	0°	21.38

Table 2.1: Maximum energy cost for the untethered *Axel* rover to travel one meter compared to the average energy cost for the *Rocky 8* rover

with a number of rocks less than 1 m in size. Excursions ranged from 10 to 25 m round trip and included several maneuvers on the slope to push the limits of *Axel*'s capabilities, including rappelling down a vertical (90°) face, avoiding hazardous rocks, turning in place while tethered, arc driving, sampling, and driving both forwards and backwards. The tests on all slopes proved very successful. *Axel* managed to both ascend and descend the steep terrain comfortably, even over rocks that were approximately 1/3 of the wheel diameter.

During the Mars Yard experiments, *Axel* was also affixed with a rudimentary sampling device, consisting of a tube with an opening at one end, mounted in-line with the caster arm (Figure 2.3b). By pointing the caster arm into the ground on sloped terrain and lowering the rover, the sampling device successfully collected samples of sand on uneven terrain. Multiple experiments demonstrated, however, that the device worked well only for cohesive sand and on slopes greater than 10°.

Without a tether (or when the tether is slack), *Axel* has two types of driving modes: rolling and tumbling. In rolling mode, *Axel*'s wheels are powered and the caster arm is kept fixed, keeping the body pitch angle constant as the rover moves. In tumbling mode, the caster arm is powered while the wheels are kept fixed, causing the body to tumble forward as it moves.

Twelve untethered runs were performed to measure *Axel*'s power consumption and efficiency—three for each type of driving mode on both flat and sloped terrain. For all of the tests, *Axel* was running at 24 volts. Maximum current measurements from the power supply were recorded under each specific operating condition. Thus, the data represents an upper bound for the power usage and worst-case scenario in terms of efficiency. The figures are also normalized by distance and weight in order to provide a basis for comparison to other rovers. Data collected from tests conducted on loose sand and packed dirt with 0° and 13° inclination, respectively, are enumerated in Table 2.1, which also includes data from *Rocky 8*¹ for comparison.

On both flat and slightly inclined terrain, driving the 25 kg *Axel* rover untethered in tumbling mode used significantly less power and proved more efficient than rolling mode. This is attributed to

¹*Rocky 8* is a rocker-bogie suspension rover built after *Sojourner* as a precursor to the MER rovers *Spirit* and *Opportunity*.

the fact that the caster arm uses a smaller actuator with a higher output torque (but slower speed) compared to the wheel actuators. *Axel* was originally designed to quickly manage and maneuver large payloads, which required higher speed and more powerful motors to drive the wheels. The calculated upper bound values for power and efficiency for the *Axel* system are on par with those of *Rocky 8* (Table 2.1).

The first *Axel 1* experiments conducted in the JPL Mars Yard proved the effectiveness of a simplistic, cylindrical, rappelling robot in traversing steep terrains. By using a tether, a significant increase in mobility was achieved with only three actuators, validating the *Axel* concept as an extreme terrain robotic system.

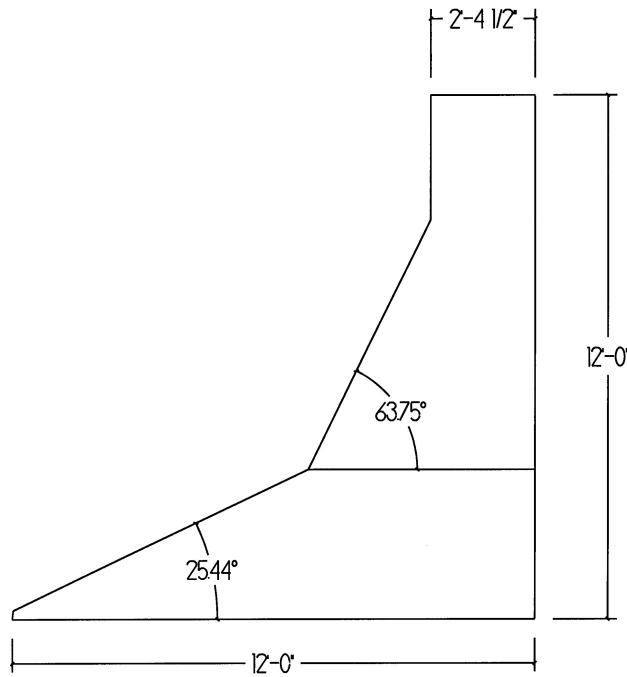
2.3.2 Artificial Lunar Crater Tests

In the summer of 2008, the Smithsonian Institute invited *Axel* to Washington, D.C., for their annual Folklife Festival as part of the “NASA: 50 Years in Space” celebration. In addition, the Smithsonian constructed an artificial lunar crater for *Axel* to use in demonstrating its rappelling abilities to the public. The structure, made of exterior plywood and covered in a textured paint, stood 12 feet high, 12 feet long, 8 feet wide, and consisted of three slopes of varying angles. The Smithsonian mounted artificial rocks on the surface, and they cut a sand pit at the foot of the wall which could be used to practice sampling maneuvers (Figure 2.4).

Several important upgrades were implemented on the *Axel 1* rover in order to prepare for the demonstrations in Washington, DC. First and foremost, the external power supply was replaced by a 4.2 amp-hour lithium polymer battery mounted inside the rover, removing the need for an exterior cable and allowing the rover to operate continuously for one hour before requiring a recharge. Two Point Grey 1024 x 768 color FireWire cameras were mounted to the outside of the central tether section with a 25 cm baseline, streaming video as the rover was operated. Additionally, a MicroStrain 3DM-GX1 inertial measurement unit (IMU) was installed at the center of the body. By correlating the IMU information with the cameras, the images sent from the rover could be properly oriented, even when *Axel* was in an upside-down configuration.

Finally, *Axel*'s sampling device was modified from the original proof-of-concept tests conducted earlier. The new design featured a T-shaped tube mounted on the end of the caster arm (Figure 2.5). After pointing the arm into the ground, *Axel* could rotate in place in either direction to collect a sample. This method worked well even for loose sand and on slopes all the way down to 0°. The new sampling device also had a removable collection tube at the bottom of the “T” where a mother-ship rover could potentially remove the sample for scientific analysis. For more details on the specifics of the system upgrades done in preparation for the trip to Washington, D.C., I refer the reader to [10].

By the end of the trip to Washington, D.C., well over 100 tests had been conducted on the artificial lunar crater. *Axel* performed very well on the structure, demonstrating the ability to rappel



(a) Wall schematic.



(b) Picture of the wall in Washington, DC.

Figure 2.4: Artificial lunar crater constructed of plywood and covered in textured paint and artificial rocks. The sandbox at the base was used to practice sampling maneuvers. Srikanth Saripalli stands next to *Axel 1*, which was undergoing repairs.

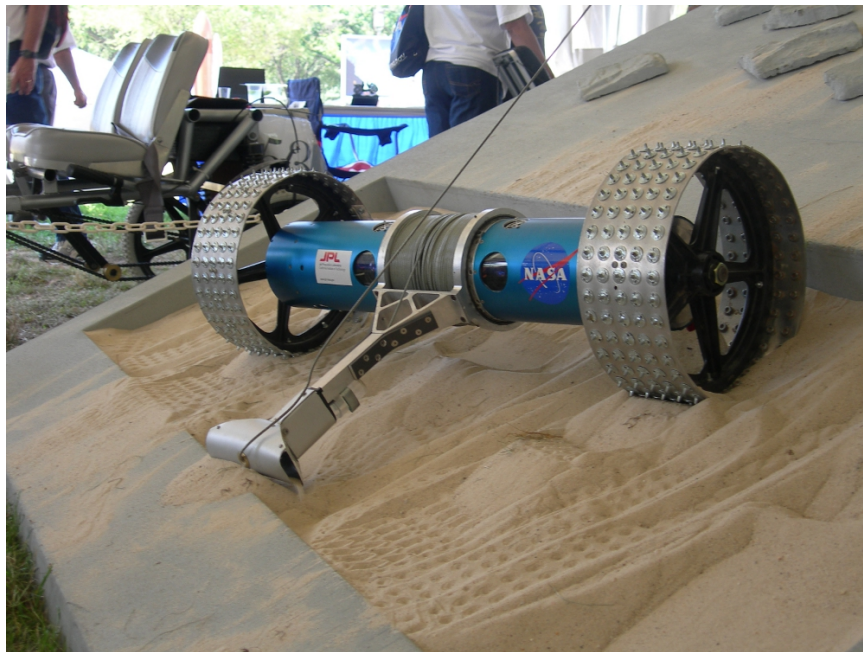


Figure 2.5: Sampling on the artificial lunar crater with the T-shaped sampling device

down slopes ranging from 0 to 90 degrees and collect samples. Video was successfully captured and streamed from the two cameras and correlated with sensor data from the IMU.

2.3.3 Long Traversals

To further push the limits of the rover’s hardware, *Axel* needed to be subjected to longer traversals and rockier terrain, which required an upgrade to several of the rover’s key components. Specifically, *Axel*’s communication system, wheel design, sampling mechanism, and tether were targeted for improvement.

To climb over even greater rock obstacles, experiments were conducted with a variety of different wheel designs, including cleated wheels and bike tires. For a detailed analysis on wheel design and performance, see Chapter 3. Ultimately, a design which more than doubled the diameter of *Axel*’s wheels (from 12” to 26”) was selected, and they were outfitted with large grousers, or “paddles” (Figure 2.6a).

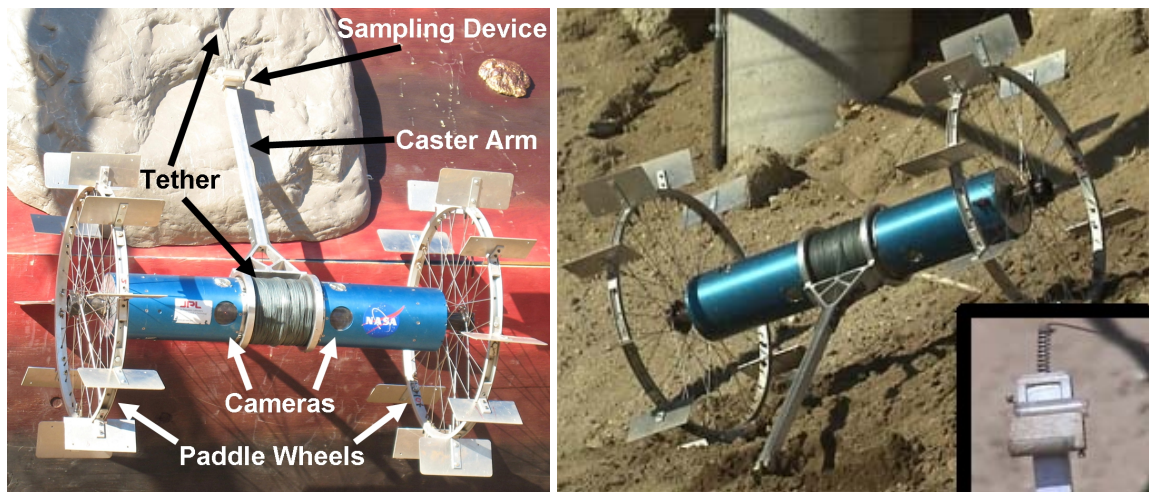
The new sampling mechanism utilized a similar design to the T-shaped device used previously, which kept the openings of the sampling tubes perpendicular to the long axis of the caster arm. In addition, the new device featured two removable sampling tubes (instead of one) for the collection of distinct samples, and it was smaller, lighter, and more compact (Figure 2.6b).

Finally, many different options were investigated for tether material selection. A strong fiber material called high-performance polyethylene (HPPE), with a maximum load capacity of 500 lb, was chosen for the experiments. HPPE has a very high strength-to-weight ratio, making it very useful for climbing applications. Furthermore, it is very resistant to abrasion, minimizing the damage done from rocks and rough surfaces.

After implementing these wheel, sampling, tether, and communications upgrades (see [11] and [9] for more details), experiments were conducted to test *Axel 1*’s long traversal capabilities in the JPL Mars Yard. Simulating exploration of a Martian crater, a mock lander was secured near the top of the observation platform to serve as an anchor and starting point for *Axel*’s trials. The balcony was transformed into an artificial crater promontory with a 90° slope by using plywood and securing fake rocks to its surface. The setup was intended to mimic the terrain in Cape St. Vincent on Mars (Figure 1.4).

Using teleoperation, *Axel* demonstrated its ability to descend down slopes 90° or greater, traverse to flat ground, sample loose soil on slopes ranging from 0° to 40°, travel over rocky terrain, and finally ascend back up the vertical promontory to its original starting position (Figure 2.8).

15 runs were conducted, each round trip taking approximately 20 minutes and extending 30 m from the anchor point. The grouser wheels were very effective at surmounting obstacles in the Mars Yard, easily traversing rocks up to 55% of its wheel diameter with and without the aid of the tether (Figure 2.7) [11, 9].



(a) *Axel 1* on a vertical face with key features labeled (b) *Axel 1* taking a soil sample. Inset: close-up of the sampling device

Figure 2.6: First-generation *Axel* prototype descending a vertical face and taking a sample. *Axel* samples by pointing the caster arm into the ground and turning in place. Sand enters through the openings on the ends of the removable sampling tubes (inset).

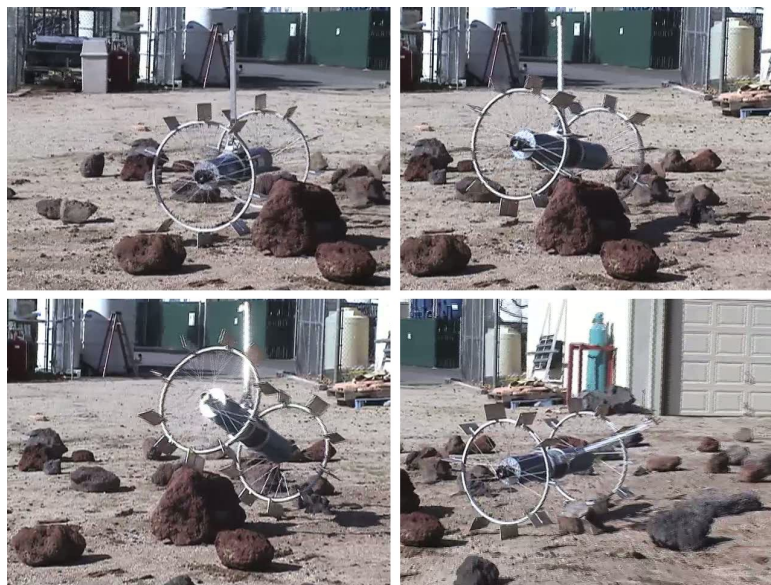


Figure 2.7: From top-left to bottom-right: *Axel 1* uses its larger radius paddle wheels to traverse a rock more than half of its wheel diameter in the JPL Mars Yard.

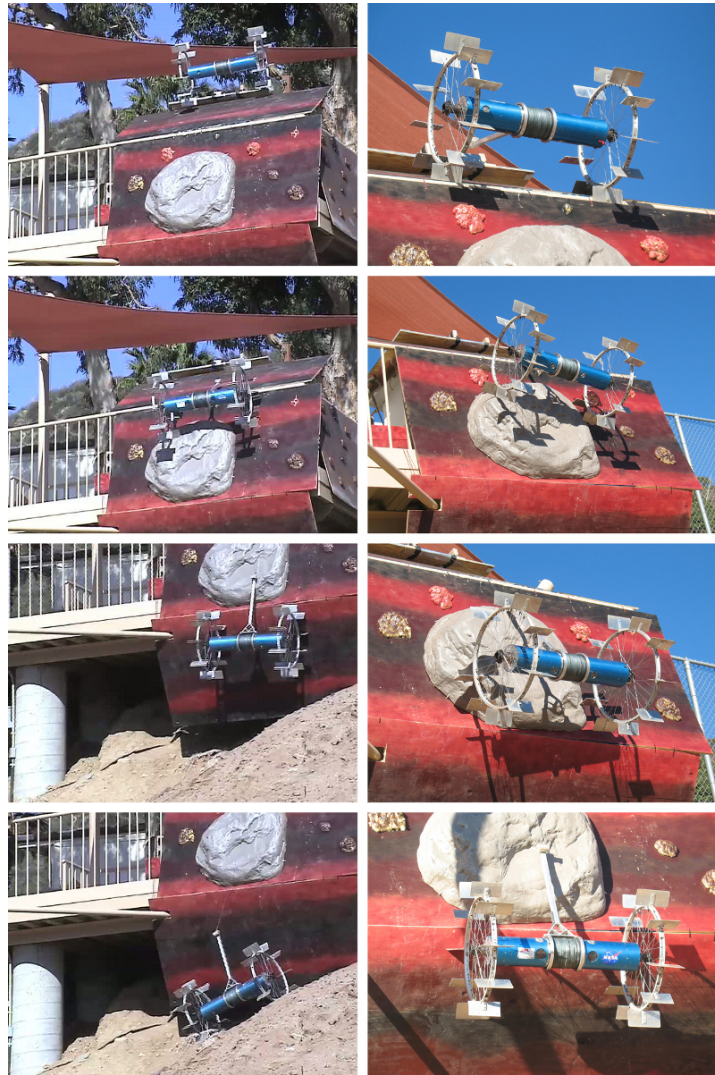


Figure 2.8: Left column from top to bottom: *Axel 1* descending down onto sloped terrain in the JPL Mars Yard. Right column from bottom to top: *Axel 1* ascending over a simulated crater promontory onto a mock lander

Ascending over a ledge, from a 90° slope to a 0° horizontal, poses a practical challenge for *Axel*—the caster motor may stall during this maneuver due to a significant increase in the required torque, and the tether tension can rise dramatically. For more details and a computational analysis of this scenario, see Section 5.2. The large wheel radii, in addition to improving obstacle traversal performance, also had the added benefit of facilitating the return ascent over the promontory. In none of the experiments did the tether rupture from over-stress.

Axel's performance on extreme terrain is primarily a function of its wheel design, tether control, and on-board sensor suite, in conjunction with an algorithm that plans the rover's movements. The following three chapters will analyze and further develop these key rover characteristics in order to improve rugged terrain mobility.

Chapter 3

Wheel Design

This chapter summarizes the developments in wheel design along with theoretical and experimental analysis in order to optimize *Axel* for steep and rugged terrain. Wheel performance is evaluated on the following criteria: obstacle traversal, sinkage, and efficiency.

3.1 Cleated Wheels

The first *Axel* prototype was adapted from an original concept designed to carry payloads on flat terrain with sparsely scattered rocks (Section 2.3). As a result, its wheels were optimized for efficiency on even ground and could only surpass obstacles up to 6" in size. Fabricated out of a thin aluminum rim and covered in small cleats (Figure 2.2), the original 12" diameter wheels allowed *Axel* to drive with energy costs similar to those of the *Rocky 8* rover (see Section 2.3.1).

In order to optimize *Axel*'s capabilities for rugged terrain, it was necessary to improve its rock-traversing ability. To this end, 26" Hakkapeliitta W240 mountain bike tires were mounted on *Axel*'s chassis (Figure 3.1). The tires, specifically designed for snow and ice, had small metal cleats all along the circumference, similar to the original aluminum rim. By purchasing the wheels commercially rather than custom fabricating them for *Axel*, manufacturing time and cost were greatly reduced while prototyping this new design. It was hypothesized that *Axel* would easily surpass much larger obstacles with these new larger diameter tires.

However, experiments conducted at JPL with the new tires did not confirm this initial hypothesis. Driving in the Mini Mars Yard, as the bike wheel approached an obstacle, *Axel* would typically turn in place while the wheel slipped without gripping. Experiments were conducted with the tires fully inflated, half inflated, and with very low inflation. For all three cases, however, the results were very similar and no significant difference was noted. Even over small rocks that the original 12" aluminum wheels could traverse easily, the new tires did not grip effectively. In only a few instances did the wheels gain traction and travel over the obstacle.

The results of the mountain bike tire experiments reaffirmed the importance of the cleats on the



Figure 3.1: *Axel* with 26" diameter mountain bike tires

original wheels. The original cleats gripped effectively on rocks and provided a small lever-arm to climb over obstacles. Although the bike tires did feature metal cleats, they outlined a much lower profile than on the aluminum wheels. Thus, the difference between them proved to be the key factor between the two wheel types, and their effect on obstacle traversing ability can not be overlooked when optimizing an extreme terrain rover.

3.2 Grouser Wheels

In order to test the limits of the cleat's capabilities in rock traversal, a 5-grouser (or "paddle") wheel design was prototyped on a 12" plastic rim (Figure 3.2). The grousers, each approximately 3" long, were evenly spaced along the circumference of the wheel.

Despite the awkward motion while driving along flat ground, these wheels were incredibly effective at surpassing obstacles. Experiments at JPL demonstrated that, for the first time, *Axel* was able to traverse rocks that were 70%-80% of the wheel diameter, including the length of the grousers. The rover also managed to climb a 12" step obstacle without any difficulty. Additionally, the paddles provide the rover with much stability, which allowed *Axel* to successfully ascend a 25°-30° slope over packed dirt without the aid of a tether.

Scaling up the grouser-wheel design proved remarkably easy. The tubes and tires were removed from the purchased bike wheels and ten evenly spaced paddles were affixed along the circumference of each (Figure 2.6). Increasing the number of grousers from the previous wheels reduced the rover's jarring vertical motion while still maintaining sufficient obstacle traversal capability.

The new large radius grouser wheels performed very well in experiments conducted at the JPL Mars Yard. Both independently and with the aid of the tether, *Axel* easily surpassed rocks slightly larger than 1/2 of the wheel diameter.

The success over obstacles comes intuitively at a loss of efficiency while traveling on flat ground.



Figure 3.2: *Axel* with 5-grouser wheel design

Section 3.3.3 outlines experiments conducted to precisely quantify this loss of efficiency. However, the goal of the *Axel* wheel design was to optimize for rugged terrain, not efficiency. The grouser wheels not only maintain the rover's stability on steep slopes, but they also provide excellent obstacle traversal capabilities.

Optimizing wheel radius, grouser length, and grouser spacing is a function of the terrain material and slope, in addition to the obstacle type, size, and quantity. The grouser wheels developed for *Axel* performed well in the Mars Yard, however these key wheel parameters need to be adjusted based upon the rover's particular mission requirements.

3.3 Analysis and Experiments

This section develops models in order to build a better understanding of how *Axel*'s wheels drive over obstacles and how sinkage will affect the rover. We then quantify the energy-cost-to-travel of different wheel types through experimental analysis and examine the trade-offs between smooth wheels and grouser wheels.

3.3.1 Obstacle Traversal

A simplified physics model will now be presented in order to help build a better understanding of how *Axel*'s wheels drive over obstacles. While obstacle traversal is greatly improved by the use of a tether, *Axel* must be able to operate independently while on flat ground. Therefore, in order to focus particularly on wheel optimization, the tether input is excluded from the analysis.

Figure 3.3 represents the forces experienced by a wheel just as it loses contact with the ground after encountering an obstacle. While obstacle shapes in the field can be quite complicated, for simplicity we consider an object with circular cross section. The wheel contacts the obstacle at

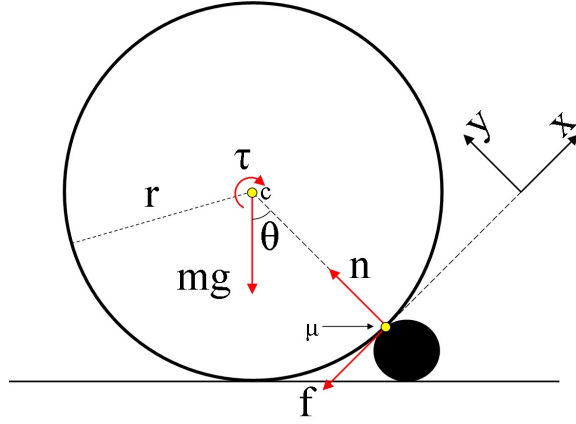


Figure 3.3: Free-body diagram of a wheel traveling over a rock just as it loses contact with the ground

a point along its rim θ radians from the vertical. m is the wheel's mass, r its radius, and I its moment of inertia while rotating in the plane. The coefficient of friction between the wheel and the obstacle is denoted by μ , f is the frictional force, g is the gravity vector, τ represents the torque applied to the wheel by the motor, n is the normal force from the rock on the wheel, a_x and a_y are the accelerations in the x- and y-directions respectively, and α is the wheel's angular acceleration. Summing the forces and moments about the center of the wheel, c :

$$\Sigma F_x = ma_x = -f - mg \sin \theta \quad (3.1)$$

$$\Sigma F_y = ma_y = 0 = n - mg \cos \theta \quad (3.2)$$

$$\Sigma M_c = I\alpha = -fr - \tau. \quad (3.3)$$

Note that $\alpha = -a_x/r$ and $|f| < |\mu n|$ for the wheel to travel without slipping. After rearranging and solving, we find that for the wheel to have a positive acceleration in the x-direction ($a_x > 0$, thereby continuing over the obstacle), two conditions must be met for $0 \leq \theta < \pi/2$:

$$\tau < mgr \sin \theta \quad (3.4)$$

$$\mu > \tan \theta. \quad (3.5)$$

Notice that as θ approaches $\pi/2$, the magnitude of μ must tend toward infinity if the wheel is to climb over the obstacle. Without the aid of a tether, the wheel cannot surpass obstacles whose contact point height is greater than one-half of the wheel diameter above the ground plane. Traditional wheels are therefore fundamentally limited in terms of their performance over obstacles.

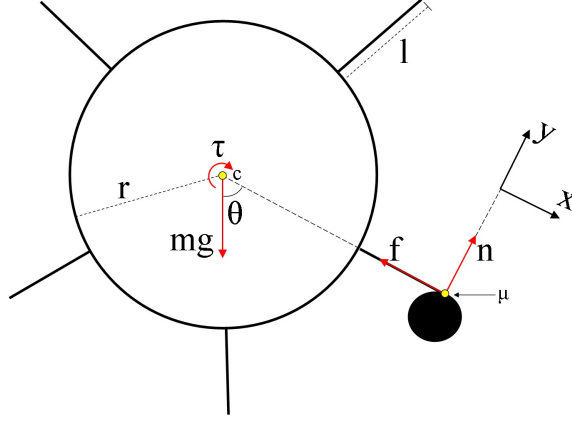


Figure 3.4: Free-body diagram of a grouser wheel as it encounters an obstacle and just as it leaves the ground

With a slight modification, however, the wheel forces can be redirected in the rover's favor. Figure 3.4 presents a free-body diagram of a wheel with five equidistant grousers as it encounters an obstacle and just as it leaves the ground. This wheel provides a motion that is roughly a hybrid of rolling and walking. Letting l denote the length of the grouser, Newton's second law applied to Figure 3.4 yields:

$$\Sigma F_x = ma_x = 0 = -f + mg \cos \theta \quad (3.6)$$

$$\Sigma F_y = ma_y = n - mg \sin \theta \quad (3.7)$$

$$\Sigma M_c = I\alpha = -\tau + n(r + l). \quad (3.8)$$

For the wheel to travel over the obstacle without slipping, note that $\alpha = -a_y / (r + l)$ and once again $|f| < |\mu n|$. To ensure forward movement over the obstacle ($a_y > 0$) when $0 \leq \theta < \pi/2$, two conditions must be met:

$$\tau > mg(r + l) \sin \theta \quad (3.9)$$

$$\mu > \frac{(I + m(r + l)^2) \cos \theta}{I \sin \theta + (r + l) \tau / g}. \quad (3.10)$$

Note that since the lower bound on the coefficient of friction is inversely proportional to input torque, this bound can be reduced by increasing the wheel torque. Furthermore, the lower bound on μ approaches 0 as θ approaches $\pi/2$. Thus, with a grouser wheel design, for a small increase in the required torque, it actually becomes easier to travel over obstacles without slipping, especially as the angle between the grouser blade and the horizontal increases.

If the grouser wheel can slip in the x-direction, then Equation 3.6 becomes:

$$\Sigma F_x = ma_x = -f + mg \cos \theta. \quad (3.11)$$

Here we simplify on the condition that $a_x > 0$ for $0 \leq \theta < \pi/2$ while noting that $|f| = |\mu m|$. As expected, the input torque requirement is the same as in the no-slip case while the bound on the coefficient of friction becomes:

$$\mu < \cot \theta. \quad (3.12)$$

Hence for small angles the grouser wheel travels over obstacles while slipping. As the contact point angle increases, one can expect the grouser wheel to stop slipping and switch to the previous equations of motion. Note that this is in contrast to the traditional wheel, which at the low wheel rotation speeds characteristic of rovers, cannot overcome an obstacle while slipping.

In summary, a simplified physics model of the grouser wheel predicts that it will perform better than a traditional wheel at higher contact point angles. At smaller angles, the grouser wheel will generally overcome the obstacle while it slips along the paddle. This theoretical analysis was validated by experiments conducted at JPL using different wheel types (see Sections 3.1 and 3.2).

3.3.2 Sinkage

A possible drawback to a grouser wheel is that it could potentially sink deeply into soft soils as may be found on the Moon or Mars, greatly affecting the rover's ability to maneuver. Here, we develop a model to estimate the depth of grouser wheel sinkage in loose sand based on Bekker's equations for deformable terrain [21]. We then compare the model to sinkage data taken in the Mini Mars Yard at JPL. The data show that sinkage is not a debilitating issue with this design¹.

Wheel sinkage can be divided into two types: static and dynamic sinkages. The static sinkage is a result of the vertical load of the wheel, and the dynamic sinkage is caused by the wheel's rotation. We assume *Axel* moves *quasi-statically*, meaning that at the slow speeds typical of the rover, we can approximate its motion with static analysis. As a result, we focus our analysis on the static sinkage of the grouser wheel.

Bekker's pressure-sinkage equation relates the depth to which a thin vertical plate penetrates the soil to characteristics of the soil and the pressure on the plate [21, 37]. It is calculated as

$$p(h) = \left(\frac{k_c}{b} + k_\phi \right) h^n, \quad (3.13)$$

where h is the depth of the blade penetration into the ground, b is the width of the plate, and p is

¹This section describes joint work done with Sandeep Chinchali.

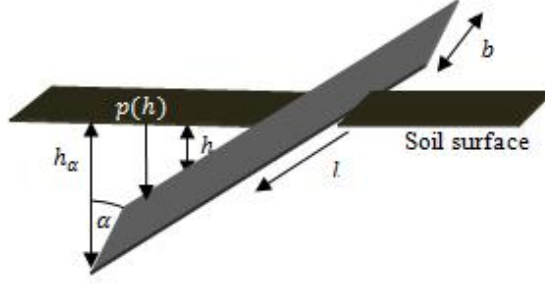


Figure 3.5: Submerged flat plate at arbitrary angle α with key parameters labeled. The plate models a grouser.

the pressure on the plate. k_c and k_ϕ are pressure-sinkage modules, and n is the sinkage exponent, which is based on the soil type [21]. Previous works have conducted experiments to quantify these parameters for a variety of terrains [57, 69, 67]. Shibly [57] found that over a range of terrain parameters reasonable for a planetary rover on deformable soil, the sinkage exponent $n \approx 1$, allowing simplification of Equation 3.13. Dry sand, for example, which was typically used for *Axel*'s mobility experiments, has a sinkage exponent $n = 1.1$.

We incorporate this equation into our sinkage model by considering *Axel*'s grousers as submerged plates at some arbitrary angle, as in Figure 3.5. Integrating the pressure equation along the direction l and approximating the dry sand sinkage exponent $n = 1.1 \approx 1$ in order to realize an analytic expression, we find the total vertical force on one grouser to be approximately

$$F_{grouser} = \frac{bh^2}{2 \cos \alpha} \left(\frac{k_c}{b} + k_\phi \right), \quad (3.14)$$

where α is the angle between plate and the vertical.

Axel 1's wheels feature two slightly different grousers, one larger and one smaller, mounted in an alternating fashion around its rim. While the grouser wheels rotate, *Axel* switches between having one and two grousers in contact with the ground. Thus, the total vertical force between the ground and the wheels is a function of β_{leave} , the angle at which one grouser loses contact with the ground as the wheel drives forward. From the diagram in Figure 3.6, this angle is calculated as

$$\beta_{leave} = \alpha - \theta_{sep} = \cos^{-1} \left(\frac{r + d}{r + l_{p,small}} \right) - \theta_{sep}, \quad (3.15)$$

where r is the radius of the wheel, $l_{p,small}$ is the length of the small plate, and θ_{sep} is defined as the separation angle between the grousers (36.8° in *Axel 1*). The force on each grouser can be calculated as a function of the single variable d , the distance from the bottom of the wheel rim to the ground. In static equilibrium, the force from the grousers will balance with the weight of the rover, and this

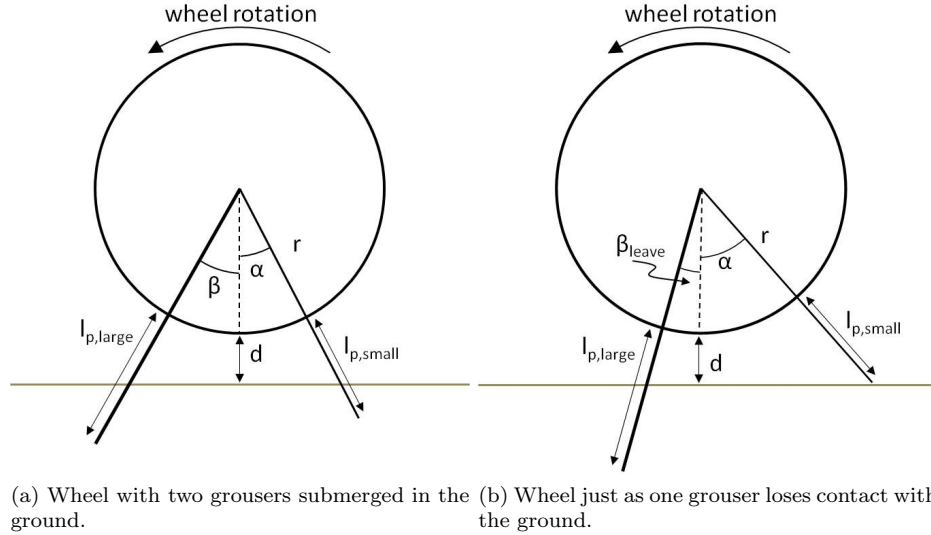


Figure 3.6: Diagrams showing *Axel 1*'s wheel as it rotates. The wheel's grousers alternate between large and small sizes. Note that the diagram is not to scale and shows only two grousers for clarity.

analysis will estimate the depth to which the grousers sink into the soil.

Two sets of measurements of the wheel height, d , were carried out in the JPL Mini Mars Yard for various values of β , the angle between the larger grouser and the vertical. The rover was initially placed on a flat patch of sand with both grousers at approximately equal angles to the vertical. The wheel motor was then driven to rotate the wheel, and measurements of d were taken until the grouser passed the vertical and the rover tipped to the other side. The data is plotted alongside the theoretical model in Figure 3.7, where the wheel height is calculated as a function of the large grouser angle from the vertical, β . The data from the two tests fit the model reasonably well and deviate mostly in the extremes where the large grouser is almost vertical or close to leaving the ground. It may be necessary to develop a different model for these scenarios in order to more closely approximate the observed results.

The model and our experiments suggest the benefit in rock climbing ability gained by the introduction of the grouser does not lead to a wheel design which might sink deeply into soft soils and therefore become bogged down.

3.3.3 Efficiency

The development of an analytical model that can accurately predict the efficiency of a grouser wheel is an ongoing challenge. In this section, we take a more empirical approach, comparing the measured energy expenditure of the grouser wheels and a pair of mountain bike tires (with essentially the same diameter) while both types of wheels travel over flat ground consisting of loose playground sand. One can intuitively hypothesize that the jerky, hybrid rolling/walking motion of the grouser wheel

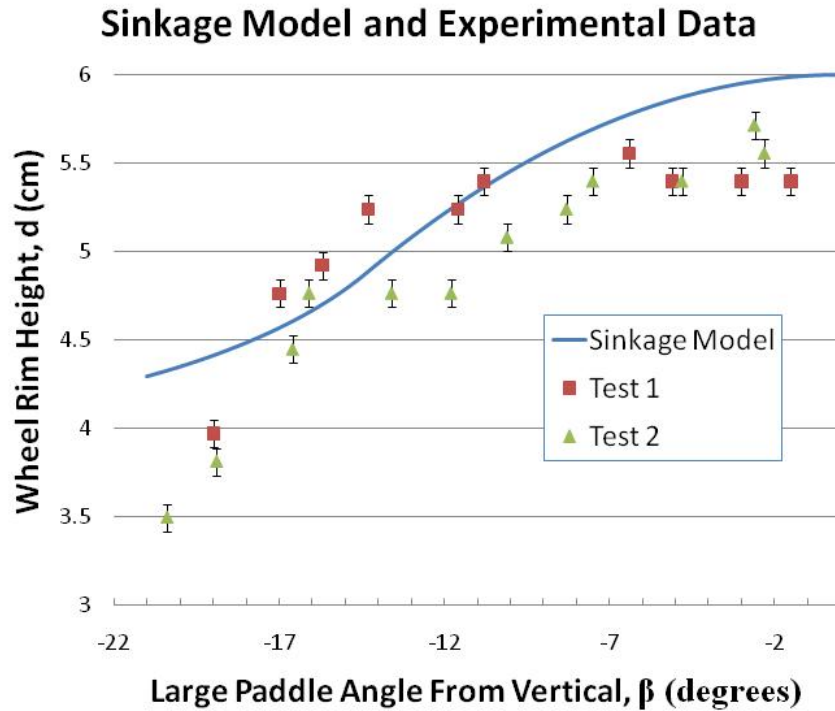


Figure 3.7: Experimental sinkage data overlaid with the theoretical model

would be much less efficient than that of a smooth bike tire over flat ground. Experiments conducted with *Axel* in the Mini Mars Yard at JPL quantify efficiencies and validate this hypothesis.

We delineated a straight, 16 ft long course to drive along at different speeds with each wheel type. Three trials were conducted for each speed with a total of five different speeds, resulting in 15 trials for each wheel type. During each trial, *Axel* was driven by pushing the caster arm into the ground, causing the body and wheels to rotate at the same angular rate. Voltage and current readings for the caster were recorded from the Elmo Whistle motor controller. From these measurements one can approximate the amount of power and energy required to complete the traversal of the test course.

A plot of power vs time is shown in Figure 3.8. Notice the large amplitude and sinusoidal nature of the power curve for the grouser wheels. This corresponds to the increased torque required by the motor to push the wheel to the edge of the grouser and then tumbling forward once the grouser has passed the vertical. The mountain bike tire, on the other hand, is relatively smooth and consistent in terms of its power requirements over flat ground. The difference in linear velocity between the two wheels is a result of the fact that the grouser wheels have a slightly larger effective radius.

For each speed, the power requirements were averaged over the three trials and divided by the velocity in order to calculate the energy required by the rover to travel one meter. The results of this calculation as a function of linear velocity can be seen in Figure 3.9. At any given rover speed, the energy required by the rover is approximately doubled when using the grouser wheels, which

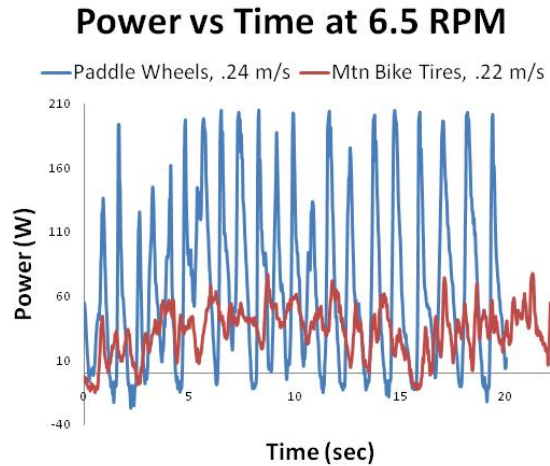


Figure 3.8: Power vs time over a 16 foot straight-line course for both the grouser wheels and mountain bike tires. The caster arm drives the body and wheels at an angular rate of 6.5 rpm.

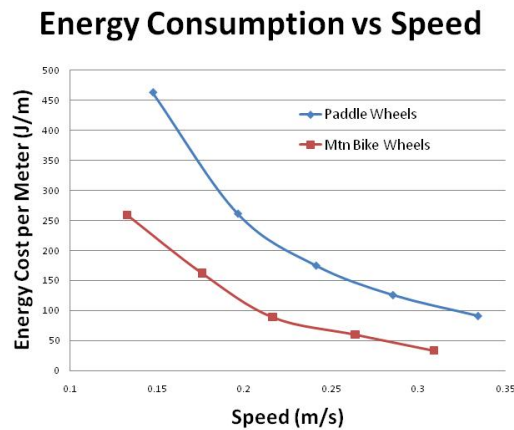


Figure 3.9: Energy consumption per meter traversed plotted as a function of the rover speed supports our initial hypothesis. Furthermore, energy requirements increase dramatically at the lower speeds.

The experiments show that not only are the grouser wheels less efficient while traveling on flat ground, but, as can be seen in Figure 3.8, the non-smooth motion of the rolling grouser wheel can cause the instantaneous power demand to be approximately five times greater than that of the standard wheel. The increased performance over obstacles and steep slopes encourages us to keep the grouser wheel concept, however the significant energy cost-of-travel needs to be addressed if *Axel* is to explore rugged terrains with limited access to energy sources.

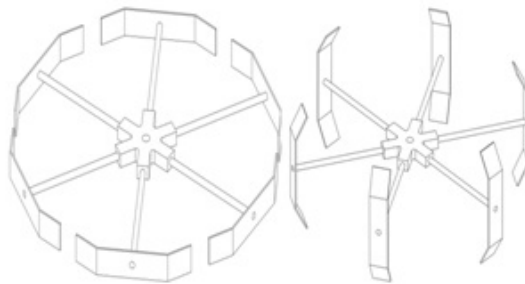


Figure 3.10: Wheel-like and grouser-like configurations of the paddle-rim wheel

3.4 Paddle-Rim Wheels

Because of the limitations in pinpoint landing, in some mission scenarios *Axel* or *DuAxel* (see Chapter 6) is likely to be landed in benign terrain a few kilometers from an extreme terrain site of interest. Hence, it must travel over moderate terrain for some distance, where the analysis in Section 3.3.3 shows that the grouser wheel is less efficient. To address this issue, investigations were performed on a multi-modal wheel design dubbed the *paddle-rim* wheel (Figure 3.10) whose segmented solid rim segments can be rotated between a grouser-like configuration (*paddle mode*) and a rim-like configuration (*rim mode*)².

A prototype of this wheel was tested on the *Axel 1* rover in the simulated Martian terrain of the JPL Mars Yard to assess the trade-off between the efficiency of movement when the wheel is in rim mode vs the ability to overcome obstacles in paddle mode. Efficiency and obstacle maneuvering was also tested with three different rim surface textures: plain aluminum, rubber tread, and crampon-like spikes. Figure 3.12 depicts the efficiencies of the wheel in rim mode (vs vehicle speed) with different textures and parameters. The plot also includes the efficiencies of the original paddle wheels and a standard mountain bike tire. Experiments showed that in rim mode the wheel is significantly more efficient than a grouser wheel, and its efficiency can approach that of a mountain bike tire with the appropriate texture choice.

More importantly, it was discovered that the paddle-rim design, when operated in paddle mode, was even better at overcoming obstacles than the original grouser wheels. The new wheel design routinely surmounted obstacles whose height is 90% of the wheel diameter (Figure 3.11). A multi-modal wheel architecture therefore offers the potential for both efficiency on flat terrain and high mobility in complex terrain.

In this chapter, the development of *Axel 1*'s wheel design was explored through various iterations, working towards optimizing for obstacle traversal capabilities. The result of this work produced a grouser wheel design that surpassed rocks up to 70% of the wheel diameter. Experiments showed that grouser sinkage into soft sand would not significantly hinder mobility on planetary surfaces.

²This section outlines work done by Melissa Tanner and Michelle Jiang.



Figure 3.11: Photo of *Axel 1* as it drives over an obstacle which is 92% of its wheel diameter with paddle-rim wheels operating in paddle mode

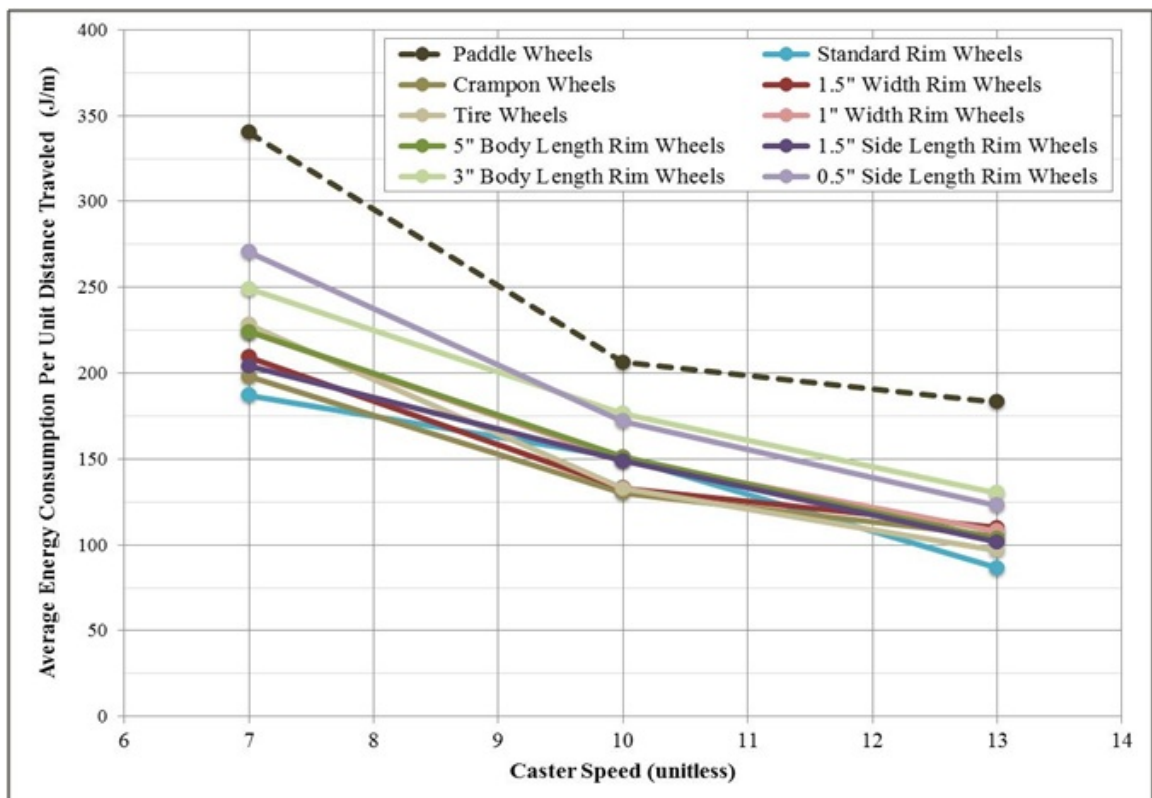


Figure 3.12: Efficiency (as measured by *Axel 1* transportation cost per unit distance traveled over simulated Martian terrain) of the paddle-rim wheel with different textures and rim parameters

Efficiency experiments conducted at JPL, however, demonstrated that the grouser wheel consumed on average twice as much energy per meter traveled as a regular bike tire. The paddle-rim wheel presented an adaptable wheel design, which if actuated, can alternate between modes for efficient long-distance travel and obstacle traversal.

Chapter 4

Tethered Motion Planning

In an ideal mission scenario, a rover operating on a celestial body far from Earth would be controlled by a human driver. With knowledge about the environment and the rover state gathered from sensor data, the operators could send driving instructions over radio signals as they carefully navigate safe paths for the robotic explorer.

Unfortunately, the vast distances between planets in our solar system make direct rover command and control, or *teleoperation*, almost impossible. Although radio signals can reach the moon in approximately two seconds, communication with rovers on other planets varies greatly due to the elliptical orbits of the celestial bodies. For example, a signal sent from a MER rover directly to Earth containing 60 megabits of data (about 1/100 of a CD) would take between 1.5 and 5 hours [8].

This large time delay in communications to other planets forces engineers to bestow their robotic explorers with a large degree of autonomy. Typically, rover operators provide the robots with high-level tasks to perform each day, and the rover will use its on-board intelligence to make the low-level calculations. Example tasks include driving to a particular coordinate, taking measurements, and collecting samples.

In order to navigate on the surface of Mars, robotic rovers need sophisticated motion planning algorithms which incorporate sensor data to first detect obstacles and then plan safe routes around them. The focus of this chapter will be to summarize related works in the field of tethered motion planning, model *Axel's* dynamics, present a blueprint for modeling extreme terrains, discuss obstacle detection on steep slopes, and then illustrate a novel algorithm for operation on extreme terrain. The chapter concludes with both a simple example and a full simulation of the algorithm on terrain data of the Moon's Shackleton crater taken by the Lunar Reconnaissance Orbiter.

4.1 Related Work

Several prior works have considered the problem of motion planning for tethered robots, e.g., [68, 34, 35, 33, 32]. However, in these prior works, the tether acted primarily as an umbilical cord to

provide power, communication, and control signals to the mobile robot. The tether did not generate large reaction forces needed for mobility. The primary motion goal in these efforts was to minimize entanglement of the trailing umbilical tether with obstacles [68, 34] or with other robots [35, 33, 32] in a multi-robot scenario. The motion planning problem considered in this thesis is unique in that not only must tether entanglement be avoided, but the tether and wheels acting together must also be able to generate sufficient forces in order to ascend or descend steep slopes. Moreover, these forces must be properly aligned with the robot’s motion goals to ensure stable robot movement.

Axel is not the first tethered robot to be developed for steep terrain access. The *Dante II* robot [18, 63, 40, 14], designed for descent into an Alaskan volcano, is the most well known tethered robot. The formidable engineering efforts [18, 40] behind the development of this vehicle did not produce a detailed theory for tethered robot motion planning, although this work did analyze the forces experienced by a tethered robot on a slope [63]. It is worth pointing out that *Dante II*’s mission ended when large lateral tether forces destabilized and toppled the vehicle during slope ascent. This demonstrates the need for a motion planning paradigm that integrates motion planning with tether mechanics and terramechanics.

The JPL *Cliffbot* system [55, 46] is another planetary rover prototype designed to rappel across a cliff face under the actuation of two robotic tethers. While *Cliffbot* has traversed cliffs in Svalbard, Norway, no motion planning theory for long descents has emerged from that effort, in part because its dual tether design is not suitable for long descents. The analysis presented in this chapter assumes a single tether, though many of these principles could be extended to a planning algorithm for *Cliffbot*-like robots.

It is important to note that *Axel*’s tether is paid out or reeled in from the robot and not from a winch located at the anchor. This approach minimizes abrasion on the tether as compared to a configuration where tether winching is performed at the anchor. While much of the planning framework developed in this chapter could be applied to anchor-winching systems, the focus is on robot-side winching systems.

4.2 Rover Dynamics

Understanding rover dynamics on extreme terrain is essential to developing motion planning algorithms and incorporating full autonomy. To this end, the equations of motion for the *Axel* rover are derived from basic principles using the Lagrangian construction. These equations are then extended to factor in slip and unilateral tether forces on steep slopes. Although the ultimate goal of this chapter is to analyze the dynamics of the *Axel* rover, the approach can be applied to a wide variety of systems.

4.2.1 Euler-Lagrange Equations

This section applies the well-known Euler-Lagrange equations of motion to the *Axel* system. The formulation is a result stemming from the subject of calculus of variations. A comprehensive treatment of this subject, however, is beyond the scope of this dissertation. For more background on this topic, see [61, 70].

Let q be a set of *generalized coordinates* for the system which uniquely specify the position of all particles in the system. For rovers, q typically consists of the coordinates of a reference frame on the vehicle in addition to the joint angles. The *configuration space*, Q , is the set of all possible system configurations. Let the time derivative of q be denoted \dot{q} , which takes values in TQ , the *tangent bundle* of Q .

Define the Lagrangian function as the difference between the system's kinetic energy, K , and potential energy, V ($L : TQ \rightarrow \mathbb{R}$): $L(q, \dot{q}) = K(q, \dot{q}) - V(q)$. The *Lagrange-d'Alembert principle* states that an unconstrained mechanical system will take the path $c(t)$ ($c : [a, b] \in \mathbb{R} \rightarrow Q$) which extremizes the integral of L with respect to variations in c where the endpoints are fixed ($\delta c(a) = 0$ and $\delta c(b) = 0$).

Proposition 4.1. [43, 53] *A curve, $c(t)$, is said to satisfy the integral Lagrange-d'Alembert principle if*

$$\delta \int_a^b L(c(t), \dot{c}(t)) dt = 0, \quad (4.1)$$

for any given variation δc that vanishes at the endpoints.

Substituting terms and simplifying Equation 4.1 using the calculus of variations, one arrives at the Euler-Lagrange equations of motion.

Theorem 4.1 (Euler-Lagrange). *The Lagrangian function, L , which extremizes the action integral in Equation 4.1, will satisfy the Euler-Lagrange equation*

$$\frac{\partial L}{\partial q} - \frac{d}{dt} \frac{\partial L}{\partial \dot{q}} = 0. \quad (4.2)$$

Proof. The well-known classical proof of this theorem can be found in many textbooks on the subject of the calculus of variations (e.g., [70]). □

It should be noted that the Lagrange-d'Alembert principle can also be applied in the cases where there is an external forcing function, $T(q, \dot{q})$, acting on TQ . In this case, Equation 4.2 becomes:

$$\frac{\partial L}{\partial q} - \frac{d}{dt} \frac{\partial L}{\partial \dot{q}} = T(q, \dot{q}). \quad (4.3)$$

In robotic systems, $T(q, \dot{q})$ is typically a vector consisting of the actuated motor torques.

If there are no constraints imposed on the system, then Equation 4.3 reduces to Newton's second law of motion in generalized coordinates. The next section will extend this formalism to holonomic and non-holonomic constraints and how they apply to a mechanical system.

4.2.2 Holonomic and Non-Holonomic Constraints

Dynamics and control in the presence of constraints is quite a broad topic, and there have been many books written on the subject, e.g., [28, 30, 54], to name a few. The goal of this section is only to showcase the portions of the theory which are relevant to the development of a dynamic model of the *Axel* rover. In particular, [49] provides a concise analysis that relates to the Lagrangian construction presented in Section 4.2.1.

A *constraint* on a mechanical system is a limit on the set of paths that the system can follow. Constraints are applied through *constraint forces*, which act on the system to ensure the constraint equations are not violated.

There are two main types of constraints, namely, *holonomic* and *non-holonomic*. Holonomic constraints limit the possible configurations of the system to a submanifold of the configuration space, Q . If there are k holonomic constraints, they can be written in the form

$$h_i(q) = 0, \quad i = 1, \dots, k. \quad (4.4)$$

Non-holonomic constraints, on the other hand, limit the possible velocities of the system. If there are l non-holonomic constraints, they are assumed to take the Pfaffian form

$$\omega_j(q)\dot{q} = 0, \quad j = 1, \dots, l. \quad (4.5)$$

In other words, the constraint equations are linear in the velocities.

Two assumptions are made about the constraints imposed on the system. The first assumption is that the forces are conservative and do no work. Non-conservative constraints would violate the Lagrange-d'Alembert principle in Section 4.2.1. The second assumption is that the constraints are linearly independent. If the configuration space Q is an open subset of \mathbb{R}^n with coordinates $q = (q_1, \dots, q_n)^T$, linear independence can be verified by checking that the matrices

$$\frac{\partial h}{\partial q} = \begin{bmatrix} \frac{\partial h_1}{\partial q_1} & \cdots & \frac{\partial h_1}{\partial q_n} \\ \vdots & \ddots & \vdots \\ \frac{\partial h_k}{\partial q_1} & \cdots & \frac{\partial h_k}{\partial q_n} \end{bmatrix} \quad (4.6)$$

$$\text{and } \omega(q) = \begin{bmatrix} \omega_1(q) \\ \vdots \\ \omega_l(q) \end{bmatrix} \quad (4.7)$$

are both full row rank. Let the combined holonomic and non-holonomic constraints have the form

$$C(q)\dot{q} = \begin{bmatrix} \frac{\partial h}{\partial q}(q) \\ \omega(q) \end{bmatrix} \dot{q} = 0 \quad C(q) \in \mathbb{R}^{(k+l) \times n}. \quad (4.8)$$

As mentioned previously, the constraints are implemented through constraint forces, which affect the motion of the system. The rows of the matrix $C(q)$ form a non-normalized basis for these constraint forces, and so the dynamics can be written in vector form as

$$\frac{d}{dt} \frac{\partial L}{\partial \dot{q}} - \frac{\partial L}{\partial q} + C^T(q)\Lambda = T(q, \dot{q}), \quad \Lambda = \begin{bmatrix} \lambda_1 \\ \vdots \\ \lambda_{k+l} \end{bmatrix} \quad (4.9)$$

where $\Lambda \in \mathbb{R}^{k+l}$ is a column vector comprised of the magnitudes of the constraint forces, $\lambda_1, \dots, \lambda_{k+l}$, which are called the *Lagrange multipliers*. These Lagrange multipliers need to be computed before the system dynamics can be fully specified.

In the special case where the Lagrangian is the difference between the kinetic and potential energy of the system, Equation 4.9 can be rewritten as

$$M(q)\ddot{q} + B(q, \dot{q}) + G(q) + C^T(q)\Lambda = T(q, \dot{q}), \quad (4.10)$$

where $M(q)$ is a symmetric, positive definite, and invertible mass matrix, $B(q, \dot{q})$ is a column vector comprised of coriolis forces, and $G(q)$ is a column vector of the gravitational forces acting on the system.

This restriction allows for Λ to be explicitly found in the following manner. First, rearrange Equation 4.10 to yield an expression for \ddot{q} :

$$\ddot{q} = M^{-1} (T - B - G - C^T \Lambda). \quad (4.11)$$

Differentiating Equation 4.8 produces:

$$C(q)\ddot{q} + \dot{C}(q)\dot{q} = 0. \quad (4.12)$$

Finally, substitute Equation 4.11 into Equation 4.12 and rearrange to gain the following explicit expression for the Lagrange multipliers:

$$\Lambda = (CM^{-1}C^T)^{-1} (CM^{-1}(T - B - G) + \dot{C}\dot{q}), \quad (4.13)$$

assuming $(CM^{-1}C^T)$ is invertible, which will be true for any practical mass matrix $M(q)$ and with the assumption of linear independence of the constraints.

The full dynamics for the constrained mechanical system are given in Equation 4.11, where the Lagrange multipliers are defined as in Equation 4.13. Given the system's configuration, q , velocities, \dot{q} , and the external forces, $T(q, \dot{q})$, the accelerations, \ddot{q} , can be readily found.

Tethered rovers, such as *Axel*, are special cases of constrained systems whose dynamics are governed by holonomic *inequality* constraints of the form $h_i(q) \geq 0$. For a dynamic system attached to a cable or rope, the inequality constraint maintains that the system cannot traverse beyond the length of unreeled tether. When the rover reaches the end of its tether, an impact occurs, and the dynamics can be modeled by the theory of unilateral contact forces [26].

When active (after an impact has been detected), holonomic inequality constraints impose unilateral contact forces on the dynamic system: $\ddot{z}_i = F(z_i, \dot{z}_i)$, where $z_i = h_i(q)$. More generally, this can be expressed as

$$\frac{\partial h_i}{\partial q} \ddot{q} + \frac{d}{dt} \left[\frac{\partial h_i}{\partial \dot{q}} \right] \dot{q} = F \left(h_i(q), \frac{\partial h_i}{\partial \dot{q}} \dot{q} \right). \quad (4.14)$$

The tether tension force, for example, can be modeled as a mass-spring-damper system. In doing so, however, the tether force will be non-conservative, and it cannot be computed in the dynamics using the method of Lagrange multipliers. The next section will explore how to incorporate non-conservative forces, such as unilateral tether forces and sliding contacts, into the system dynamics using the principles of the power dissipation method.

4.2.3 Non-Conservative Forces and the Power Dissipation Method

Section 4.2.2 discussed how to incorporate conservative constraint forces (e.g., no-slip forces) into the dynamics of a mechanical system. In many simple cases, this will suffice to produce an accurate model. On extreme terrain, however, rovers driving on steep slopes, loose soil, and icy terrain will often slip, and sliding contact forces will predominate. These non-conservative forces must be properly incorporated in order to produce a more accurate dynamic model of rovers traversing extreme terrain. This section summarizes the power dissipation method, uses its basic principle to

compute the forces along sliding contacts, and then adds these forces to the dynamic model.

The Lagrange multipliers of the non-holonomic constraints described in Section 4.2.2 typically quantify the magnitude of the friction force required to maintain a no-slip condition at a particular contact point. This force, however, may exceed the maximum friction force permitted by a given friction model, at which point the system will begin to slip. The system will then switch between different dynamic models based upon which contact points are sliding, i.e., none, some, or all of the contact points. Thus, the dynamics represent a *multiple-model control system* [47]. This idea is expressed formally in Definition 4.1.

Definition 4.1. [48] A control system, Σ , evolving on a smooth n -dimensional manifold, Q , with m inputs, u , is said to be a *multiple-model affine* (MMA) system if it can be expressed in the form

$$\Sigma: \quad \dot{q} = f_0(q, t) + \sum_{i=1}^m f_i(q, t)u_i \quad (4.15)$$

where $q \in Q$. For any q and t , the vector field f_i assumes a value in a finite set of vector fields: $f_i \in \{g_{\alpha_i} | \alpha_i \in I_i\}$, where I_i is an index set.

Given an MMA system Σ , the power dissipated through κ contact states governed by Coulomb friction can be found with the *dissipation functional*:

$$D(q)(\dot{q}) = \sum_{i=1}^{\kappa} \mu_i N_i |\omega_i(q)\dot{q}|, \quad (4.16)$$

where $\omega_i(q)\dot{q}$ is the velocity of the sliding contact, μ_i is the Coulomb coefficient of friction, and N_i represents the normal force at the i th contact. The form of Equation 4.16 reflects the Coulomb friction model, but other friction models can easily be applied by replacing the term $\mu_i n_i$ with a more general state-dependent function $g_i(q)$ [48].

Essentially a restatement of the second law of thermodynamics, the *power dissipation principle* (PDP) states that systems will minimize power or energy dissipation during their state evolution. This principle was first applied in a robotics context in [12], and it provides a useful way of determining the kinematics of a wheeled mobile robot. In particular, Murphey [48] demonstrated that the PDP and the Euler-Lagrange equations provide equivalent formulations for the system dynamics, since the solutions derived from the PDP are kinematic reductions of solutions to the constrained Euler-Lagrange equations.

Consider a planar wheeled robot whose state evolution is described by Equation 4.11. Impose no-slip conditions on the wheels through non-holonomic constraints and the Lagrange multipliers are given by Equation 4.13. If the system has n wheels, then the magnitude of the constraint force on each wheel, F_i , computed as a function of the configuration (q) and the Lagrange multipliers (Λ), must stay within the upper bound given by the governing friction model:

$$|F_i(q, \Lambda)| \leq F_{max}, \quad i = 1, \dots, n. \quad (4.17)$$

For the Coulomb model, for example, $F_{max} = \mu N_i$. If this inequality is broken, then the system must have at least one wheel slipping. With each wheel in either a “slip” or “no-slip” state, there are $(2^n - 1)$ combinations of total slip states (excluding the case where none of the wheels are slipping). Let \mathcal{S}_j be the set of slipping contacts in the j th slip state. To determine which slip state is active, one minimizes the dissipation functional over the set of all possible slip states:

$$\min_j D_j(q)(\dot{q}) = \sum_{i \in \mathcal{S}_j} F_{max} |\omega_i(q) \dot{q}|, \quad j = 1, \dots, 2^n - 1. \quad (4.18)$$

For the slip state, j , which minimizes D , assign $F_{i \in \mathcal{S}_j} = -\text{sign}(v_i) F_{max}$, where v_i is the velocity of the i th slipping contact. Knowing which slip state is active, the Euler-Lagrange equations can be re-computed with the appropriate constraints, and the non-conservative sliding forces can be added into the dynamic model:

$$M(q)\ddot{q} + B(q, \dot{q}) + G(q) + \sum_{i \in \mathcal{S}_j} F_i + \sum_{i \notin \mathcal{S}_j} \lambda_i \omega_i^T(q) = T(q, \dot{q}), \quad i = 1, \dots, n. \quad (4.19)$$

In summary, the dynamics of a wheeled mobile robot with no-slip at all of its contact points can be described by Equation 4.11. If, however, the force on any wheel violates Equation 4.17, the PDP can be used to determine the correct slip state, j , and the state will evolve according to the model given by Equation 4.19. Using this MMA system to describe the dynamics of a rover on extreme terrain provides a more accurate description of the system, especially when sliding forces predominate.

4.2.4 Application to *Axel*

This section presents a model of the *Axel* rover and derives the Lagrangian function and constraint equations which govern its motion. The power dissipation method is applied to derive the various slip states which can occur.

The *Axel* model is given in Figure 4.1. It consists of four rigid bodies joined together: the central body, two wheels, and the caster arm. The subscript “1” refers to properties of the left wheel and “2” refers to those of the right wheel when looking along the positive x-axis in the rover’s coordinate frame. The subscript “b” refers to properties of the body and “c” refers to the caster arm. It is assumed that the wheels each have the same radii ($r_1 = r_2 = r_w$) and mass ($m_1 = m_2 = m_w$). *Axel*’s configuration on a two-dimensional plane can be completely defined by seven variables:

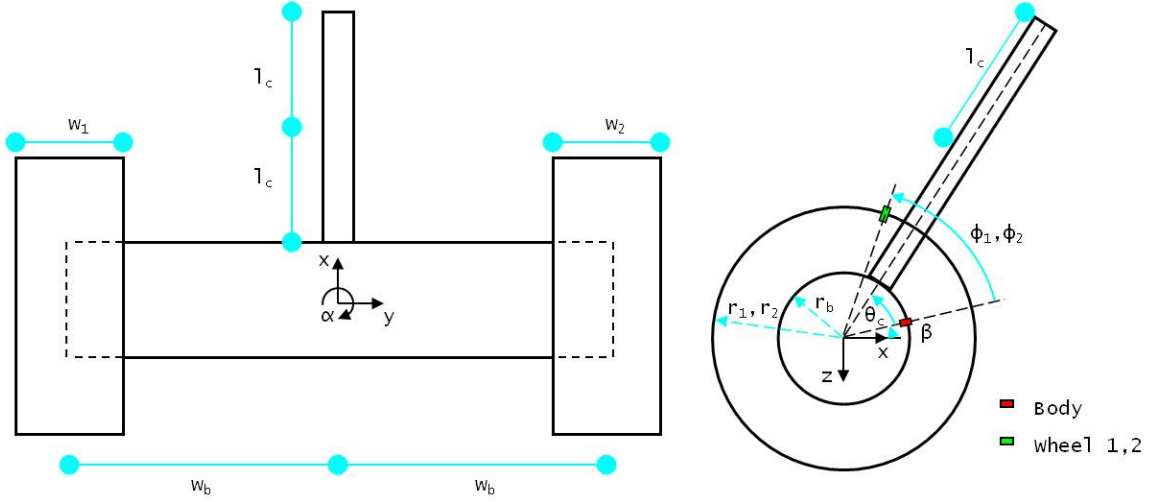


Figure 4.1: Top and side views of the *Axel* model used to derive the equations of motion

$$q = [x \ y \ \alpha \ \beta \ \phi_1 \ \phi_2 \ \theta_c]^T \in \mathbb{R}^2 \times \mathbb{T}^5, \quad (4.20)$$

where x and y are the planar coordinates of the body's center of mass (assumed to be in the center of the body), α is the rover's rotation around the positive z -axis, β is the body's pitch around the y -axis, ϕ_1 and ϕ_2 are the wheel rotation angles, and θ_c is the castor arm angle.

Recall that the Lagrangian function is given by $L(q, \dot{q}) = K(q, \dot{q}) - V(q)$, where $K(q, \dot{q})$ is the kinetic energy and $V(q)$ is the potential energy of the system. The total kinetic energy is given by the sum $K = K_b + K_1 + K_2 + K_c$, where the kinetic energy terms are as follows: K_b is for the body, K_1 and K_2 are for the left and right wheel, and K_c is for the castor arm. The kinetic energy of each rigid body is given by $K_i = \frac{1}{2}m_i \mathbf{v}_i^T \mathbf{v}_i + \frac{1}{2}\boldsymbol{\omega}_i^T I_i \boldsymbol{\omega}_i$, where \mathbf{v}_i is the velocity of the rigid body's center of mass, $\boldsymbol{\omega}_i$ its angular rotation, m_i its mass, and I_i its moment of inertia matrix. With its cylindrical shape and near-homogeneous mass distribution, *Axel's* body is modeled as a uniform cylinder, and hence the inertia matrix becomes diagonal. Calculating the kinetic energy of the central body using $\mathbf{v}_b = [\dot{x}, \dot{y}, 0]^T$, $\boldsymbol{\omega}_b = [0, \dot{\beta}, \dot{\alpha}]^T$ yields

$$K_b(q, \dot{q}) = \frac{1}{2} \left(m_b (\dot{x}^2 + \dot{y}^2) + I_{b_z} \dot{\alpha}^2 + I_{b_y} \dot{\beta}^2 \right). \quad (4.21)$$

The velocity of the left wheel, v_1 , is computed using the equations of rigid body kinematics:

$$\mathbf{v}_1 = \mathbf{v}_b + \boldsymbol{\omega}_1 \times \mathbf{r}_1 = \mathbf{v}_b + (R_b \boldsymbol{\omega}_1^b) \times (R_b \mathbf{r}_1^b) \quad (4.22)$$

where the superscript "b" refers to vectors in the body-fixed coordinate system, \mathbf{r}_1 is the vector pointing to the center of the left wheel, and R_b is the rotation matrix transforming vectors in the body-fixed coordinates to global coordinates. With $\mathbf{r}_1^b = [0, -w_b, 0]^T$, $\boldsymbol{\omega}_1^b = [0, (\dot{\beta} + \dot{\phi}_1), \dot{\alpha}]^T$, using

the inertia matrix of a uniform thin cylinder, and letting R_b be the rotation about the positive z-axis by the angle α yields

$$K_1(q, \dot{q}) = \frac{1}{2} \left[I_{1_z} \dot{\alpha}^2 + I_{1_y} (\dot{\beta} + \dot{\phi}_1)^2 + m_w ((\dot{x} + w_b \dot{\alpha} \cos \alpha)^2 + (\dot{y} + w_b \dot{\alpha} \sin \alpha)^2) \right]. \quad (4.23)$$

Taking advantage of the model's symmetry, K_2 can be easily computed by changing the subscripts "1" to "2" in Equation 4.23 and adjusting for $\mathbf{r}_2^b = -\mathbf{r}_1^b$:

$$K_2(q, \dot{q}) = \frac{1}{2} \left[I_{2_z} \dot{\alpha}^2 + I_{2_y} (\dot{\beta} + \dot{\phi}_2)^2 + m_w ((\dot{x} - w_b \dot{\alpha} \cos \alpha)^2 + (\dot{y} - w_b \dot{\alpha} \sin \alpha)^2) \right]. \quad (4.24)$$

Finally, the caster arm is modeled as a uniform thin rod, yielding no inertia about the arm's body-fixed x-axis. In practice, *Axel's* caster arm is interchangeable between models of different lengths and mass. Through different design iterations, however, the arm is kept as thin as possible in order to reduce volume and mass. Additionally, experiments demonstrated that thin caster arms with small profiles perform much better while ascending vertical walls than bulkier versions which become trapped underneath obstacles. Using the thin rod assumption and applying the caster arm rotation matrix, R_c , to account for both rotations α about the z-axis and θ_c about the y-axis yields the formula for the caster arm's kinetic energy:

$$\begin{aligned} K_c(q, \dot{q}) = & \frac{1}{2} (I_{c_z} \dot{\alpha}^2 + I_{c_y} (\dot{\beta} + \dot{\theta}_c)^2) + \frac{1}{4} m_c (2\dot{x}^2 + 2\dot{y}^2 + (l_c + r_b)^2 (\dot{\alpha}^2 + 2(\dot{\beta} + \dot{\theta}_c)^2)) + \\ & \frac{1}{4} m_c (l_c + r_b) \left[\dot{\alpha} ((l_c + r_b) \dot{\alpha} \cos(2(\beta + \theta_c)) + 4 \cos(\beta + \theta_c) (\dot{y} \cos \alpha - \dot{x} \sin \alpha)) - \right. \\ & \left. 4(\dot{\beta} + \dot{\theta}_c) (\dot{x} \cos \alpha + \dot{y} \sin \alpha) \sin(\beta + \theta_c) \right]. \end{aligned} \quad (4.25)$$

Computing the potential energy of the system is much simpler. Assuming *Axel* is traveling on a plane inclined at angle θ_s relative to the horizontal, the gravity vectors $g \sin \theta_s$ and $g \cos \theta_s$ are applied in the -x and +z directions, respectively. $V(q)$ is merely the sum of potential energies of the system, given by

$$\begin{aligned} V(q) = & (m_b + 2m_w + m_c) x g \sin \theta_s + (m_b + 2m_w) r_w g \cos \theta_s + \\ & m_c (r_b + l_c) \cos \alpha \cos(\beta + \theta_c) g \sin \theta_s + \\ & m_c (r_w + (r_b + l_c) \sin(\beta + \theta_c)) g \cos \theta_s. \end{aligned} \quad (4.26)$$

Given the Lagrangian, it is now a straightforward (albeit time-consuming) calculation to arrive at the Euler-Lagrange equations of motion.

There are three motors in *Axel 1*, one for each wheel and another for the caster arm. The torques are given by $T(q, \dot{q}) = [0, 0, 0, 0, \tau_1, \tau_2, \tau_c]^T$, where τ_1 and τ_2 are the torques on the left and right wheel, and τ_c is the torque applied to the caster arm. The vector $T(q, \dot{q})$ is added to the right-hand side of Equation 4.2.

For the holonomic constraint restricting the tip of the caster arm to lie above the ground plane,

$$-r_w - (r_b + 2l_c) \sin(\beta + \theta_c) \geq 0. \quad (4.27)$$

The full x-y-z coordinates of the tip of the caster arm are given by

$$\boldsymbol{\rho}_c = \begin{bmatrix} x + (r_b + 2l_c) \cos(\beta + \theta_c) \cos \alpha \\ y + (r_b + 2l_c) \cos(\beta + \theta_c) \sin \alpha \\ -r_w - (r_b + 2l_c) \sin(\beta + \theta_c) \end{bmatrix}. \quad (4.28)$$

Assuming an *anchor point* (i.e., the point at which the free end of the tether is tied) is chosen with coordinates $\boldsymbol{\rho}_a = [x_a, y_a, z_a]^T$, a second holonomic inequality constraint arises due to length of the tether:

$$l_t - \|\boldsymbol{\rho}_c - \boldsymbol{\rho}_a\| \geq 0. \quad (4.29)$$

The variable l_t is the length of unreeled tether. Since *Axel's* body is the winch, l_t is a function of the body pitch angle, β : $l_t = l_{t_0} - \beta r_b$, where l_{t_0} is the amount of unreeled tether at time $t = 0$.

To compute the non-holonomic no-slip constraints, first note that the coordinates of a point on the rim of the left and right wheels are given by:

$$\boldsymbol{\rho}_{1,2} = \begin{bmatrix} x \\ y \\ -r_w \end{bmatrix} + R_b \begin{bmatrix} r_w \cos(\beta + \phi_{1,2}) \\ \mp w_b \\ -(r_b + 2l_c) \sin(\beta + \theta_c) \end{bmatrix}. \quad (4.30)$$

The no-slip condition dictates that the velocity of the point on the rim of the wheel touching the ground must be zero:

$$0 = \left. \frac{\partial \boldsymbol{\rho}_{1,2}}{\partial t} \right|_{(\beta + \phi_{1,2}) = -\frac{\pi}{2}}. \quad (4.31)$$

Equation 4.31 results in four non-holonomic constraint equations, but only three are linearly independent:

$$\begin{bmatrix} 1 & 0 & w_b \cos \alpha & r_w \cos \alpha & r_w \cos \alpha & 0 & 0 \\ 1 & 0 & -w_b \cos \alpha & r_w \cos \alpha & 0 & r_w \cos \alpha & 0 \\ 0 & 1 & w_b \sin \alpha & r_w \sin \alpha & r_w \sin \alpha & 0 & 0 \end{bmatrix} \dot{q} = \begin{bmatrix} \omega_1(q) \\ \omega_2(q) \\ \omega_3(q) \end{bmatrix} \dot{q} = \begin{bmatrix} 0 \\ 0 \\ 0 \end{bmatrix}. \quad (4.32)$$

The one-forms $\omega_i(q)$, $i = 1, 2, 3$ in Equation 4.32 serve as a basis for the Lagrange multipliers when added to the Euler-Lagrange equations as in Equation 4.9. The Lagrange multipliers λ_1 , λ_2 , and λ_3 thus represent the friction forces applied at the wheels. Specifically, the forces are:

$$F_{1x} = \lambda_1 \cos \alpha + \lambda_3 \sin \alpha \quad (4.33)$$

$$F_{2x} = \lambda_2 \cos \alpha \quad (4.34)$$

$$F_y = \lambda_3 \cos \alpha - (\lambda_1 + \lambda_2) \sin \alpha, \quad (4.35)$$

where F_{1x} and F_{2x} are the forces in the body-fixed x-direction on wheels 1 and 2, respectively, and F_y is the force in the body-fixed y-direction. Notice that the Lagrange multipliers do not provide enough information to determine how F_y is distributed between the left and right wheel. Let $X \in [0, 1]$ be the fraction of the force F_y applied at the left wheel. Then $F_1^2 = F_{1x}^2 + X^2 F_y^2$ and $F_2^2 = F_{2x}^2 + (1 - X)^2 F_y^2$. Under a Coulomb friction paradigm, $F_1^2 \leq \mu^2 n^2$ and $F_2^2 \leq \mu^2 n^2$ where μ is the coefficient of friction and n is the normal force on the wheel, assumed to be the same for each wheel. Substituting and rearranging provides three inequalities which must be met for the forces on *Axel's* wheels to be within the limit imposed by Coulomb friction (no-slip conditions):

1. $|F_{1x}| \leq \mu n$,
2. $|F_{2x}| \leq \mu n$, and
3. $1 - \left[\frac{\mu^2 n^2 - F_{2x}^2}{F_y^2} \right]^{\frac{1}{2}} \leq \left[\frac{\mu^2 n^2 - F_{1x}^2}{F_y^2} \right]^{\frac{1}{2}}$.

If one of these inequalities is violated, *Axel* will slip in one of 3 possible slip states: left wheel slips, right wheel slips, or both wheels slip. The power dissipated in each case is given by

$$D_1 = \mu n |\omega_1(q) \dot{q}|, \quad (4.36)$$

$$D_2 = \mu n |\omega_2(q) \dot{q}|, \quad (4.37)$$

$$D_3 = F_{1x} |\omega_1(q) \dot{q}| + F_{2x} |\omega_2(q) \dot{q}| + F_y |\omega_3(q) \dot{q}|. \quad (4.38)$$

The forces in the case where both wheels slip can be solved as a constrained optimization problem where F_{1x} , F_{2x} , and F_y are calculated knowing that the magnitude of the force on each wheel is

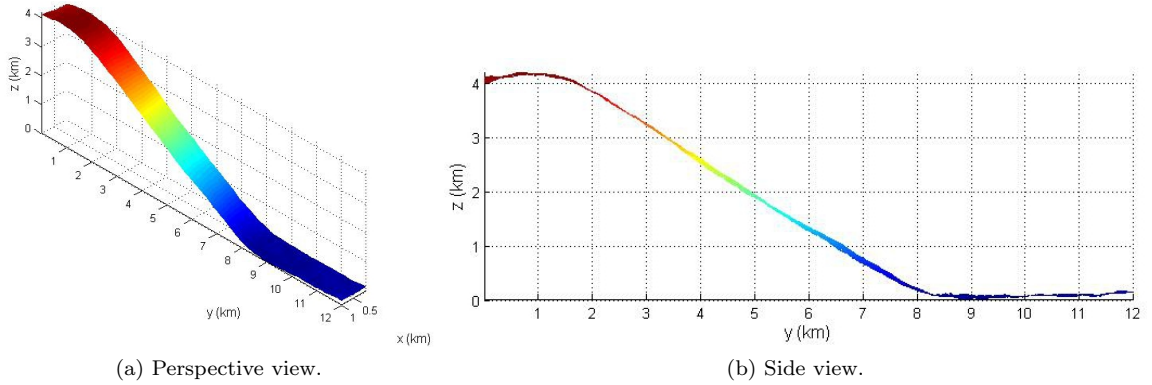


Figure 4.2: Perspective and side views of an elevation map of a 1-km-wide strip of the Shackleton crater taken by the LOLA/LRO. Color gradient varies with height along the slope of the crater.

μn . The slip state is determined by computing the state, D_i , which minimizes the power dissipated. The skidding forces are then computed and added to the Euler-Lagrange equations.

The analysis in this section constructed a multiple-model system which defines *Axel's* equations of motion while tethered on a slope of angle θ_s . The model switches between states of slip and no-slip based upon the Coulomb friction law and the power dissipation principle. The following sections will build models for extreme terrain, develop an algorithm for obstacle detection, and then plan paths which do not entangle the tether around the obstacles.

4.3 Modeling Extreme Terrain

Extreme terrains can vary greatly in their size, slopes, obstacles, and soil characteristics. This section develops a generic blueprint for the extreme planetary terrains that one would expect to encounter. By doing so, the motion planning algorithm presented in Section 4.5 becomes more versatile and can be applied to a wide variety of science targets for tethered robot systems. We use data obtained from a lunar orbiter to motivate the analysis.

Since reaching lunar orbit in June of 2009, NASA's Lunar Reconnaissance Orbiter (LRO) has been acquiring altimetry data to produce a 3-dimensional map of the Moon's surface [6]. Figure 4.2 shows a portion of this data from the north wall of the Shackleton crater taken by the LRO's Lunar Orbiter Laser Altimeter (LOLA) [7]. The Shackleton crater is a good example of an extreme planetary terrain that conventional, untethered rovers would be unable to explore, and it is a candidate application for *Axel*. The elevation map has 1 m^2 resolution in the x-y plane and 10^{-5} m resolution along the z-axis.

The data show that the crater walls have a very consistent and steep slope over 7 km long. While descending or ascending the slope, a robot must rely upon the tether for climbing or support forces, as beyond a certain slope angle (which depends upon wheel size and geometry, the wheel-

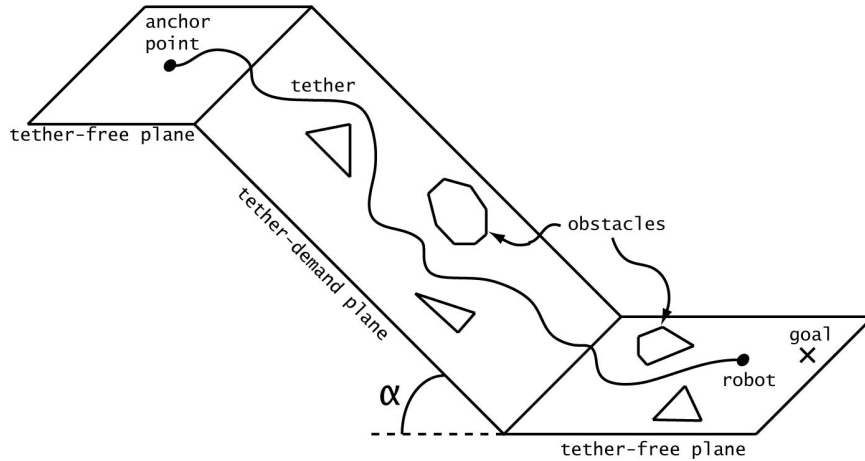


Figure 4.3: Simplified 3-plane model of the Shackleton crater

soil interaction forces, the robot mass, and the wheels' configuration), the wheels cannot reliably generate sufficient traction forces to propel the robot. Additionally, the crater floor and rim, at least on a macroscopic scale, are relatively flat. Thus, we can conceptualize the rim, crater floor, and slope as an intersection of three planes, two of which are roughly horizontal and the other sloped at a steep angle α (Figure 4.3).

More generally, many extreme terrains of interest can be divided into an alternating sequence of gentle slopes (termed *tether-free* regions where the rover can travel without the aid of its tether) and steep slopes (termed *tether-demand* regions because tether forces are essential for mobility in these regions). For example, the promontory in the Victoria Crater shown in Figure 1.4 can be divided into a reasonably small number of tether-free and tether-demand regions. One can easily conceive of a model consisting of hundreds or thousands of intersecting planes in order to approximate a terrain. And in fact, most available altimetry data for extreme terrains comes in the form of a triangulated mesh. Modeling the crater this way, the general motion planning problem on a complicated 3-dimensional surface is converted into a quasi-2-dimensional problem.

4.4 Obstacle Detection

Indoor autonomous robots can take advantage of their highly structured environments to easily sense and characterize their surroundings. Walls are vertical planes, doorways are rectangular, and an obstacle is anything that rises above the ground, which is completely flat [16, 20, 25, 58, 66, 71]. Rovers operating outdoors in non-urban environments, however, face a difficult challenge. The terrain is typically rough and uneven, and a computer might have difficulty determining if a large object in front of it is a solid rock or compressible vegetation.

The problem of obstacle detection while rappelling on sloped terrain is even more challenging

since we cannot rely solely on accelerometers to calculate the relative ground plane. And an object, which may be an obstacle to a traditional rover, may pose no difficulty for a robot equipped with a tether. In this section, we will summarize a successful algorithm for flat-ground obstacle detection developed by Manduchi et al. [42] and then extend it for operation on sloped terrain. The effectiveness of the new algorithm is then verified by testing it on the Shackleton crater data shown in Figure 4.2.

Definition 4.2. [42] Two surface points \mathbf{p}_1 and \mathbf{p}_2 are called *compatible* with each other if they satisfy the following two conditions:

1. $H_{min} < |p_{2,z} - p_{1,z}| < H_{max}$ (i.e., their difference in height is larger than H_{min} but smaller than H_{max});
2. $\frac{|p_{2,z} - p_{1,z}|}{\|\mathbf{p}_2 - \mathbf{p}_1\|} > \sin \theta_{max}$ (i.e., the line joining them forms an angle with the horizontal plane larger than θ_{max});

where H_{min} , H_{max} , and θ_{max} are constant parameters.

Definition 4.3. [42] Two points \mathbf{p}_1 and \mathbf{p}_2 belong to the same obstacle if:

1. They are compatible with each other, or
2. There exists a chain of compatible point pairs linking \mathbf{p}_1 and \mathbf{p}_2 .

Given a point cloud in a Euclidean space (produced by means of a LIDAR¹, for example), Definitions 4.2 and 4.3 from [42] outline the characteristics required for a group of points to be considered an obstacle on rugged terrain. It can be more intuitively described by the diagram in Figure 4.4. For every point \mathbf{p} in the point cloud, one draws two cones with a vertical axis, vertex \mathbf{p} , and with the cone angle defined by θ_{max} . The points compatible with \mathbf{p} are those that lie within the truncated cones limited by the planes $|y| = H_{min}$ and $|y| = H_{max}$.

The parameters H_{min} , H_{max} , and θ_{max} can be adjusted according to the rover's dimensions and capabilities. H_{min} is the maximum obstacle size that the rover can successfully traverse, θ_{max} is the maximum slope the rover can climb, and H_{max} is a parameter which allows one to limit the search space for compatible points. A large H_{max} may find more compatible points, but it will also increase the algorithm's run-time. H_{max} should be tuned based upon the characteristics of the point cloud data set and the computational power of the CPU.

Manduchi et al. [42] demonstrated this method's ability to detect obstacles using stereo-range data while driving rovers outdoors in off-road environments. This approach is now extended to detect obstacles on elevation maps of extreme terrains.

¹Short for Light Detection And Ranging, *LIDAR* uses pulses of light (often from a laser) to remotely measure distance to a target. It is also sometimes referred to as *LADAR*, which is short for Laser Detection And Ranging.

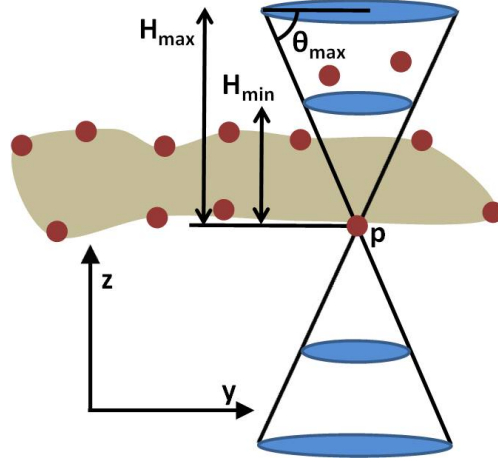


Figure 4.4: For the obstacle detection algorithm in [42], the points compatible with \mathbf{p} are those that lie within the two truncated cones with vertex \mathbf{p} whose shape depends upon the parameters H_{min} , H_{max} , and θ_{max} .

Given a set of intersecting tether-free and tether-demand planes as described in Section 4.3, the goal is to detect obstacles which restrict the motion of a rover maneuvering on the terrain. It is also necessary to distinguish between two classes of obstacles: “positive” obstacles, which extend above the ground plane, and “negative” obstacles, which are holes dropping below the ground plane. Differentiating between obstacle types is essential for tethered systems since positive obstacles will ensnare the tether while negative obstacles will not.

Let α_i , $i = 1, \dots, N$ be the slope angles of the tether-demand and tether-free planes for a model consisting of N intersecting planes. For simplicity, it is assumed that there is no cross slope in the x-direction. In practice, there may be a slight slope perpendicular to the direction of descent, but it is usually small and can be ignored. For hemispherical terrains like craters and volcanoes, the tethered rover should be restricted to a narrow descent corridor so as not to deviate too far laterally from the tether support line, resulting in only small cross slopes. The data from the Shackleton crater (Figure 4.2), for example, does not show a significant slope in the x-direction for a 1 km wide descent corridor. The model can easily be adjusted in the cases where this assumption does not hold.

Adjusting Figure 4.4 so that the vertical axis of the truncated cones is at angle α_i to the vertical, compatibility is redefined for points on sloped terrain.

Definition 4.4 (Sloped Terrain Compatibility). Let \mathbf{p}_1 and \mathbf{p}_2 be two x-y-z points on a terrain with slope angle α . Let d be the distance between point \mathbf{p}_2 and the plane that goes through \mathbf{p}_1 at angle α to the horizontal. d is given by $d = |(p_{1,z} - p_{2,z}) \cos \alpha - (p_{1,y} - p_{2,y}) \sin \alpha|$. \mathbf{p}_2 is *compatible* with \mathbf{p}_1 if it satisfies the following two conditions:

1. $H_{min} < d < H_{max}$ (i.e., their difference in height relative to the sloped plane through \mathbf{p}_1 is

larger than H_{min} but smaller than H_{max} ;

2. $\frac{d}{\|\mathbf{p}_2 - \mathbf{p}_1\|} > \sin \theta_{max}$ (i.e., the line joining the two points forms an angle with the sloped plane larger than θ_{max});

where H_{min} , H_{max} , and θ_{max} are constant parameters.

As an example, the steep terrain obstacle detection algorithm was used on the Shackleton crater data obtained from the LRO (see Section 4.3). The local slope was computed at each row (y-value at 1 m resolution) and used as the slope angle α_i , $i = 1, \dots, 12000$. Figures 4.5 and 4.6 show two different sections of the terrain along with the output from the algorithm. The parameters used for the algorithm, $H_{min} = .1$ m, $H_{max} = 3$ m, and $\theta_{max} = 40^\circ$, represent appropriate values for the scale and capabilities of the *Axel* rover.

As the output shows, this steep terrain obstacle detection algorithm does a very good job of distinguishing between traversable terrain and obstacles, and it is not affected by the angle of the ground plane. Furthermore, obstacles were classified as either positive or negative by comparing the average height of the points immediately surrounding the obstacles to those in the interior (Figures 4.5d and 4.6d).

Combined with the terrain blueprint discussed in Section 4.3, the steep slope obstacle detection algorithm allows one to effectively model extreme terrains using altimetry data from orbiting satellites. When this is coupled with on-the-ground measurements and color images, one can further classify terrain types and predict mobility in various regions of the science target. Given a terrain model and a set of obstacles, the next section discusses how to create an algorithm to plan a path for the rover as it descends into the crater.

4.5 Algorithm

This section considers the conceptual problem of planning the motions of a tethered, wheeled robot on an extreme terrain with both positive and negative obstacles of the type discussed in Sections 4.3 and 4.4.

4.5.1 Summary of the Problem

I assume that a model of the terrain is a priori known. Any future mission to an extreme planetary terrain will likely incorporate an orbiter which can provide altimetry and high-resolution images from which terrain models can be constructed with features on the order of a few meters in scale. Further assume that the terrain is divided into tether-demand and tether-free regions (see Section 4.3). Tether-free and tether-demand planes may contain one or more polygonal obstacles. Assume that an *anchor point*, \mathbf{a}_0 , has been chosen. I.e., the anchor would typically be a mount on a host

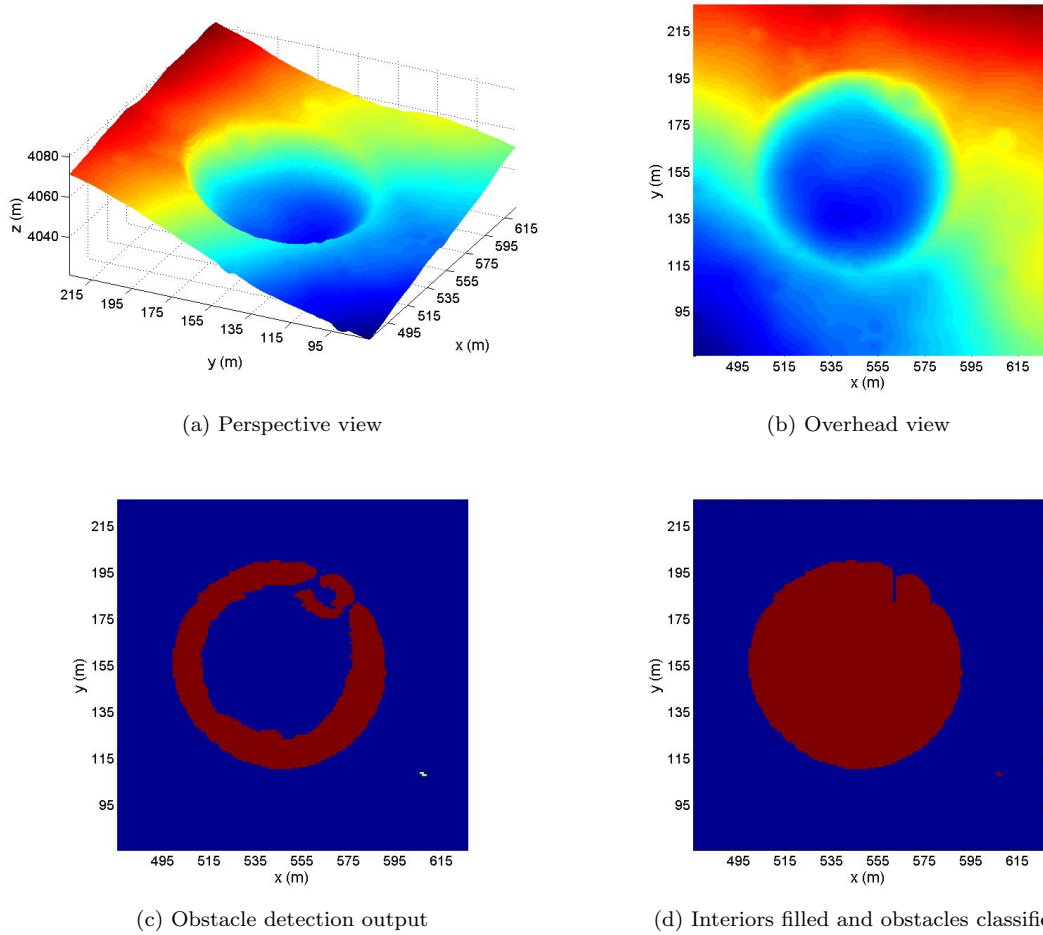


Figure 4.5: 4.5a and 4.5b show a section of relatively low-grade terrain ($\alpha \approx 10^\circ$) from the Shackleton crater data. The modified obstacle detection algorithm was run with parameters $H_{min} = .1$ m, $H_{max} = 3$ m, and $\theta_{max} = 40^\circ$. 4.5c shows two groups of compatible points, represented by the red and green colors. Obstacle-free points are shown in dark blue. 4.5d shows the obstacles with their interiors filled, and both obstacles are classified as “negative”, represented by the red color.

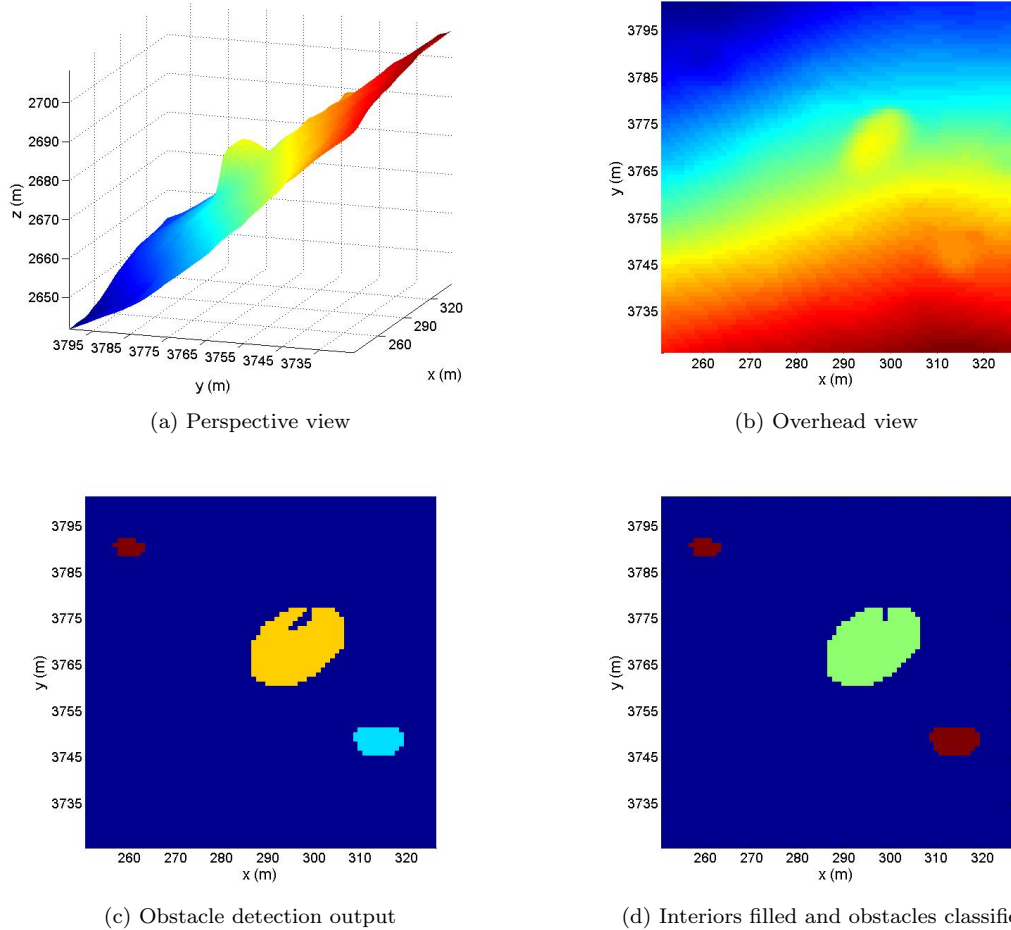


Figure 4.6: 4.6a and 4.6b show a section of steep terrain ($\alpha \approx -45^\circ$) from the Shackleton crater data. The modified obstacle detection algorithm was run with parameters $H_{min} = .1$ m, $H_{max} = 3$ m, and $\theta_{max} = 40^\circ$. 4.6c shows three groups of compatible points, represented by the red, light blue, and yellow colors. Obstacle-free points are shown in dark blue. 4.6d shows the obstacles with their interiors filled. The “negative” obstacles are shown in red and the “positive” obstacle is shown in green.

platform, and so it is assumed that the coordinates of the mother ship are given. The tether is fixed to the anchor, but its geometry is otherwise governed by its interaction with the terrain and with the robot. Likewise, the coordinates of a goal location, \mathbf{g} , are given.

Definition 4.5 (Extreme Terrain Motion Planning). Given a terrain model consisting of tether-free and tether-demand intersecting planes, a set of obstacles, an initial tethered robot configuration and tether anchor point, the solution to the *extreme terrain motion planning problem* is a feasible round-trip path from the anchor point to the goal configuration and back.

In some cases, more than one feasible path may exist, and thus an optimal path could be chosen based on different criteria, such as “safest” or “shortest.” Here, a feasible path is one where, to the resolution of the available terrain model and surface characteristics, *Axel* is controllable at all times during descent and ascent.

4.5.2 Ascent/Descent Approach

Within the tether-free regions, assuming that it is possible to pay out the tether at the same rate that the rover moves, one can use existing motion planning algorithms (e.g., [68]) to compute feasible paths. Motion planning in the tether-demand planes requires more consideration.

Tethered robot ascent of steep slopes is generally more difficult than descent. Working against gravity, terrains with little or no traction can be very difficult to traverse, and it can be easy for a rover to become stuck underneath an obstacle. Additionally, while executing a tethered ascent, a robot’s motion is constrained in that it is unable to deviate much from the path of the tether.

For the reasons just stated, not all feasible descent paths will be feasible ascent paths. Therefore, the set of all possible descent paths will generally be much larger than the set of viable ascent paths. Thus, in order to reduce the computational complexity of the planning problem and to structure the search space, the feasible ascent paths are computed first. Safe descent paths are then searched for within the set of paths whose initial tether configurations are *homotopic* (smoothly deformable) to the tether configuration of ascent paths.

4.5.3 Ascent Path Planning

To climb a tether-demand plane, *Axel* must reel in its tether until it is taut and use the cable’s tension to travel up the steep slope. The shape of the taut tether is very important to the robot’s ascent since it will dictate the direction in which this upward force is applied. For simplicity, it is assumed that the contact between the tether and the ground is frictionless. This ignores “frictional” obstacles, or snagging points that may occur in areas of high surface friction. With this assumption, the taut tether geometry will be the shortest obstacle-free path from the anchor to the robot. Hence, one can compute the configuration of a taut tether given a slack configuration by finding the

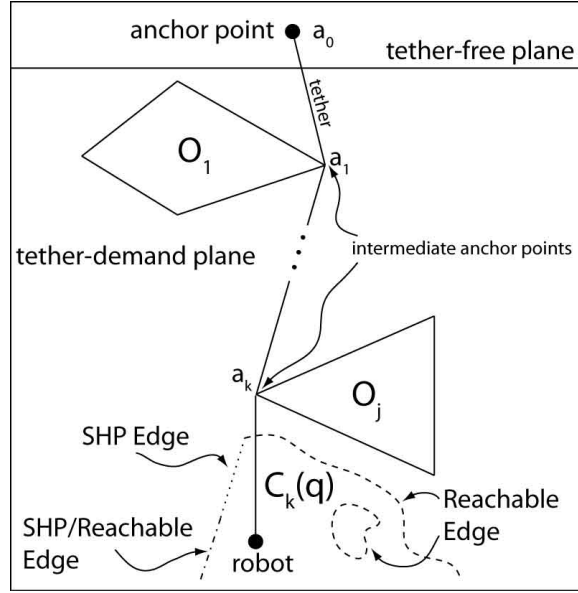


Figure 4.7: Top view of intersecting tether-demand and tether-free planes with obstacles and intermediate anchor points. The dotted sections represent the edges of the *anchor reachable set* (see Definition 4.8).

shortest homotopic path (SHP) from the anchor to the robot's configuration. In other words, this is the shortest path that is smoothly deformable to the tether's geometry (without passing through an obstacle). An algorithm for computing the SHP in a 2D plane with obstacles can be found in [31]. Aspects of this algorithm's construction will be summarized in Section 4.5.4.

Once the SHP from the anchor to a given robot configuration has been computed, one next identifies the *intermediate anchor points*, which are needed to determine whether or not a given ascent is feasible.

Definition 4.6. An *intermediate anchor point* is a point at which the taut tether contacts one or more of the obstacles, O_1, \dots, O_N .

Starting with the anchor point, \mathbf{a}_0 , the *intermediate* anchor points, $\mathbf{a}_1, \dots, \mathbf{a}_k$, are indexed in increasing order along the tether from the anchor point (Figure 4.7). For a given configuration and SHP, it is necessary to determine whether or not the steep terrain rover can navigate around the sequence of intermediate anchor points and ascend back to the tether-free plane, which motivates the following definition.

Definition 4.7. (Passability) An intermediate anchor point, \mathbf{a}_j , is *passable* from robot configuration q if, given q and an SHP with anchor points $\mathbf{a}_0, \dots, \mathbf{a}_j$, the robot can reach a configuration which removes \mathbf{a}_j from the SHP and makes \mathbf{a}_{j-1} the most immediate anchor point.

With Definitions 4.6 and 4.7, the ascent path planning problem simplifies to finding a taut tether configuration containing a sequence of passable anchor points between \mathbf{g} and \mathbf{a}_0 .

```

Input: Terrain model, obstacles  $O_1, \dots, O_N$ , anchor  $\mathbf{a}_0$ , goal  $\mathbf{g}$ 

1. Preprocess terrain into tether-demand, tether-free regions;
2. Construct  $\{\mathcal{S}_i(\mathbf{a}_0, \mathbf{g})\}$  (Set of SHPs connecting  $\mathbf{a}_0$  to  $\mathbf{g}$ );
3. Extract intermediate anchor points  $\{\mathbf{a}_{i,j}\}$  in  $\{\mathcal{S}_i(\mathbf{a}_0, \mathbf{g})\}$ ;
4.  $\mathbf{S}^{\text{feas}} = \{\}; N_{\text{feas}} = 0;$  % set of feasible ascending paths
5. For  $i=1$  to  $N_S$  % find feasible ascending paths
    Continue=true;  $q = \mathbf{g}; j = A_i;$ 
    While (Continue)
        Construct  $C_{i,j}(q);$ 
        If ( $\mathbf{a}_{i,j}$  is passable)
             $j=j-1;$  % advance to next intermediate anchor
            If ( $j=0$ ), % path to anchor exists
                 $\{\mathbf{S}^{\text{feas}}\} = \{\mathbf{S}^{\text{feas}}\} + \mathcal{S}_i(\mathbf{a}_0, \mathbf{g}); N_{\text{feas}} = N_{\text{feas}} + 1;$ 
                Continue=false;
            Else Select  $q \in$  SHP edge;
        Else Continue=false; %  $\mathcal{S}_i(\mathbf{a}_0, \mathbf{g})$  not feasible
6. If ( $N_{\text{feas}} > 0$ ) % feasible ascending paths exist
    For  $i=1$  to  $N_{\text{feas}}$  % construct descending paths
        Find safe descending subset of sleeve( $\mathbf{S}_i^{\text{feas}}$ );
        Plan path from  $\mathbf{a}_0$  to  $\mathbf{g}$  in safe sleeve( $\mathbf{S}_i^{\text{feas}}$ );
    Else report failure. % no feasible ascent exists

Output: A set of controllable descent/ascent paths, or failure.

```

Figure 4.8: Pseudo-code of the steep terrain tethered robot planning algorithm

Finding the set of all feasible ascents can now be accomplished with two steps. First, one computes all of the SHPs connecting the anchor, \mathbf{a}_0 , to the goal, \mathbf{g} . Algorithms for finding the shortest path of a given homotopy type already exist [31, 56] (see Section 4.5.4 for a summary of one such algorithm). This problem is simplified by restricting the SHP search to only consider shortest paths which do not wind around an obstacle, since it is generally hazardous to encircle terrain features with the rover's tether. Let $\{\mathcal{S}_i(\mathbf{a}_0, \mathbf{g})\}$, $i = 1, \dots, N_S$, denote this set of taut tether paths connecting \mathbf{a}_0 to \mathbf{g} . Assuming a finite number of obstacles, N , in the region of interest, N_S is finite. Likewise, there are a finite number of intermediate anchor points, A_i , in path $\mathcal{S}_i(\mathbf{a}_0, \mathbf{g})$.

The second step is then to determine whether or not the intermediate anchors of $\mathcal{S}_i(\mathbf{a}_0, \mathbf{g})$ are passable, which can be accomplished with the help of one more definition.

Definition 4.8 (Anchor Reachable Set). Given the j th anchor point of the i th SHP, $\mathbf{a}_{i,j}$, the *anchor reachable set*, $C_{i,j}(q)$, is the set of points that are reachable from the robot configuration, q , while it is tied to anchor $\mathbf{a}_{i,j}$.

Generally, the anchor reachable sets will depend upon the SHP, the terrain angle, the terrain traction model, and the robot's dynamic capabilities.

Anchor reachable sets have three types of edges: 1) an edge which, when crossed, changes the list of anchor points in the SHP (SHP edge), 2) an edge which is the limit of reachable configurations (reachable edge), and 3) an edge which may be both (1) and (2). In Figure 4.7, the SHP edge

is the dotted line, the reachable edges are the dashed lines, and the SHP/Reachable edge is the dotted-dashed line.

From the definitions presented in this section, it should be evident that the intermediate anchor point $\mathbf{a}_{i,j}$ is passable if $\mathcal{C}_{i,j}(q)$ has an SHP edge which, when crossed, makes $\mathbf{a}_{i,j-1}$ the most immediate anchor point. Once an intermediate anchor point is found to be passable, the crossed SHP edge is used to calculate a starting configuration, q for the analysis of the following reachable set. Optionally, q becomes set-valued as the starting point for the computation of $\mathcal{C}_{i,j-1}(q)$.

If all intermediate anchor points of $\mathcal{S}_i(\mathbf{a}_0, \mathbf{g})$ are passable, a kinodynamic motion planning algorithm [41] can be used to search for feasible or optimal paths from \mathbf{g} to \mathbf{a}_0 within the space of the associated reachable sets.

The descent path planning problem is similar to the ascent planning problem except that it is further constrained to consider only paths which are homotopic to the feasible ascent paths, $\{\mathcal{S}_i^{feas}(\mathbf{a}_0, \mathbf{g})\}$. As described in Section 4.5.4, the *sleeve* framework of Hershberger and Snoeyink [31] is used to search for descent paths within the feasible ascent homotopy class.

In summary, the basic tethered robot steep terrain motion planning algorithm can be summarized with the pseudo-code presented in Figure 4.8. The next sections will provide additional technical details regarding the key steps of the planning algorithm.

4.5.4 Homotopies of Ascending Paths

Constructing the taut tether configuration and preprocessing the terrain for efficient descent planning requires that the tether-demand regions are triangulated as a *boundary triangulated 2-manifold*. Recall that a two-dimensional *simplicial complex* is a triangulated 2-manifold. In other words, it is a collection of triangles, edges, and vertices such that individual triangles may have only three relations: 1) no intersection, 2) intersection at a vertex, or 3) intersection at two vertices and a common edge. A *boundary-triangulated 2-manifold* (BTM) is a simplicial complex in which all vertices are incident to two *boundary edges*. Boundary edges are incident only to a single triangle. Practically, boundary edges form the boundaries of the tether-demand regions or the edges of bounding obstacles. Figure 4.9 shows the tether-demand plane of Figure 4.7 triangulated as a BTM. De Berg et al. [29] provide an efficient algorithm for constructing a BTM from an arbitrary polygon, which is summarized here.

Constructing the BTM from a two-dimensional polygon object can be summarized in two steps: 1) partition the polygon into monotone pieces, and 2) triangulate the monotone polygon pieces.

Definition 4.9 (Monotone Polygon). [29] A simple polygon (polygon with no holes) is called *monotone* with respect to a line L if for any line L' perpendicular to L the intersection of the polygon with L' is connected.

In other words, the intersection between the polygon and L' should be a line segment, a point, or

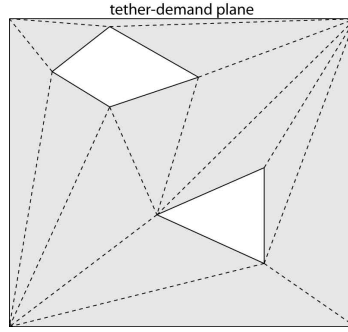


Figure 4.9: The tether-demand plane of Figure 4.7 processed into a boundary triangulated 2-manifold (BTM)

empty. As a specific case, a polygon that is monotone with respect to the y -axis is called *y-monotone*. Clearly, then, the given polygonal terrain region with obstacles (holes) will not be monotone, and so this step must be performed before the region can be triangulated.

Dividing the polygonal terrain region into monotone pieces is performed by drawing a horizontal line and scanning the vertices of the polygon with this line from top to bottom. As the scan progresses and encounters a polygon vertex, diagonals are drawn between vertices according to the specific nature of the vertex until all the partitions are y -monotone.

For the second step, the vertexes are similarly scanned downward in order of decreasing y -coordinate, but this time a greedy triangulation is implemented, and as many diagonals are drawn as possible. De Berg et al. showed that this algorithm takes $\mathcal{O}(n \log n)$ time, where n is the number of vertices in the polygon.

The reason the BTM is useful is because it leads naturally to the construction of a *sleeve*. Recall first that a *simple path* is a curve that does not cross itself. As mentioned in Section 4.5.3, only simple paths are considered, since rover operators want to avoid paths that form closed loops around obstacles.

Definition 4.10. [31] A *sleeve* is a triangulated simple polygon whose dual tree is a simple path.

An example showing how sleeves are constructed will serve to clarify Definition 4.10. Using the BTM presented in Figure 4.9, Figure 4.10 shows numbered triangle faces and a circuitous path drawn in red. The tree of the path is shown in Figure 4.10b. The sleeve of the red path is constructed by moving up the tree from the end-face to the start-face, which is highlighted in red. Since the sleeve is a simple polygon, it has the useful property that any two simple paths in the same sleeve with the same endpoints must be homotopic. Sleeves can therefore represent the homotopy class of the tether configuration during ascent.

Figure 4.11 shows the four possible sleeves for the BTM presented in Figure 4.9. These sleeves represent the four unique homotopy classes of paths connecting the top of the tether demand region to the robot configuration. All tether paths within the sleeve of $\mathcal{S}_i(\mathbf{a}_0, \mathbf{g})$, denoted by $sleeve[\mathcal{S}_i(\mathbf{a}_0, \mathbf{g})]$,

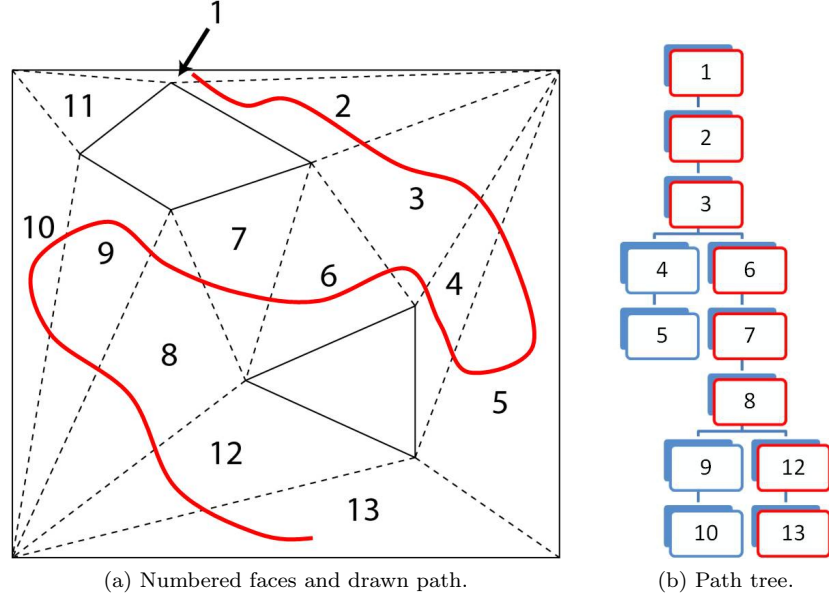


Figure 4.10: The BTM of Figure 4.9 is shown in 4.10a with triangular faces numbered and a circuitous path drawn in red. The tree of the red path is shown in 4.10b. The sleeve of the red path is constructed by moving up the tree from the end-face to the start-face (red highlight).

will deform to $\mathcal{S}_i(\mathbf{a}_0, \mathbf{g})$ when the tether is pulled taut. The shortest path in a simple polygon can be readily found. It is worth noting that given a slack tether shape, the associated SHP (taut tether configuration) can be found from the sleeve construction [31].

Let $\mathcal{S}_i^{feas}(\mathbf{a}_0, \mathbf{g})$ denote the i th feasible ascent SHP (all of its intermediate anchor points are passable). After all feasible ascent paths, $\{\mathcal{S}_j^{feas}(\mathbf{a}_0, \mathbf{g})\}$, $j = 1, \dots, N_{feas}$ are found, the search space for descending paths is limited to the sleeves of the feasible ascent paths, e.g., one of the shaded regions of Figure 4.11. As described in Section 4.5.5, this space can be further refined by looking only at the subsets of these regions where the rover is safe and controllable. If no suitable descent path can be found within this space, the search can be expanded to include triangles adjacent to the sleeve, so long as the path returns to the sleeve through the same triangle edge from which it left. This will ensure homotopy to the ascent configuration when the tether is pulled taut.

4.5.5 Constructing Anchor Reachable Sets

During the ascent phase, the step terrain motion planning algorithm requires calculation of the anchor reachable sets to assess if an intermediate anchor point is passable. In the descent phase, it is useful to determine the subsets of the sleeves where the vehicle is likewise safe and controllable. In general, constructing anchor reachable sets of nonlinear control systems is a difficult task and depends upon the dynamic capabilities of the robot, its configuration on the terrain, a terrain-vehicle interaction model, and the geometry of the tether.

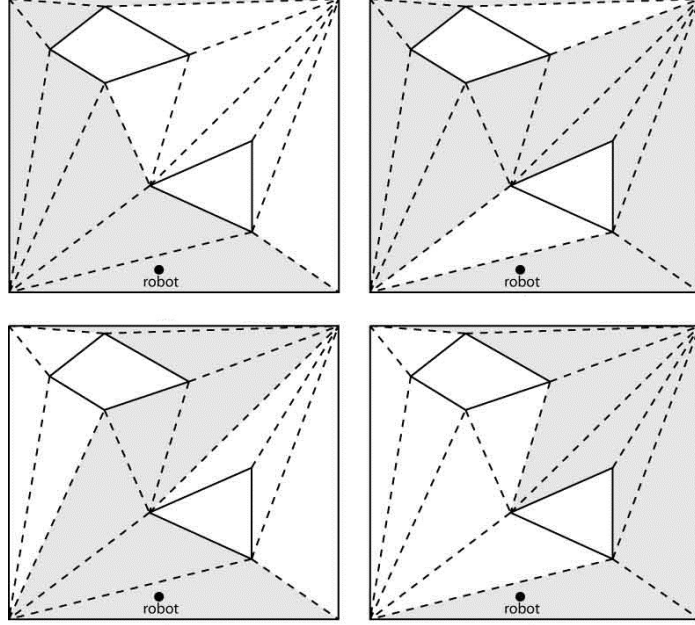


Figure 4.11: The shaded grey regions represent the four possible sleeves of Figure 4.9 running from the top of the tether-demand plane to the robot configuration.

To obtain the correct equations of motion, one must first determine the correct dynamic model and then apply the appropriate constraints as detailed in Section 4.2.2. If *Axel* is assumed to move quasi-statically, the equations of motion can be simplified:

$$\ddot{q} = M^{-1}(T - G - C^T \Lambda) \quad \text{and} \quad (4.39)$$

$$\Lambda = [CM^{-1}C^T]^{-1} [CM^{-1}(T - G)], \quad (4.40)$$

and the rover's motions can be approximated by $\dot{q} \approx \ddot{q}\Delta t$ for small time Δt . Thus, *Axel* can locally ascend the tether-demand plane if there exists at configuration q a feasible set of motor torques, $T(q, \dot{q})$, such that $\ddot{q}\Delta t$ produces velocities which displace *Axel* towards the SHP edge of the anchor reachable set. The SHP edge of a given anchor reachable set is easily computed by extending the penultimate line segment of the shortest homotopic path.

A distinction should be made here between this small time displacement towards the SHP edge and the classical notion of controllability. The simplified calculation presented above is meant to serve as a means to compute passability in the cases where constructing the full anchor reachable set is impossible or impractical. In addition, it will usually not be necessary to determine if the rappelling rover is fully controllable at a given configuration, since many rover displacements will not serve to untangle the tether from the most immediate anchor point. The problem of constructing

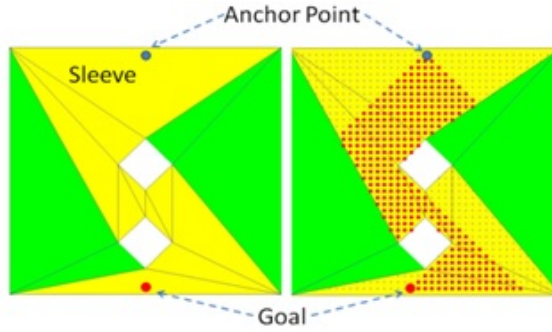


Figure 4.12: Computational example of *Axel* controllability calculation in one sleeve of a tether-demand plane. Left image shows the goal and anchor point with obstacles in white and one sleeve highlighted in yellow. The dots in the right image represent grid points in the sleeve, and the red circles depict the controllable/safe subset of the sleeve based on a maximum deviation angle from the nearest intermediate anchor point.

the full anchor reachable set is therefore simplified by restricting the local controllability calculation to only consider motion towards the SHP edge. Future references to “controllability” will refer to this notion of controllability in the direction of the SHP edge.

A similar analysis can be used during descent planning to prune the geometry of the sleeve down to the subset of safe and controllable rover configurations. In practice, the anchor reachable sets for ascent and the pruning procedure during descent planning are computed on a grid. Terrain data from an orbiter, for example, will often only be available in grid format. Because controllability depends on the SHP, each sleeve corresponding to a feasible ascent path, \mathcal{S}_i^{feas} , is discretized, and the controllability calculation is performed at each point on the grid. Figure 4.12 shows a computational example of such a discretized calculation for the sleeve of one ascending SHP, where the rover is assumed to be controllable within some maximum deviation angle from the vertical of the nearest intermediate anchor point.

Finally, the dynamic model, with the tether reaction force removed, can be used to predict if the rover is mobile at a given posture, q . This analysis can be used to classify the planes as either tether-demand or tether-free regions.

4.6 Simple Example

A simple example will help to illustrate the concepts presented in this chapter. Let the terrain model be given as in Figure 4.13 with the anchor point placed near the border between a horizontal and an inclined plane. Obstacles and a goal are located on two adjacent inclined planes, one at angle α_1 and the other at angle α_2 relative to the horizontal, where $\alpha_1 < \alpha_2$. In this example, the robot is modeled as a simple point mass with Coulomb friction governing its interaction with the terrain.

The first step is to identify the horizontal plane as a tether-free plane and the two inclined planes

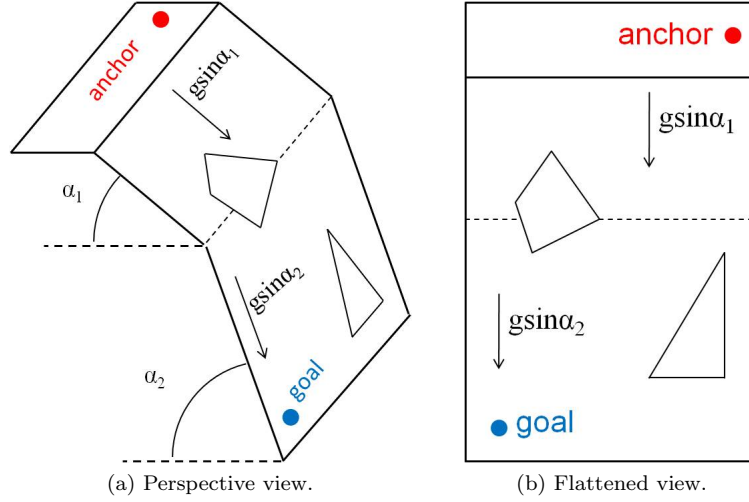


Figure 4.13: Example terrain in perspective and flattened views. $\alpha_1 < \alpha_2$.

as tether-demand planes. Next, compute the anchor reachable sets to find the viable ascent paths. Assuming quasi-static robot motion, then the reachable edges of the anchor reachable sets will occur at the points where the point mass robot will start to slip in static equilibrium. A straightforward calculation shows that this relation is given by

$$|\theta_i^{max}| = \sin^{-1}(\mu \cot \alpha_i). \quad (4.41)$$

The variable θ_i^{max} is the maximum angle from the vertical to the straight line connecting the robot to the nearest anchor point, α_i is the slope angle for $i = 1, 2$, and μ is the coefficient of friction between the robot and the terrain. Figure 4.14 shows some of the anchor reachable sets in this terrain model. θ_1^{max} is the maximum up-slope tether angle for the first tether-demand plane, and θ_2^{max} is the analogous value for the second tether-demand plane, which is at a steeper angle relative to the horizontal.

Following the algorithm presented in Section 4.5, it is clear that the only continuous sequence of passable intermediate anchor points from the goal to \mathbf{a}_0 is $[\mathbf{a}_1 \ \mathbf{a}_2]$, as shown in Figure 4.14. Next, compute the BTM of the tether-demand planes and search for a path within the ascent sleeve based on an optimization criterion, in this case the shortest path (Figure 4.15).

At first glance the naïve shortest path from the anchor point to the goal may seem very desirable because it completely avoids contact between the tether and the obstacles. The anchor reachable sets, however, indicate that this path does not guarantee the robot's safety on this steep terrain. Instead, by taking advantage of the passable anchor points the rover can find a safe path to the goal and back to the anchor point.

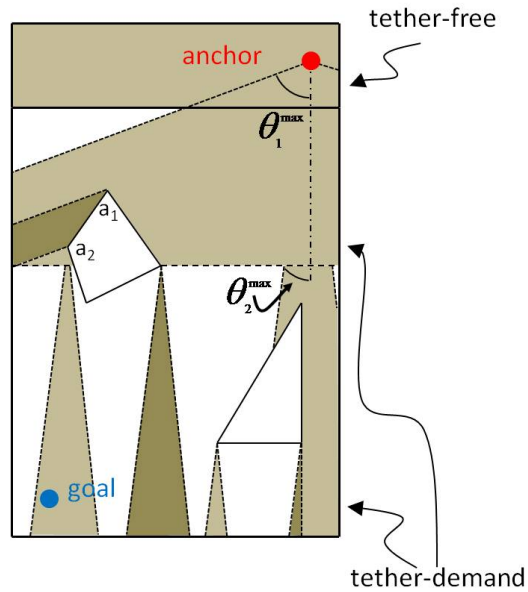


Figure 4.14: Shaded regions represent some of the anchor reachable sets for the terrain model. Different shadings distinguish between adjacent anchor reachable sets.

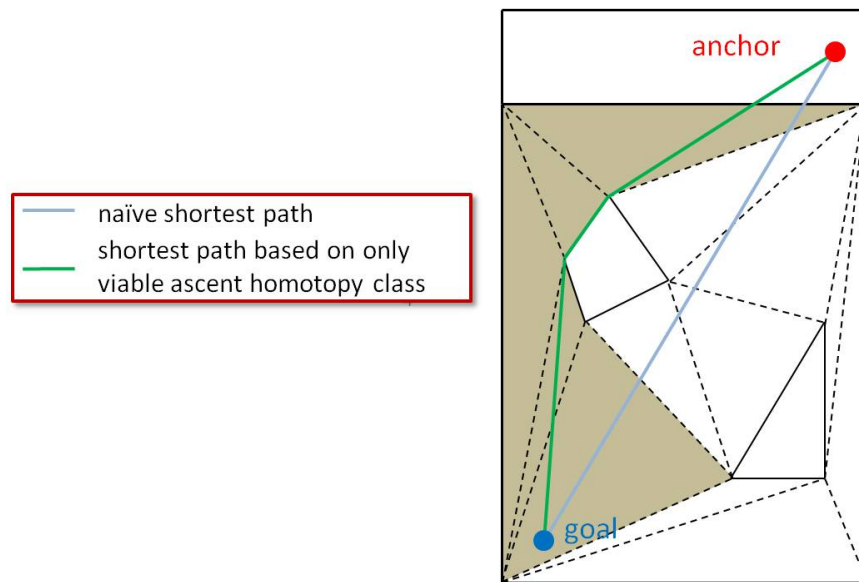


Figure 4.15: Dashed lines show the BTM of the terrain, and the shaded region is the sleeve of the viable ascent path. The blue line is the naïve shortest path from anchor to the goal, while the green line is the shortest path within the only viable ascent homotopy class.

4.7 Shackleton Crater

This section combines the chapter's previous discussions to generate a path plan from the LRO's elevation map of the Shackleton crater. As mentioned previously, the crater is an excellent example of a potential science target, but it can also easily serve as an analogue for many other extreme terrains. Thus, the goal of this section is to perform a hypothetical crater descent in order to one day supplement *Axel* with the needed on-board intelligence to prepare the rover for deep crater excursions.

Figure 4.2 shows the macroscopic data of the Shackleton crater while Figures 4.5 and 4.6 show details of the terrain. From the elevation map one can see that, typical of impact craters, there is a slight upslope just before the long descent to the bottom. It is assumed that *Axel* or *DuAxel* (see Chapter 6) could navigate its way to the crest of the crater without the aid of a tether. Recent field experiments, in which *DuAxel* traversed 35° inclines, lend credence to this assumption (see Section 6.4).

Starting from the crest ($y = 1$ km), the objective is to traverse to a hypothetical goal location approximately halfway down the slope of the crater, between $y = 4$ km and $y = 5$ km. Although the crater goes much deeper, *Axel* is limited in traversal distance by the length of its tether. Many complications arise with added lengths of tether, including, but not limited to, increased electrical resistivity, added heat loss, higher overall mass, and excess volume requirements. Recent field tests demonstrated successful operation with 200 m of tether, and so the assumption that *Axel* could carry 4 km of tether is optimistic but not altogether unrealistic. Future design work on the rover is sure to address this issue and push the limits of the rover's tether carrying capacity.

As discussed in Section 4.3, the terrain can be modeled as a set of intersecting planes with slope angles α_i , $i = 1, \dots, N$, where N is the number of planes. Given that the data has 1 m resolution along both the x and y axes, the terrain from $y = 1$ km to $y = 5$ km is divided into $N = 4,000$ planes, each $1 \text{ m} \times 1,000 \text{ m}$ in dimension. The slope angle, α_i , of each plane is given by computing the average slope of the 1,000 points that lie at the same y coordinate.

Given this terrain model, the next step is to use the obstacle detection algorithm outlined in Section 4.4 to calculate the location of all the positive and negative obstacles. Using the parameters correlating to *Axel*'s dimensions and capabilities ($H_{min} = .1$ m, $H_{max} = 3$ m, and $\theta_{max} = 40^\circ$, see Section 4.4 for details), the output of the sloped terrain obstacle detection algorithm can be seen in Figure 4.16a. A positive obstacle is defined as one in which the average elevation of the points immediately surrounding the obstacle is lower than that of the points in the obstacle. A filter showing only the positive obstacles is shown in Figure 4.16b. A total of almost 1,500 distinct obstacle groups were detected by the algorithm, of which approximately 25% were positive.

Next, the region containing the positive obstacles is converted into a boundary triangulated

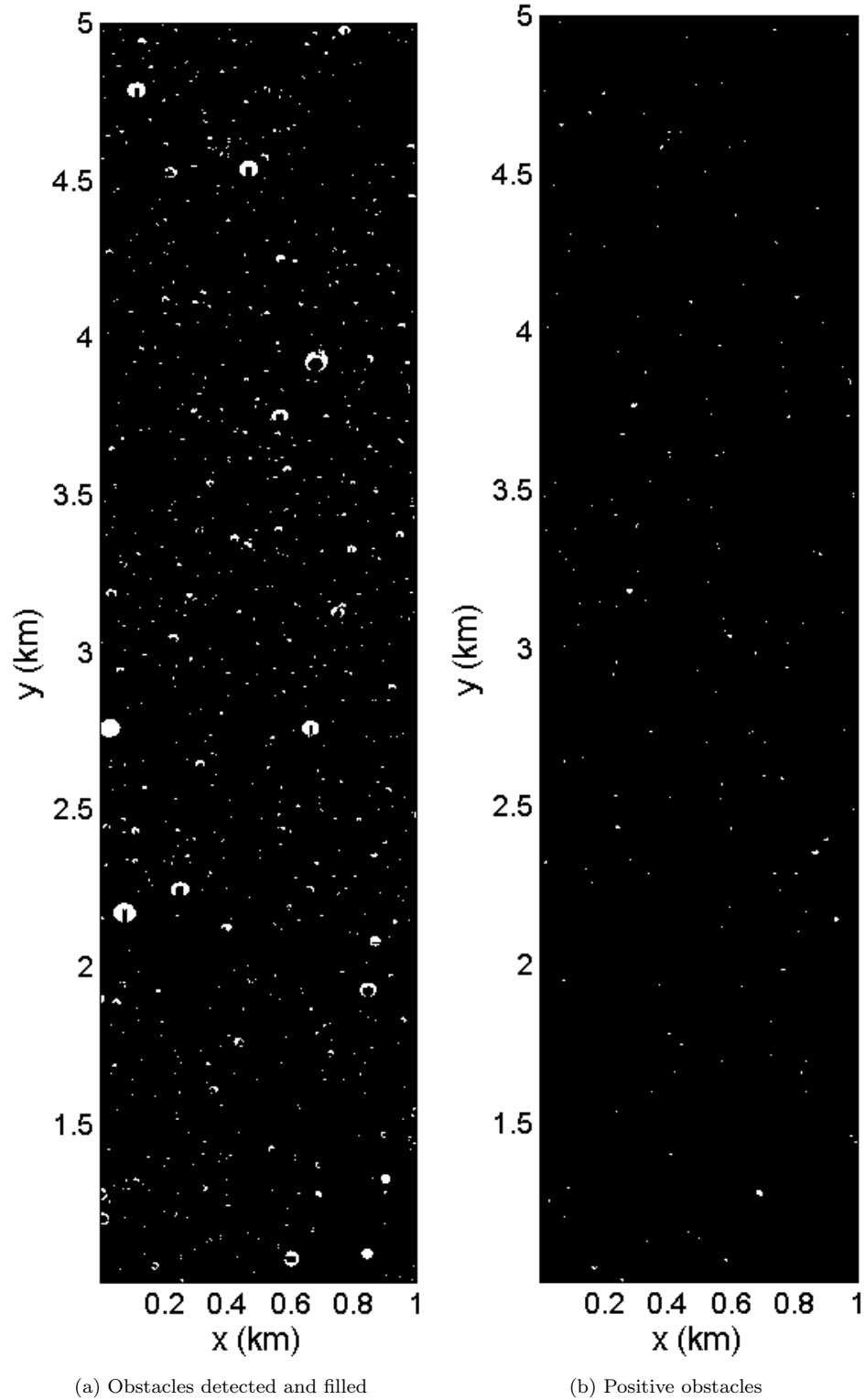


Figure 4.16: Figure 4.16a shows the output after the obstacles have been detected and filled. Black regions are obstacle-free while the light regions contain obstacles. Figure 4.16b shows only the positive obstacles. Almost 1,500 distinct obstacle groups were detected, of which approximately 25% of them were positive obstacles.

manifold using any of a number of triangulation algorithms. This analysis used the triangulation method put forth by de Berg et al. in [29] and summarized in Section 4.5.4, although Chazelle’s algorithm [27], for example, would also be a valid alternative. The full BTM is presented in Figure 4.17 and close-details of the traingulation are shown in Figure 4.18.

With a start and goal location separated by over 300 positive obstacles, there are many different sleeves in the associated BTM. Most of these sleeves, however, do not represent realistic homotopy classes for a rover path. For example, any sleeve that has the rover traversing directly across the plane from $x = 0$ km to $x = 1$ km would be difficult to realize in practice. Given an anchor point $\boldsymbol{\rho}_a = [550, 1100]^T$ and a goal location $\mathbf{g} = [500, 4700]^T$, a few candidate sleeves are presented for the reader in Figure 4.19.

Next, the sleeve is discretized every 1 m along the x and y-coordinates, the SHP from each point in the sleeve to the anchor location is computed, and a static controllability test is implemented according to Equation 4.41, with $\mu = .3$ approximating the lunar friction coefficient. Using the “central path” sleeve of Figure 4.19a, the anchor reachable sets from the goal location to the anchor are computed and represented in Figure 4.20. The red region represents the union of all the anchor reachable sets, the green and black diamonds represent the anchor and goal locations, respectively, and the yellow “holes” in the red region are the negative obstacles.

Anchor reachable sets corresponding to smaller and larger values of the coefficient of friction, μ , can be seen in Figure 4.21. When the rover has less traction (smaller μ), the anchor reachable sets become narrower (Figure 4.21a), while more traction allows *Axel* to access a larger subset of the sleeve (Figure 4.21b). These computations show a simple controllability calculation using the simple Coulomb model, however one could easily apply an arbitrarily complex controllability model based on the rover’s dynamics and available terrain data.

Using the discretized reachable configurations, it is now straightforward to compute a round-trip path (anchor to the goal and back) using any preferred optimization criteria. Staying within the anchor reachable sets (red region of Figure 4.20), the ascent is guaranteed to be homotopic to the descent path, precluding the possibility of tether ensnarement around an obstacle. Furthermore, by avoiding the edges of the anchor reachable sets, the rover can minimize lateral tether forces and reduce the risk of tip-over. Such a computation would have greatly benefited the *Dante II* rover during its ascent out of the Mt. Spurr volcano.

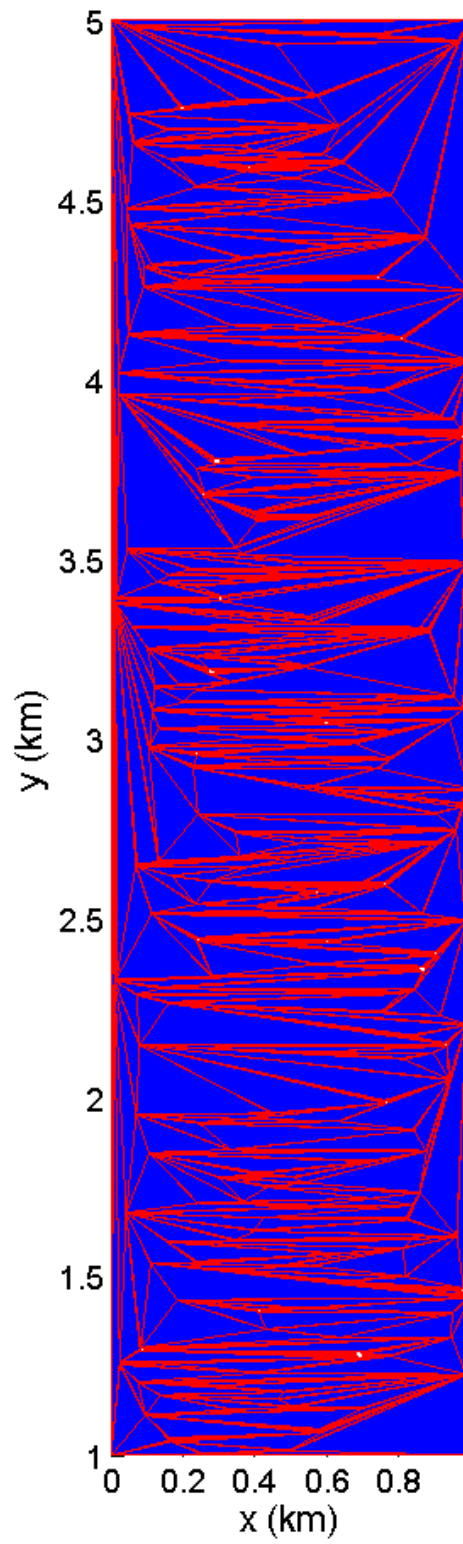


Figure 4.17: The $1 \text{ km} \times 4 \text{ km}$ region of positive obstacles from Figure 4.16b as a boundary triangulated manifold

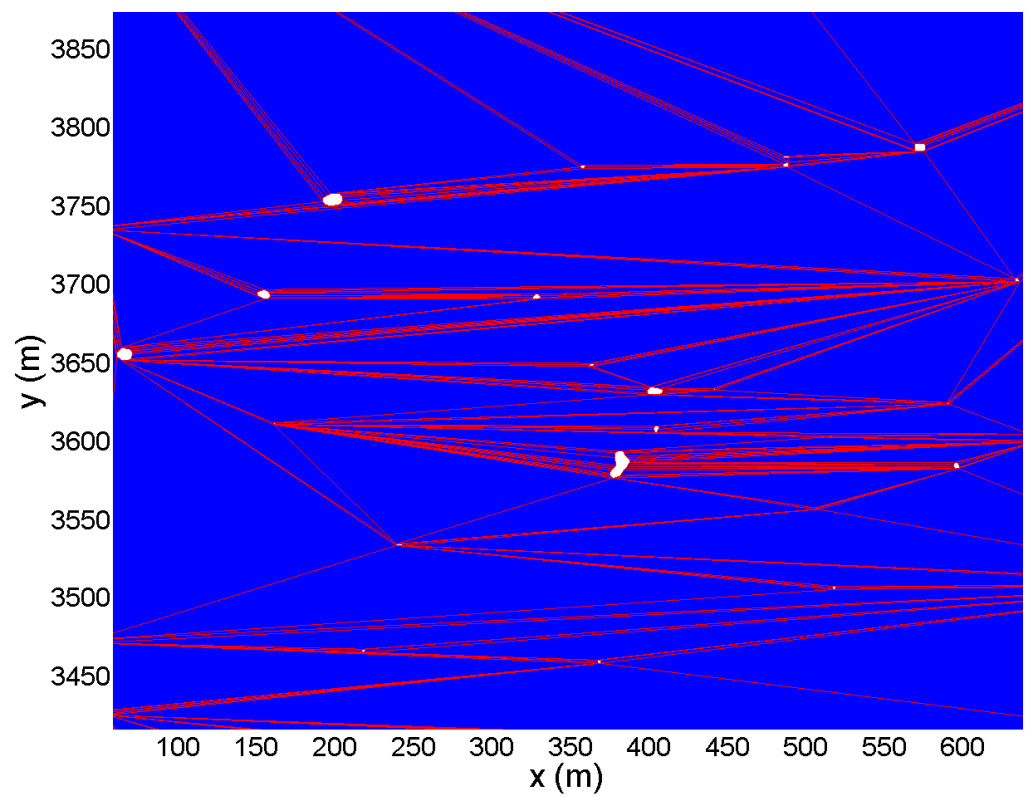
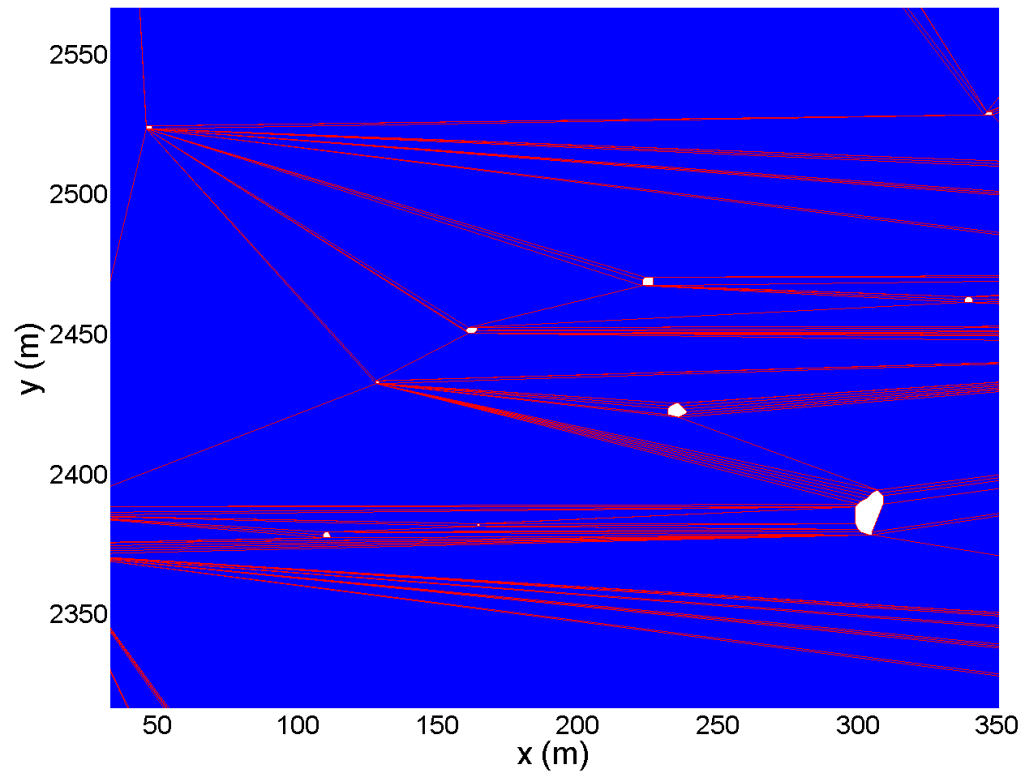


Figure 4.18: Details of the BTM presented in Figure 4.17. Blue region is background, red lines form the triangulation, and the white regions are obstacles.

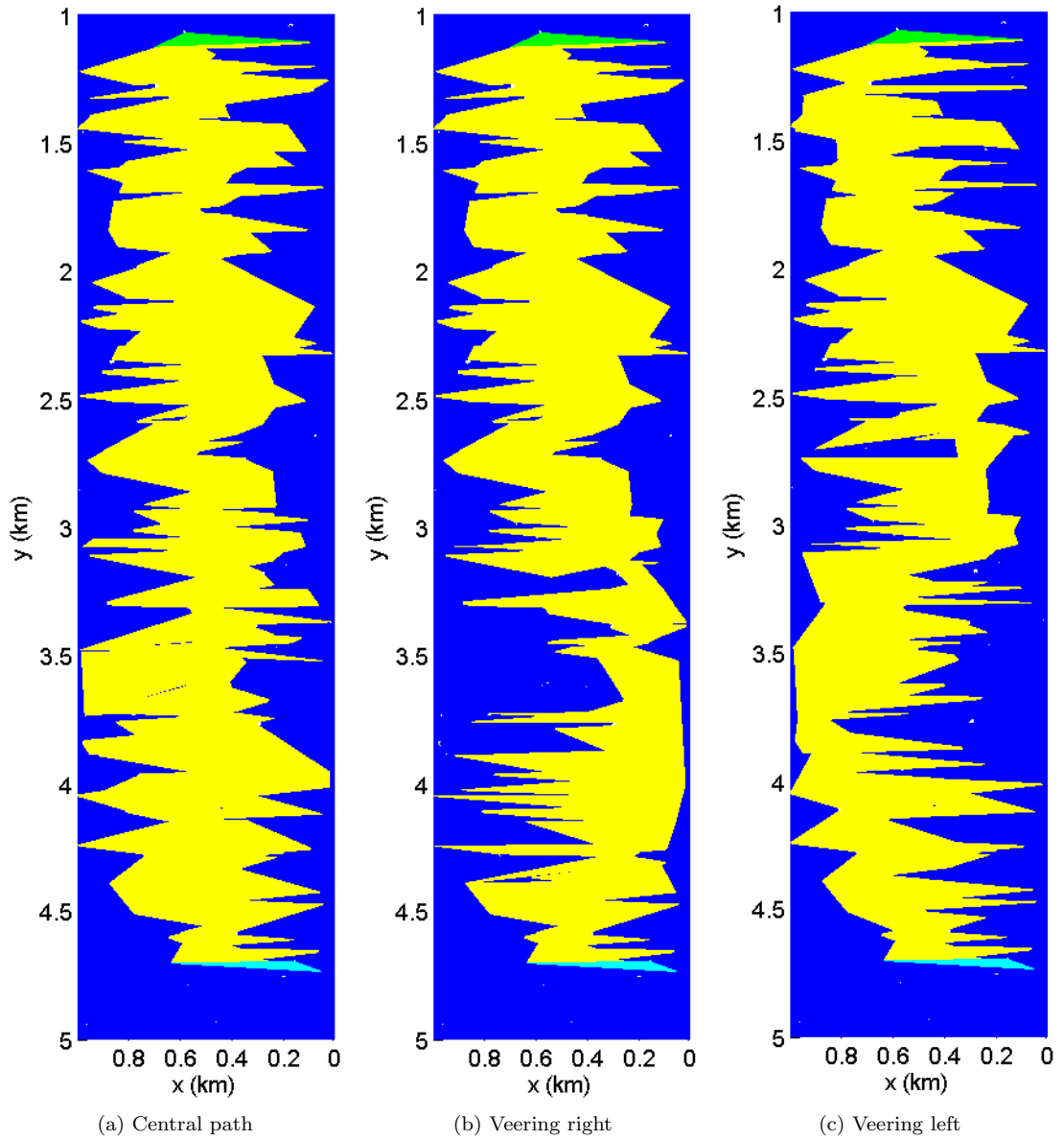


Figure 4.19: A few example sleeves for the BTM in Figure 4.17. The sleeve is given by the yellow fill. The anchor and goal triangles are presented in green and light blue, respectively.

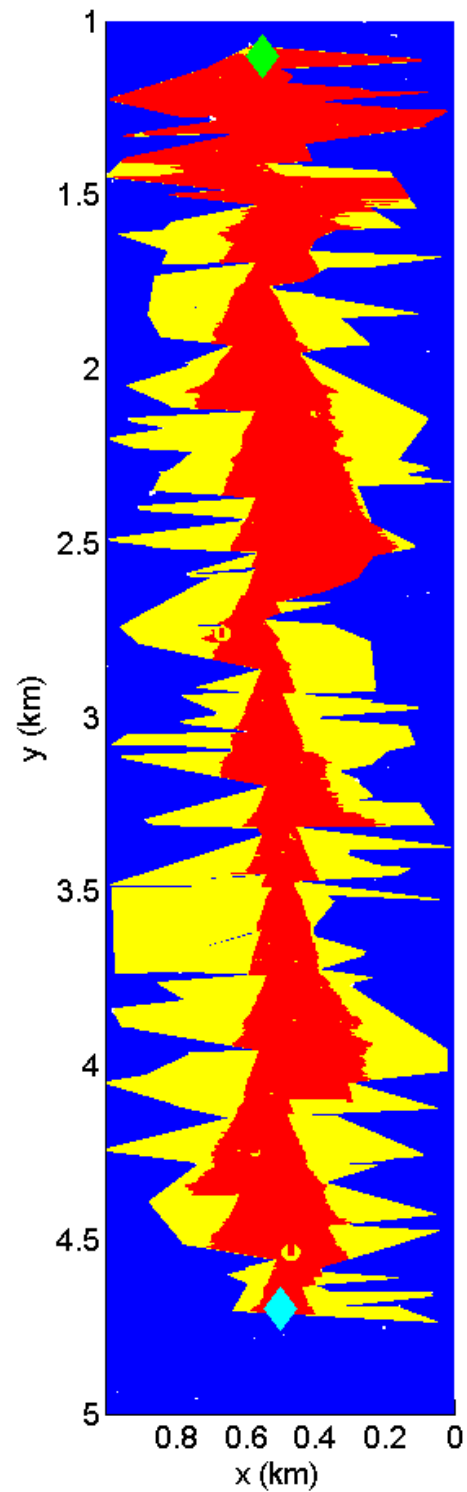


Figure 4.20: The “central path” sleeve from Figure 4.19a is shown here. The red section indicates the region within the sleeve where *Axel* would remain controllable using $\mu = .3$ for Coulomb’s law. Yellow “holes” in the red region demarcate the negative obstacles, which are not part of the anchor reachable sets. The green and light blue diamonds indicate the anchor and goal locations, respectively.

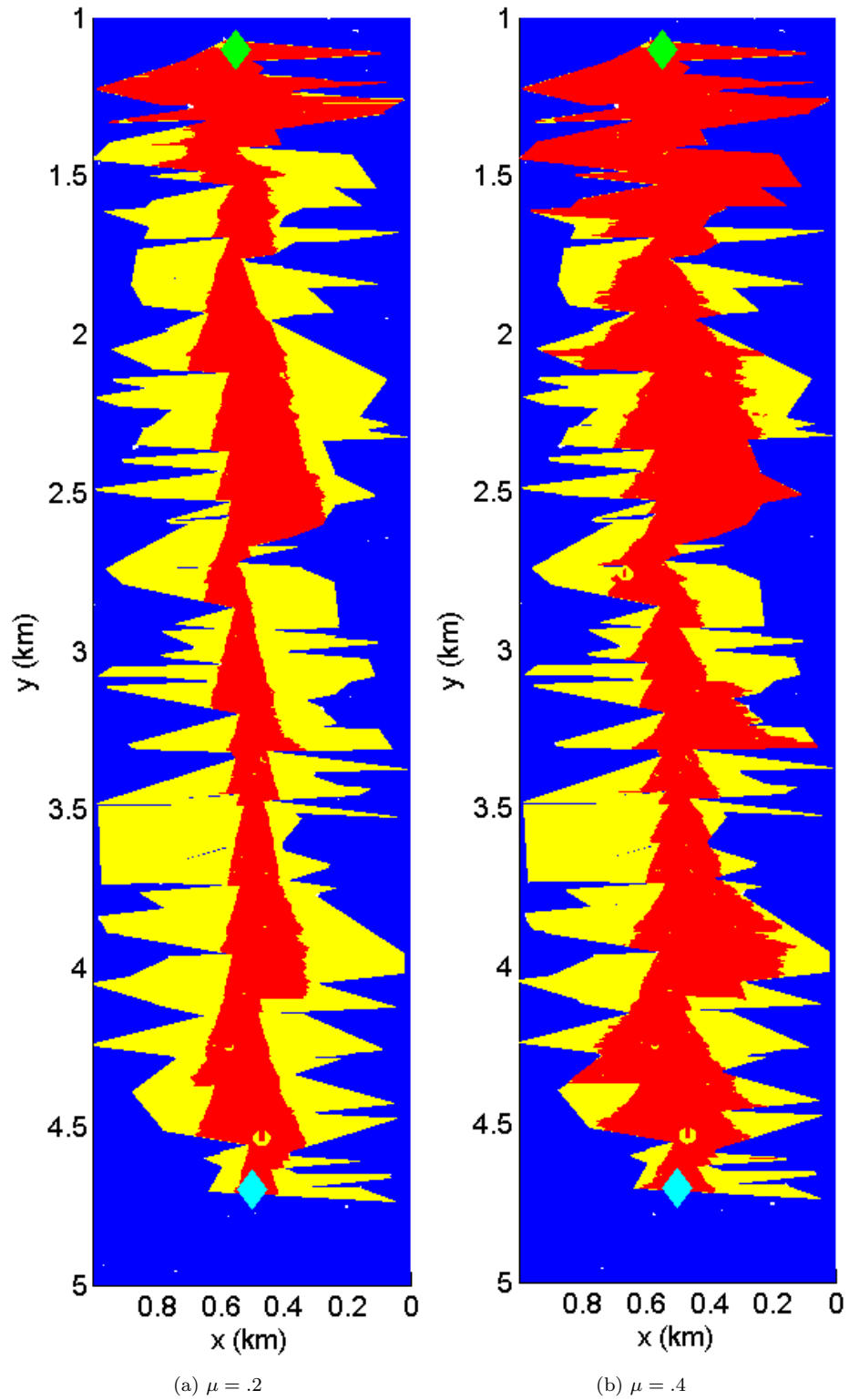


Figure 4.21: Computations of the anchor reachable sets with different levels of traction modeled by varying the coefficient of friction under the Coulomb model. The red section indicates the safe/controllable subset of the sleeve, and the green and light blue diamonds indicate the anchor and goal locations, respectively.

Chapter 5

Tether Tension Prediction

In addition to its wheel design and on-board intelligence, *Axel*'s mobility on extreme terrain is the result of its ability to actively control its tether. By reeling and unreeling the tether, it is able to both ascend and descend steep slopes, and it can even raise itself while free-hanging.

Paramount to extreme terrain mobility is ensuring that *Axel*'s tether never severs due to piercing, abrasion, or overstress. Without the ability to recharge its batteries through power connections in the tether, *Axel* could still potentially function passively on one end of the *DuAxel* (see Chapter 6), but at the bottom of a crater the rover would be left with limited mobility and a diminishing battery supply.

In January of 1993, Carnegie Mellon University, with the support of NASA funding, took their eight-legged rappelling rover, *Dante* (the predecessor to *Dante II*), on an expedition to Antarctica. The target for their field test was Mt. Erebus, the southernmost active volcano on Earth. The rover's tether, which carried both power and communication signals, would serve as *Dante*'s lifeline during the expedition. Upon reaching the lip of the volcano, *Dante* began its descent. Unfortunately, after taking only a few steps, the tether snapped and the entire expedition was brought to an abrupt halt [45].

Understanding the tether forces while maneuvering on sloped terrain is therefore essential to ensuring the safety of the rover. When computed beforehand, configurations that lead to high tether stresses can be avoided, and *Axel* can navigate safely within the cord's tolerances. This chapter models different rover configurations and maneuvers in order to predict the forces experienced by the tether. Doing so provides insight into this key component of *Axel*'s mobility and increases the rover's robustness on extreme terrain.

5.1 Tension on Steep Slopes

A careful examination of wire rope products available on the market will reveal that tensile strength is primarily a function of the diameter of the cable, which, in turn, corresponds to its overall mass.

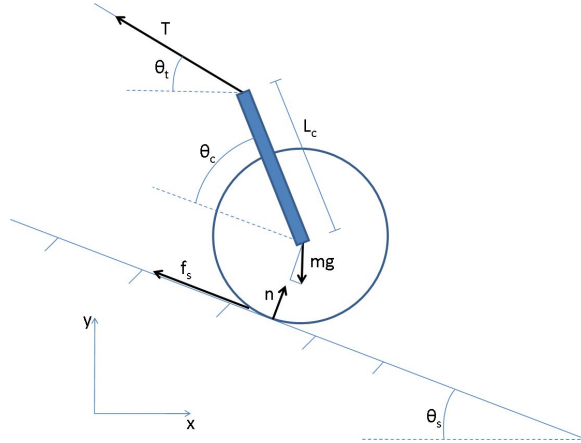


Figure 5.1: Two-dimensional free body diagram of tethered *Axel* on a slope

Robustness to abrasion, on the other hand, is more difficult to quantify and depends mostly on the cable's finish and coating. To begin, a theoretical analysis of the tensile forces experienced by the tether will be presented, which helped to determine the minimum breaking strength required to support the *Axel* rover. The analysis is then validated with a tension experiment conducted in laboratory conditions.

Figure 5.1 offers a two-dimensional free body diagram of a tethered *Axel* on a slope. In a static analysis, the equations of motion are given by Newton's second law. Letting m represent the rover's mass, r_w the wheel radius, g the gravity constant, L_c the caster length, θ_s the slope angle, θ_t the tether angle, and θ_c the caster angle, solving for the tether tension is straightforward and gives the relation

$$T = \frac{m g r_w \sin \theta_s}{L_c \sin (\theta_c + \theta_s + \theta_t) + r_w \cos (\theta_s - \theta_t)}. \quad (5.1)$$

Since the mass, wheel radius, gravity constant, and caster length are all constants, the tether tension is a function of three variables: slope (θ_s), tether angle (θ_t), and caster angle (θ_c).

For a given slope, Matlab was used to compute a matrix of values representing the tension in the tether for reasonable ranges of the tether and caster angles. The results of a typical computation for a 30° slope can be seen in Figure 5.2, where parameter values from the original *Axel 1* hardware were used for the calculations: $m g = 50$ lb, $r_w = 6.5$ in, and $L_c = 27.5$ in. Certain configurations of tether and caster angle were excluded because they do not occur in practice. For example, it would be difficult to realize a situation in which *Axel* is free-hanging on a 90° slope with the caster arm pointed perpendicular to the wall face ($\theta_c = 90^\circ$).

Figure 5.2 shows that there is a large range of configurations where the tether tension will remain below 20% of *Axel*'s weight. The figure also demonstrates that the tether tension will rise dramatically at the extremes of the caster arm angle, θ_c . This configuration occurs in practice when

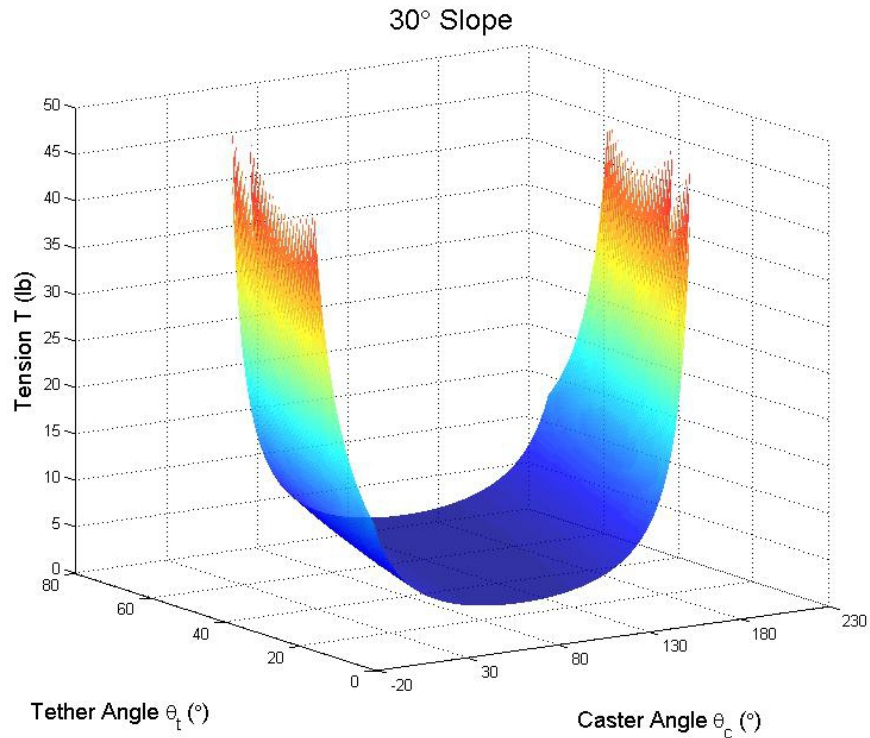


Figure 5.2: Theoretical tether tension on a 30° slope plotted for a range of values θ_c and θ_t

Axel 1 performs a sampling maneuver (see Figures 2.5 and 2.6b). Nevertheless, within an allowable range of caster arm and tether angles, the tension force never rises above the rover’s weight.

To verify the accuracy of this static analysis, an experiment was conducted on *Axel 1* using a 250 lb capacity LC101 tension sensor from Omega Engineering. The sensor was mounted in line with the tether near the anchor point. The output voltage was boosted 101 times using a LM741 op-amp and then displayed on an oscilloscope. During the experiment, *Axel 1* was balanced statically on an angled board and measurements were taken for three different slopes and 5–9 different caster angles. The anchor point for the experiment was kept fixed, and for each caster configuration the tether angle was measured using a digital inclinometer. Table 5.1 shows the data from this experiment¹.

The data matches the theoretical values reasonably well and never deviates by more than 11 lb. High-percentage errors in the lower ranges can be attributed, in part, to the resolution of the sensor itself. Figure 5.3 portrays the measurement data from the 30° slope experiment, represented by the purple line, overlaid on the theoretical prediction given by Equation 5.1.

The experiment suggests that Equation 5.1 can be used to predict the tether tension during different maneuvers on steep slopes. The tether’s required strength can therefore be based on *Axel*’s mass, and rover configurations which produce high stresses in the tether can be avoided. Although the sampling maneuver used in experiments in the JPL Mars Yard leads to sharp rises in the tension

¹Data was collected with the help of Johanna Cecava.

θ_s (°)	θ_c (°)	θ_t (°)	T_m Measured (lb)	T_t Theoretical (lb)	% Error	$ T_t - T_m $ (lb)
30.0	-16.9	16.0	22.28	33.06	32.6	10.79
	-1.6	9.9	12.46	10.94	13.9	1.52
	20.0	2.5	8.99	6.23	44.5	2.77
	57.9	3.3	6.60	4.88	35.2	1.72
	90.0	1.3	8.75	5.43	61.0	3.31
	115.5	2.6	10.07	7.24	39.0	2.83
	145.8	8.8	15.26	13.20	15.6	2.06
	173.0	30.6	19.47	15.94	22.1	3.53
	196.9	51.8	18.98	19.26	1.5	0.28
35.2	-16.1	13.4	21.58	21.34	1.1	0.23
	26.6	0.8	8.50	6.35	33.8	2.15
	62.2	3.3	8.09	5.67	42.6	2.42
	113.6	2.3	12.54	9.04	38.7	3.50
	154.8	17.1	22.57	19.45	16.0	3.12
	194.1	55.6	22.40	20.44	9.6	1.96
40.6	-16.1	10.2	19.55	21.84	10.5	2.28
	7.1	2.2	11.39	9.61	18.4	1.77
	39.6	3.0	9.03	6.59	37.1	2.45
	86.4	1.2	12.46	7.56	64.9	4.90
	126.6	6.1	21.25	17.45	21.7	3.80

Table 5.1: Data from the static tension tether experiments conducted on three slopes ranging from 30.0°-40.6°

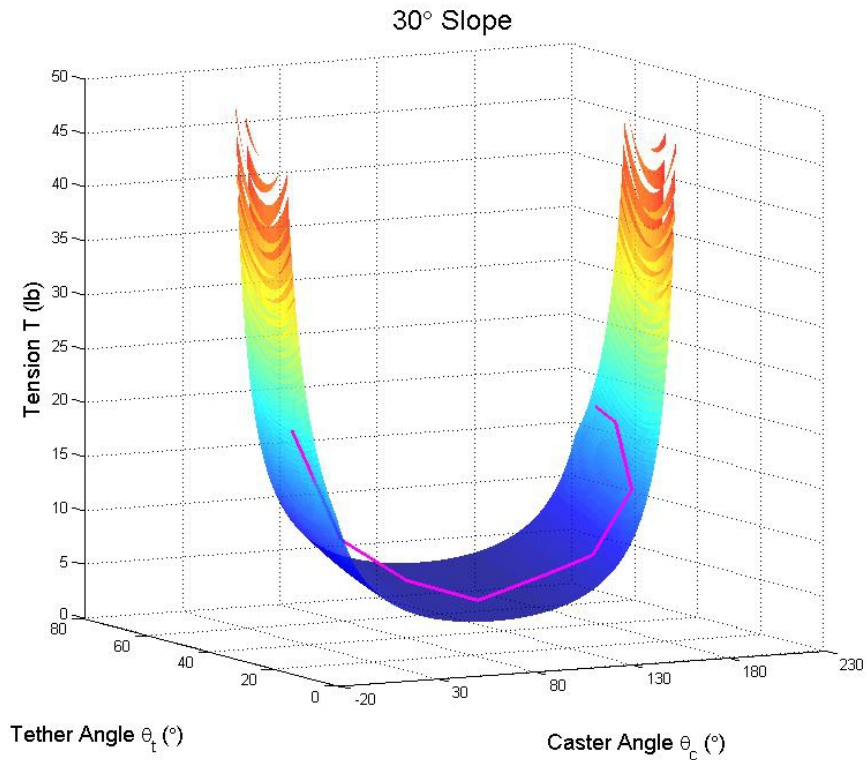


Figure 5.3: Measured tension, represented by the purple line, overlaid on the theoretical prediction for a 30° incline

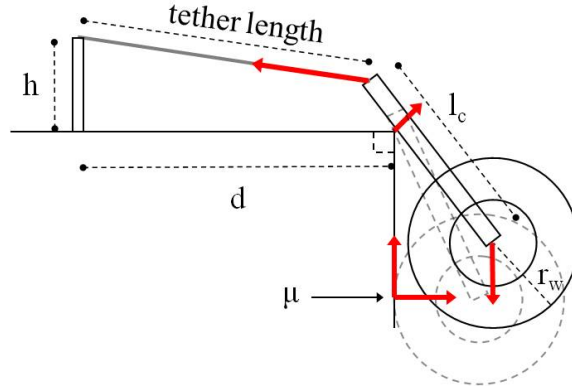


Figure 5.4: Free body diagram of *Axel* ascending over a ledge. Initially the wheels are in contact with the wall, but they may separate as winching progresses.

(see Section 2.3.3), the forces remain safely below the 500 lb loading capacity of the tether.

5.2 Climbing Precipices

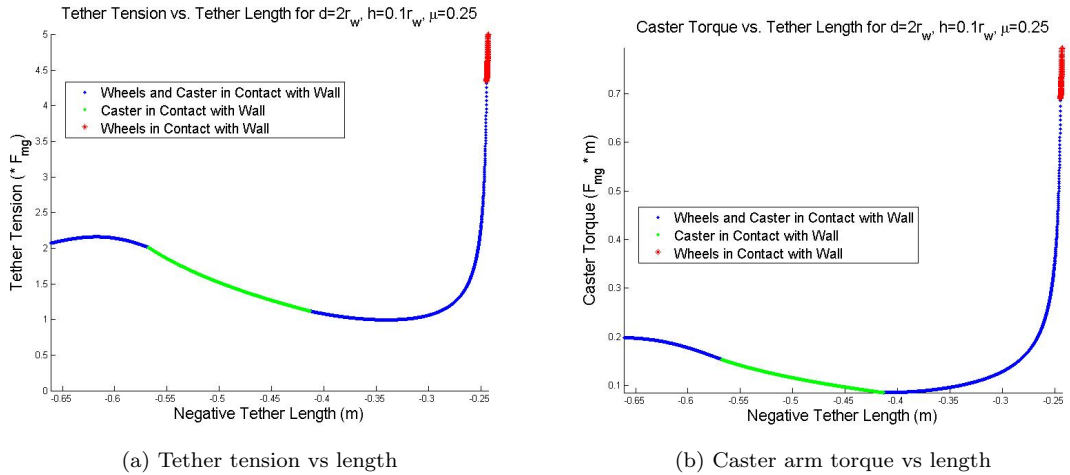
Precipices, or steep overhangs, occur naturally in many of the terrains that *Axel* is designed to explore, such as craters, canyons, and fissures (Figure 1.4). Experience during testing, however, has shown that this type of feature is particularly challenging for the *Axel* rover to surmount from below. While attempting to ascend a precipice, tether tension rises significantly and the caster motor may stall due to an increased demand in motor torque. This section develops a quasi-static model of this maneuver in order to gain insight into the forces involved and develop designs which will allow future *Axel* prototypes to easily climb these terrain features in the field².

A two-dimensional free body diagram of *Axel* climbing over a 90° ledge can be seen in Figure 5.4. The important parameters for this model are the wheel radius, r_w , the caster arm length, l_c , the coefficient of friction between the wheel and the wall, μ , and the anchor point's height and distance from the ledge, h and d , respectively. For this analysis, two assumptions are made: 1) a frictionless interface between the caster arm and the ledge corner, and 2) the center of mass of the rover is located at the center of the wheels (valid for low-mass caster arms).

If the ratio of wheel radius to caster length is sufficiently small and the anchor point is low, *Axel* will reach a configuration where its wheels lose contact with the wall. Figure 5.5a plots the estimated tether tension and Figure 5.5b plots the caster motor torque as the rover ascends over the lip. The simulation uses the parameters from *Axel 1* for the wheel radius (r_w) and caster length (l_c), 13" and 29.5" respectively. Note that the x-axis represents the negative of the unreeled tether length, corresponding to *Axel*'s ascent over the ledge in time from left to right.

In the early stage of the ascent, the required tension to support *Axel* on the precipice hovers

²This section describes work done in conjunction with Albert Wu.



(a) Tether tension vs length

(b) Caster arm torque vs length

Figure 5.5: Tether tension and caster arm torque vs the negative of the unreeled tether length. As the tether is reeled in, the plots can be interpreted as forward in time from left to right.

at around twice the weight of the rover. The theoretical tension then peaks rapidly as the wheels move closer to the corner of the ledge, reaching up to five times the rover’s weight (Figure 5.5a). The torque on the caster arm motor follows a similar curve as it becomes difficult to rotate the arm under high tether tension (Figure 5.5b). As *Axel* reaches the ledge with a low anchor point, the rover must pull very hard on the tether to generate any upward force since the tension vector is nearly horizontal. Once *Axel*’s wheels surpass the corner of the ledge, the rover’s weight will be supported by the precipice and the tension force will begin to decrease. Therefore, the end of the simulation represents the worst case tether tension while climbing over a ledge.

The potentially hazardous spike in tension can be mitigated by increasing the height of the anchor point. In doing so, the wheels will remain in contact with the wall and can help drive the rover over the ledge. From Figure 5.6, one can see that by increasing h , the tether tension can be minimized and kept below the rupture stress.

In practice, however, raising the anchor point height can be difficult to accomplish. The safety and reliability of the anchor point diminish as it approaches the precipice. Collapsible terrain on the edge of the cliff may give way under the load of a heavy rover, and slippery terrain may not provide a secure purchase, allowing the anchor to be pulled over the ledge. For added safety, *Axel*’s anchor point will likely be secured several, if not dozens, of meters from the edge of the cliff.

With a low anchor point, climbing over a sharp precipice is very taxing on the tether, however the force can be mitigated by actively driving *Axel*’s wheels. The grouser wheels, in particular, are very adept at securing a purchase in cracks and protrusions on vertical terrain, allowing the rover to leverage the wheel torque and therefore reduce tether tension in driving over 90° corners.

Based on the analysis presented in this section, a very lightweight composite fiber tether with 1 g/m linear density was selected for *Axel* experiments at JPL. Even with such a low mass, the tether

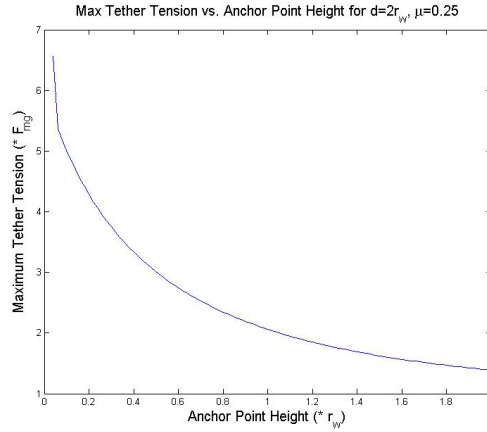


Figure 5.6: Maximum tether tension experienced while climbing over a ledge vs anchor point height for the geometry of Figure 5.4

could support up to ten times the rover’s weight, which would withstand unexpected dynamic loading during testing on steep slopes (see Section 2.3.3).

5.3 Tension in the Field

During a recent field experiment in Arizona, tether tension was measured while driving the second generation *Axel* rover (see Chapter 6) over rough natural terrain. The experiment showed, for the first time, the tether forces *Axel* experiences while outside of laboratory conditions.

The 250 lb capacity LC101 tension sensor (same as that used for experiments in Section 5.1) was mounted in line with the tether to record tension data as *Axel* rappelled over the rugged terrain. Figure 5.7a shows a time-lapsed sequence of images during the rover’s descent over the terrain, and Figure 5.7b portrays the tension data recorded during that same descent³.

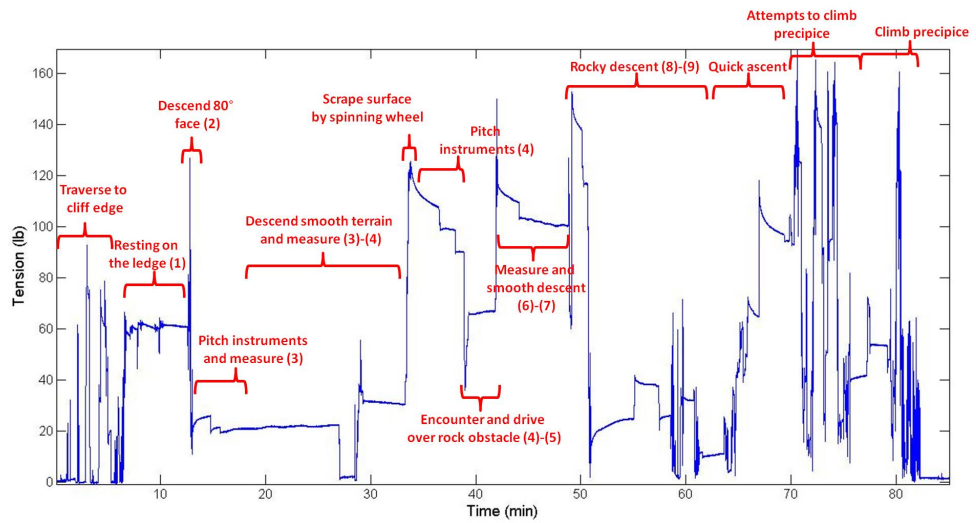
The tension data show that the ~ 100 lb rover exerts a maximum of 150 lb of force on the tether during descent, well within the tether’s 1,000 lb tolerance. Sharp peaks in the data result from short dynamic loads, correlating with rocky and uneven sections of the terrain. *Axel* also performed a maneuver in which it spun one wheel while hanging to scrape dirt from the terrain, exposing a new layer of rock and allowing instruments to take measurements a few mm below the surface. This maneuver did not overly strain the tether.

At the top of the cliff there was a fairly steep face at approximately a right angle with the top of the ledge. The rover made three attempts to ascend this precipice and failed, during which time the tether tension reached its peak value of ~ 170 lb. This value however, still maintained a 5x safety factor on the tether capacity. Overcoming the rim proved to be a challenge, but by maneuvering the rover, the teleoperator was able to secure a purchase with the wheels and travel

³Tension data was collected by Robert Peters.



(a) Time-lapse images



(b) Tension data

Figure 5.7: Time-lapsed images of *Axel 2*'s descent down the terrain of Figure 6.9a along with the tether tension data. Numbers in parentheses in the tension plot correspond to images in the time-lapse sequence.

over the sharp corner on the fourth attempt. Agreeing with the conclusion of the analysis in Section 5.2, the grouser wheels played a pivotal role in ascending the precipice.

Chapter 6

Axel 2 and *DuAxel*

This chapter details the development of the second generation *Axel* prototype, or *Axel 2* for short. Many improvements were made over *Axel 1* in terms of design, control, and robustness. The shortcomings of the *Axel 1* rover are presented and followed by an outline of how these shortcomings were addressed with the design of *Axel 2*. The next section introduces the *Dual-Axel*, or *DuAxel*, concept, which consists of two *Axel 2* rovers docked together through a central module. Finally, *Axel 2* and *DuAxel* performance is evaluated during recent extreme terrain field experiments.

6.1 *Axel 1* Shortcomings

The *Axel 1* prototype was adapted from the hardware of an old rover concept which was designed for neither tether winching nor extreme terrain traversal (see Section 2.3). Modifying the existing rover eliminated the time and cost associated with building a new robot for proof-of-concept tests, but the fundamental design of the original hardware had a number of shortcomings which needed to be addressed.

First, because science instruments were to be mounted inside the central module of the original *Axel* design as in Figure 2.2a [50], the rover did not provide a convenient location for contact instruments. Mounting the instruments inside *Axel's* cylindrical body would place them too far from the ground for in situ measurements, and deployment arms would occupy a large volume. The body could be lowered to the ground by decreasing the wheel radii, but this greatly reduces mobility and exposes the rover to an unacceptable risk of high-centering and collision with rocks and terrain protrusions.

Second, since only one actuator is used to both manage the tether and control the body pitch, *Axel 1* cannot independently orient its instruments when the wheels lose traction. For example, when the rover is on a 90° slope (free-hanging), actuating the caster arm will both rotate the central body and raise/lower *Axel* relative to the slope. In this situation, *Axel 1's* cameras cannot be independently controlled to focus on areas of interest.

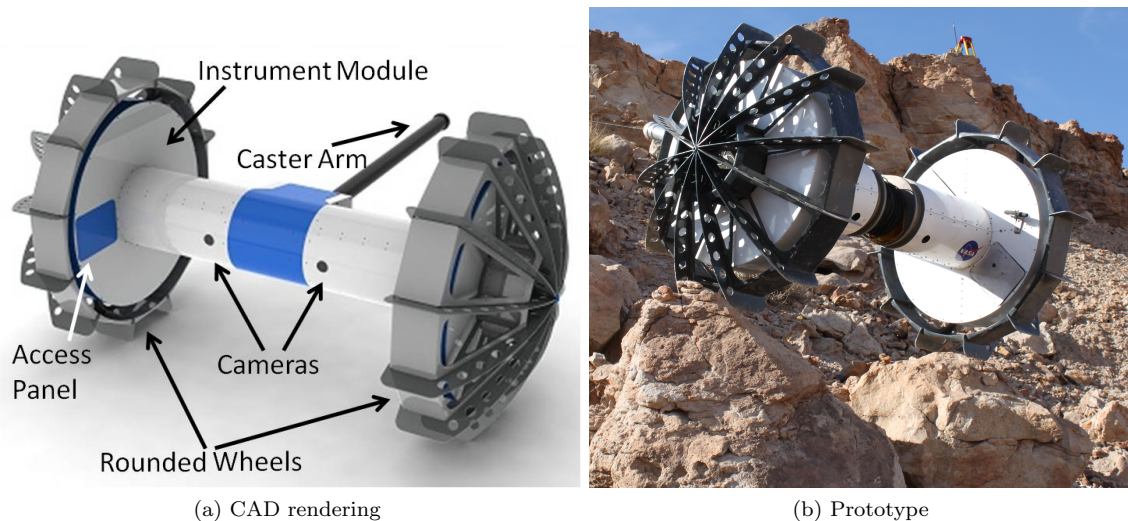


Figure 6.1: *Axel 2* CAD rendering and prototype traversing a rock during a field test

Third, *Axel 1* has no mechanism to actively manage tether tension or tether payout. If the tether is paid out at low tension, slack tether will accumulate between *Axel's* body and the caster arm. Conversely, reeling at very high tension will cause the tether to “knife” through lower layers of wound tether, which can result in tether damage and complicate unreeling. Similar issues were faced in the testing phase of *Dante II's* tethering system [40]. Furthermore, there is no mechanism in place to align the tether as it reels around the body.

While these shortcomings were the result of adapting an older rover concept for extreme terrain, there are also several hardware-specific limitations that were not addressed in *Axel 1* and deferred until the next generation.

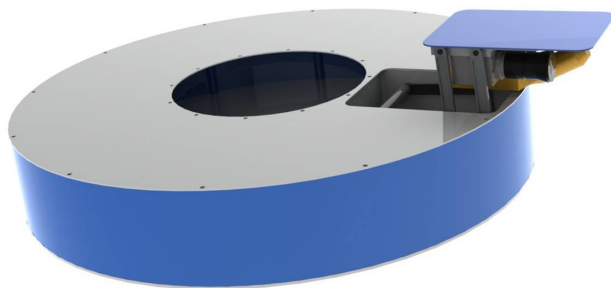
Axel 1's battery had a short lifespan and communication was limited over long distances. The grouser wheels were designed and built on a very low budget and hence leveraged existing fabricated parts. As such, they did not have curved wheels to handle tip-overs on the side. While they were adept at traversing over obstacles, if *Axel* were to tip-over onto its side it could conceivably reach a configuration from which it could not recover.

Extensive testing in the Mars Yard also revealed a number of other practical limitations, such as susceptibility to overheating and clogging of the wheel bearings with sand.

6.2 Second-Generation *Axel* Prototype

Figure 6.1a shows a computer rendering of the second-generation *Axel*, while Figure 6.1b shows a photograph of an *Axel 2* prototype. As summarized below, significant changes were made to the *Axel 1* design in order to make this a more viable candidate for future space exploration missions¹.

¹The material presented in this section is largely the work of Jaret Matthews, chief designer of *Axel 2*.



(a) CAD rendering of unmounted instrument module



(b) Taking measurements

Figure 6.2: Instrument module which is housed inside of the wheel structure. Motorized access panel extends to take measurements and then retracts to protect from dust, debris, and contaminants.

The outboard surfaces of the wheels are curved so that *Axel 2* can roll back to its nominal stance in the case of a tip-over onto its side. At the same time, *Axel 2* retains the grouser wheel features, which proved very useful going over obstacles in the *Axel 1* design. The holes in the grousers reduce wheel mass without compromising the overall strength of the wheel's structure.

The space within the volume of the wheel structure houses scientific instruments and sampling devices. Inside this enclosure and beneath the wheels, the instruments are protected from rocks, protrusions, dust, and falling debris. This design also simplifies thermal control, as the thermal management system can be readily extended into these science bays. Opening a motorized access panel allows an infrared spectrometer to extend out of the wheel structure so that it can be placed within centimeters of a test site (Figure 6.2). Thus, *Axel 2* can take multiple measurements on any slope—even at 90 degrees. Samples can be evaluated in situ and only the most interesting specimens need to be returned to the host rover. Different instruments can be incorporated within the science bays depending on the specific mission objectives.

In addition to its strength fibers, *Axel 2*'s tether also houses electrical wiring to provide both power and communication to the rappelling rover. This allows the on-board battery to be recharged from a remotely located power source (solar or nuclear) on the host rover or platform. Assuming that the host rover has solar panels and is anchored in a location with access to sunlight (or is powered by nuclear means), *Axel 2* can operate indefinitely in the dark recesses of planetary craters. Furthermore, doubly or triply redundant embedded communication lines in the tether ensure that the rover's operators will never lose contact with *Axel 2*. Greater bandwidth through the tether, even over long distances, allows the rover to stream large amounts of data.

In order to better manage tether winding around *Axel*'s body, a powered fairlead was incorporated into the design. In conjunction with a tension sensor, the fairlead maintains a constant tension on the tether as it reels and unreels. By doing so, *Axel 2* avoids slack tether buildup during unreeling

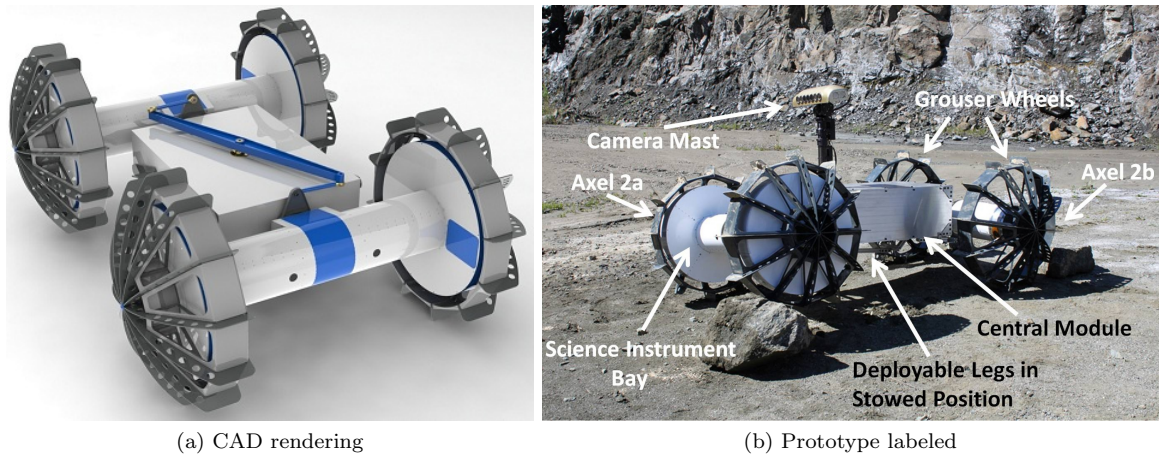


Figure 6.3: *DuAxel* is formed by docking two *Axel* rovers together through a central module.

and prevents knifing, which was discussed in Section 6.1. The enclosure over the cable drum protects the tether from dust and debris, and it also insulates the cable's heat from the cold environment. Finally, an additional motor has been introduced to control tether reeling. This de-couples the caster arm's movements from the tether, which has two main benefits. The first is that *Axel*'s cameras, which rotate with the body, can now be controlled independent of the rover's position on the slope. The second benefit is that the caster arm can be used more effectively as a tool to manipulate the tether should it happen to become ensnared around an obstacle.

Axel 2 also incorporates practical mechanical improvements, such as sealed bearings to keep out dust and a central ventilation shaft to prevent overheating during Earth-based experiments. Motor torque capacity was increased from the first-generation *Axel* in order to improve rappelling performance. Finally, *Axel 2* was designed to survive a .5 m drop, and all components and materials used in the rover were upgraded to comply with JPL safety standards.

6.3 The *DuAxel* Architecture

Short for Dual-Axel, *DuAxel* describes a four-wheeled vehicle formed by connecting two *Axel* rovers through a central module (Figure 6.3). While the tethered *Axel* was initially conceptualized as a daughter-ship for extreme terrain, the *DuAxel* architecture provides all the capabilities of a mobile mother-daughter system (see Section 2.1.1).

DuAxel is an extremely versatile rover. In the four-wheeled configuration with both *Axels* docked to the central module, *DuAxel* adeptly traverses gentle terrains. A mast mounted on the central module can house cameras used for obstacle detection and motion planning. Solar panels affixed to the top of the module can provide energy for the two docked *Axels*. Additionally, the module can also increase the scientific capacity of the mission by carrying more sophisticated instruments.

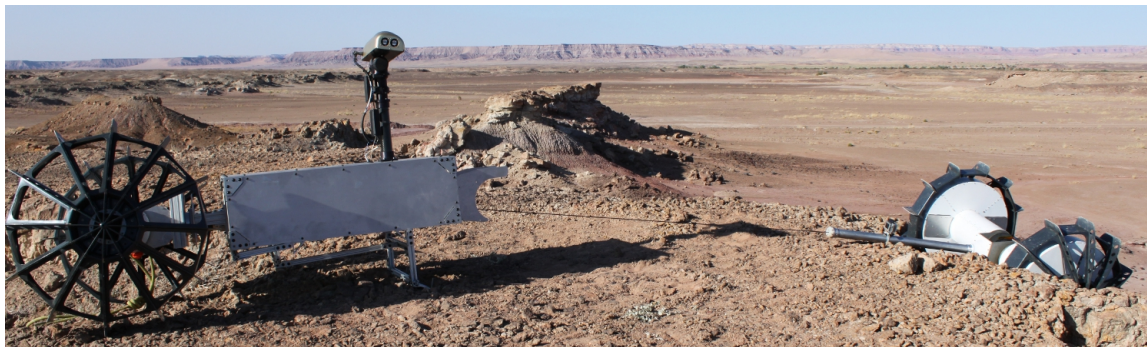


Figure 6.4: *DuAxel* in rappelling mode where the central module deploys legs to serve as an anchor while one of the *Axels* rappels into low-ground

By undocking one *Axel* and deploying legs, *DuAxel* reaches another versatile configuration. In this mode, the central module and one *Axel* form the mother ship and physical anchor, allowing the second *Axel* to rappel into low-ground (Figure 6.4). The central module provides power and communication to the descending *Axel* while at the same time using the high-ground to identify obstacles and help plan the descent path. With its deployable legs, *DuAxel*'s central module provides a reliable anchoring mechanism that is both simple and easy to de-anchor, allowing *DuAxel* to take many measurements over numerous descents.

In the third and final configuration, the central module is deposited by the *Axels* and serves as a fixed mother-ship while the *Axel 2* robots explore the surrounding area. By coordinating tasks between the two rovers, *DuAxel* can quickly and efficiently study a particular location of interest, making full use of the central module's sophisticated scientific instruments.

Because of its simplicity and low-cost, multiple *DuAxels* could be deployed from the same lander. Operating in parallel, the team of *DuAxels* would cover a large area quickly. Furthermore, if one of the *DuAxels* experienced a critical failure, mission objectives could be fulfilled by the remaining rovers.

The central module will provide many benefits for a team of twin *Axel* rovers. The most important advantage however, is that the module transforms *Axel* from a host-dependent daughter rover into a fully independent mission architecture. *Axel* no longer needs to "piggy-back" on the mission of a larger rover, such as the MSL, opening up a wide array of possible mission scenarios and allowing JPL to target many more diverse scientific targets.

6.4 Extreme Terrain Field Tests

A number of experiments were conducted to test *Axel*'s and *DuAxel*'s performance during a variety of maneuvers. The first tests took place in the JPL Mini Mars Yard, where *DuAxel* practiced dozens of docking and undocking operations. After fine tuning the docking and leg deployment

mechanisms, *Axel* demonstrated a reliable and highly repeatable docking procedure. The tether actually simplified the process by naturally guiding the caster arm into the central module as *Axel* spun its spool and reeled the tether.

More challenging tests were conducted at the JPL Mars Yard, which contains larger rocks and sloped terrains. Both *Axel* and *DuAxel* demonstrated their mobility capabilities over flat and rocky surfaces, and *Axel* rappelled successfully on the sloped regions of the yard.

Another important test was carried out at the JPL Mars Yard to verify the robustness of the *Axel* design with respect to flip-over. The tethered *Axel* rover was driven up a section of terrain where a shallow grade ran parallel to a steep grade incline. As *Axel* ascended the terrain, straddling the two slopes, one wheel began to rise higher than the other. The ascent continued until the left wheel flipped over the right wheel and landed on the ground, leaving *Axel* in an upside-down configuration. The rover survived the impact without any damage and descended back down under its own power.

After concluding preliminary tests at JPL, it was time to push the limits of the new *Axel* hardware in the rugged terrains for which it was designed. Two off-site locations were chosen based on their proximity to JPL and similarity to targets of interest (see Section 1.2): the first was a man-made quarry in Canyon Country, California, and the second was the desert near Flagstaff, Arizona, which serves as a Mars analogue site for many JPL rover tests.

6.4.1 Vulcan Quarry

Vulcan Materials, a mining company which specializes in aggregates such as crushed stone and sand, granted *Axel* permission to operate in one of their quarries located in Canyon Country, California. The field tests conducted at this site demonstrated, for the first time, the end-to-end functionality of the *Axel* rover system. The tests included *DuAxel* traversing over relatively flat terrain, climbing over scattered rocks, driving to the edge of a cliff, undocking *Axel* from *DuAxel*, deploying *Axel* over extreme terrain, and driving *Axel* back up the cliff to re-dock.

Axel completed two full teleoperated runs on the 20 meter long slope shown in Figure 6.5a. The slope angle of the cliff varied from 65° to purely vertical along a cliff wall that was 18 m tall. The surface consisted of hard rock, soft soil, and large amounts of rocky debris. In both runs, *Axel* successfully separated from *DuAxel*, descended the steep slope, traversed the flat terrain at the bottom, and returned up the escarpment to re-dock with *DuAxel*. *Axel* covered a total round trip distance of 100 m and 50 m during the first and second runs, respectively. Figure 6.5b shows still shots from the rover's second descent of the cliff face.

While *Axel* rappelled down the cliff, the central module remained anchored using a passively deployed leg mechanism (Figure 6.4). Two 18 inch drill bits were partially inserted into the ground using a manual percussive drill through the anchor plate holes shown in Figure 6.6 to further secure the anchor plate. These drill bits were used as a precaution since it was unknown if the rappelling

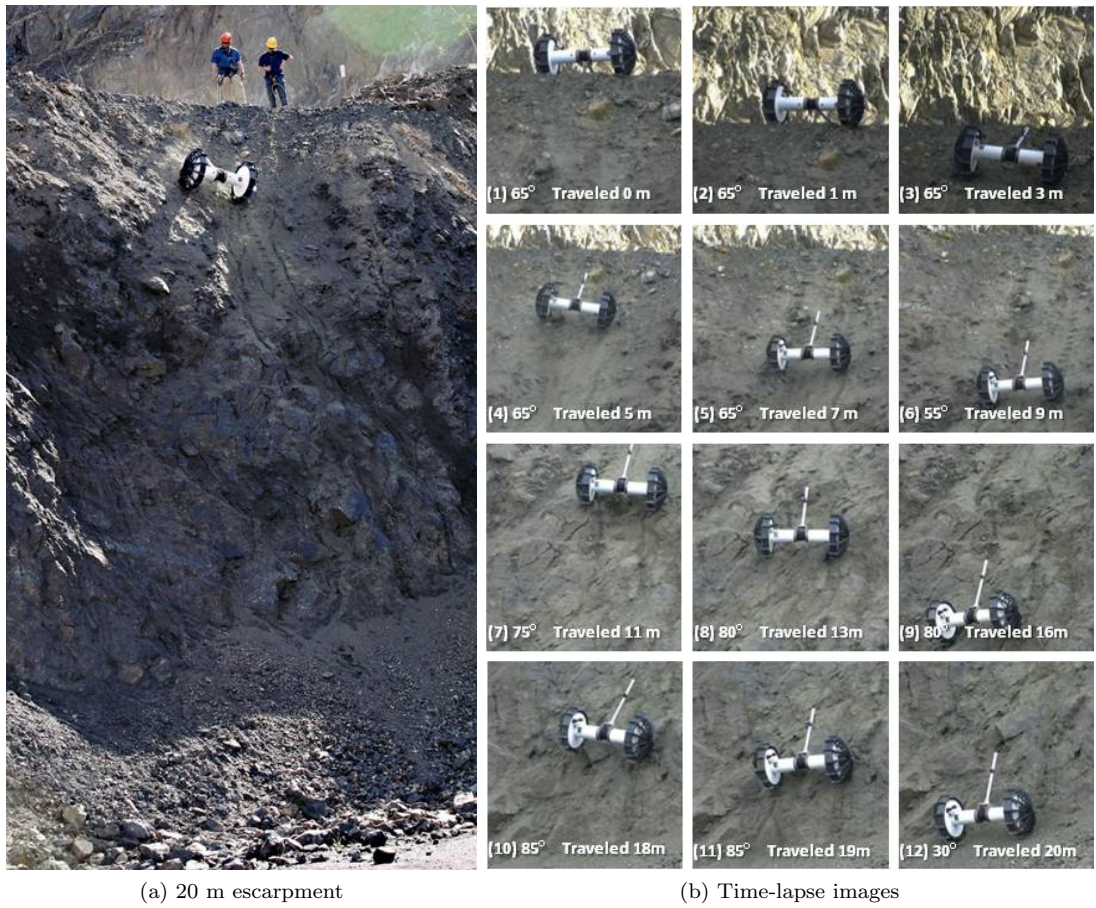


Figure 6.5: *Axel 2* descending a 20 m escarpment with slopes ranging from 65° to 85° at the Vulcan quarry in Canyon Country, California

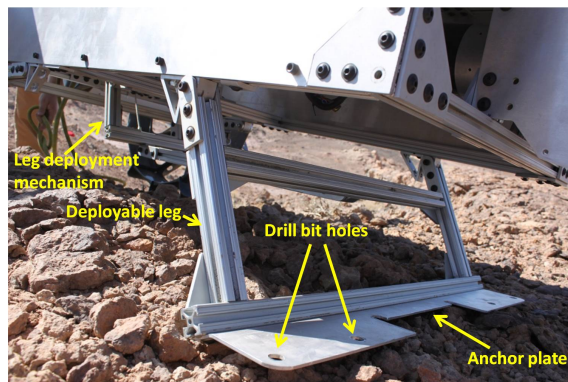


Figure 6.6: *Axel 2* separates from *DuAxel*, releasing a spring-loaded mechanism which deploys legs to support the central module.

Axel would pull the central module over the cliff edge. A third experiment, which relied solely on the passively deployed legs (i.e., without drill bits securing it to the ground), demonstrated no sliding of the central module while *Axel* descended into low-ground. Deploying the central module on a slight upslope tilt of a few degrees, the tether tension actually pulled the anchor point further into the ground, making it more secure. Re-docking *Axel* to the central module activated a spring-loaded mechanism which released the anchor plate. These experiments demonstrated that a passively deployed anchor could potentially support rappelling scenarios over terrains composed of a mixture between soil and rocks. Further studies would still be necessary to assess the advantages/disadvantages of an active anchor deployment vs a passive one.

With its top speed of 10 cm/s, *Axel* ascended the 20 meter slope in approximately four minutes. During some portions of the traverse, a large quantity of rocky debris cascaded onto *Axel* without causing damage to the rover. By controlling the body pitch as it ascended the cliff, the rover effectively protected its cameras from the falling debris.

The Vulcan quarry testing once again demonstrated *Axel*'s ability to navigate extreme terrain and its resiliency in the face of adverse conditions. The next tests in Arizona would focus more on long *DuAxel* traverses and collecting data with the rover's on-board scientific instruments.

6.4.2 Arizona Desert

Following on the heels of the Vulcan quarry tests, *Axel* was transported to the desert in northern Arizona near Black Point Lava Flow. The site closely resembles rugged Martian terrain and is frequently used by JPL to test technologies relating to future rover missions. Two full days were allotted for the tests, allowing extensive experimentation with the *Axel 2* and *DuAxel* hardware.

While the scenarios were largely identical to those tested at the quarry, *Axel* was equipped with a few upgrades to prepare for these experiments. First, three instruments were installed in one of the science modules, including an Ocean Optics USB2000 reflectance spectrometer collocated



Figure 6.7: *DuAxel* at a Mars analogue site in Arizona climbing up a terrain with slope angles up to 35°



Figure 6.8: *Axel 2* successfully descended a 15 m slope with inclines between 25° and 45° on the first day of testing in Arizona.

with a microscopic imager. Both were focused on a point 5 cm beyond the instrument deployment mechanism. The third instrument, a contact thermal probe, was mounted on a separate deployment panel in the science bay. As an additional upgrade, a roll joint, connecting one of the *Axels* to the central module, enabled the *DuAxel* to traverse more rugged terrain. Only one leg deployment mechanism was built, and hence only one *Axel* could be undocked during the experiments.

On the first day of testing, *DuAxel* was driven along a 130 m route to the top of a cliff that revealed layered stratigraphy. The path was filled with a mix of both friable and hard rocks ranging from a few centimeters to two meters in size (Figure 6.7). *DuAxel* successfully traversed the rocky terrain and climbed slopes up to 35° . Following the long upslope climb, *Axel* separated from *DuAxel* and rappelled down the steep terrain. The descent slope was 15 m in length and ranged between 25° and 45° . Certain portions of the terrain featuring stratigraphic layers had slope angles between 55° and 75° (Figure 6.8).

Throughout the run, the rover collected measurements with all three instruments at approximately 1 m intervals. At each stop, the rover would reorient its science bays in a turret-like fashion

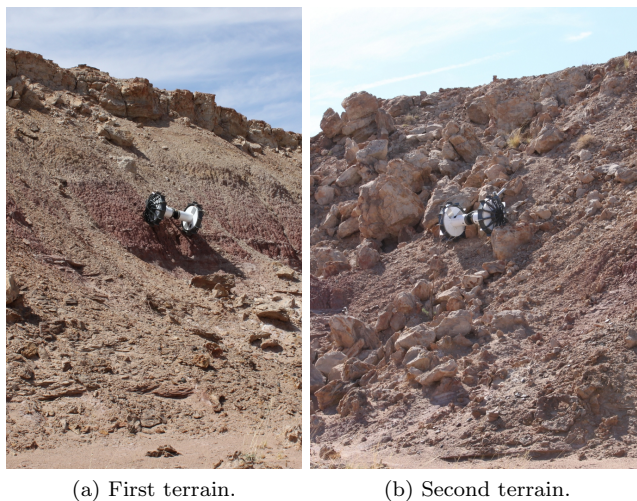


Figure 6.9: *Axel 2* descended two different terrain types on the second day of testing in Arizona. The first terrain was steeper with few rocks. The second terrain had an easier grade but was populated with many rocks.

to position different instruments on the site of interest. During this maneuver, there was no visible slip of the rover despite the fact that all four actuators were being operated simultaneously to re-orient the body. The precision of instrument pointing, on the order of millimeters, was significantly less than the 1 cm required by geologists wishing to study the region.

Following an 18 m traverse down this slope and another for the return trip, *Axel* re-docked with the central module and the *DuAxel* rover drove to a new location. The total distance traveled during this test was approximately 175 meters.

On the second day of testing in Arizona, two similar excursions were conducted on two different slopes: one was a steep slope with relatively few rocks (Figure 6.9a), and the second had an easier grade but contained many large scattered rocks (Figure 6.9b). The results from traversing the first terrain are discussed in Section 5.3.

The purpose of the experiment driving over the second terrain was to determine whether *Axel* could manage a situation in which its tether wrapped around or wedged underneath rocks (i.e., intermediate anchor points, see Section 4.5.3) on the terrain. The incline on this hillside ranged from 30° at the bottom to 40° near the top.

Using teleoperation, the rover successfully navigated across the entire length of the terrain, collected measurements, and ascended to the top. This terrain proved particularly challenging for the tethered rover as its supporting cable would frequently snag on rocks during the descent. At the bottom of the traverse, a power supply connected to the tether was used to remotely charge *Axel* from the top of the decline. The integrity of the conductors was not compromised by the bends around the rocks, and power was successfully transmitted to the rappelling rover.

By properly controlling the traverse path, the rover ascended successfully, freeing the tether as it



Figure 6.10: *Axel 2*'s tether becomes snagged easily in the field on rocky terrain. The tether is highlighted for clarity. The rover ascended successfully during this test under teleoperation. Future work should use the algorithm developed in Section 4.5 to navigate autonomously in these scenarios and return to the anchor point.

went along. Similar to previous field tests and following the explanation of Section 4.5.2, the ascent proved more challenging than the descent as the rover had to follow a specific path to release the wedged tether (Figure 6.10). The return path included traversing over rocks that exceeded a wheel diameter as shown in Figure 6.1b.

Axel's tether-less mobility was also tested on two different sloped terrains. One slope consisted of normal soil while the other was covered with flagstones. Tests conducted on 10° and 20° inclines were successful, however a solo *Axel* could not ascend 30° slopes on either of the two terrain types. Under similar test conditions on terrain composed of soil, *DuAxel* was able to climb slopes of 35° . Experiments assessing the upper limit of *DuAxel*'s mobility have not yet been performed.

In summary, over two days of testing in the Arizona desert, *Axel* was subjected to approximately half a dozen major traverses over various terrain types, and a large volume of data was collected from both *Axel*'s own instruments and the tether tension sensor. These experiments showcase *Axel 2*'s ability to navigate challenging terrain and demonstrated end-to-end operational scenarios of the



Figure 6.11: Picture of the Riegl 3D laser scanner used to scan terrain in Arizona

Axel rovers: traversing to a cliff edge, undocking, rappelling, measuring, ascending, and re-docking. Together, *Axel* and *DuAxel* traveled a combined distance of half a kilometer over rugged Martian-like terrain.

6.4.3 3D Terrain Scanning

A Riegl 3D laser scanner was transported to Arizona in order to map and model the terrains that the rovers traversed. This section provides details on the experimental tools and procedure and provides preliminary results.

Figure 6.11 shows a picture of the Riegl 3D laser scanner that was taken to Arizona. While perched on a tripod, the scanner takes measurements by shining laser light over the terrain and detecting both the distance to the target and the amplitude of the light reflecting from its surface. It can rotate a full 360° horizontally and has a vertical scanning range of up to 80° . The scanner is powered by a 13 V power supply and uses serial and parallel communication cables to interface with a laptop computer.

In Arizona, the laser scanner was used to generate three-dimensional terrain plots of the various slopes used in the *Axel* and *DuAxel* experiments. For example, the terrain traversed by *DuAxel* in Figure 6.7 is shown as an interpolated contour map in Figure 6.12. In the four-wheeled configuration, *DuAxel* navigated the gentler slope shown in the plot and climbed up the back of the terrain to the top of the hill. After undocking, *Axel* rappelled down the steep part of the slope shown both in the contour plot and in Figure 6.8.

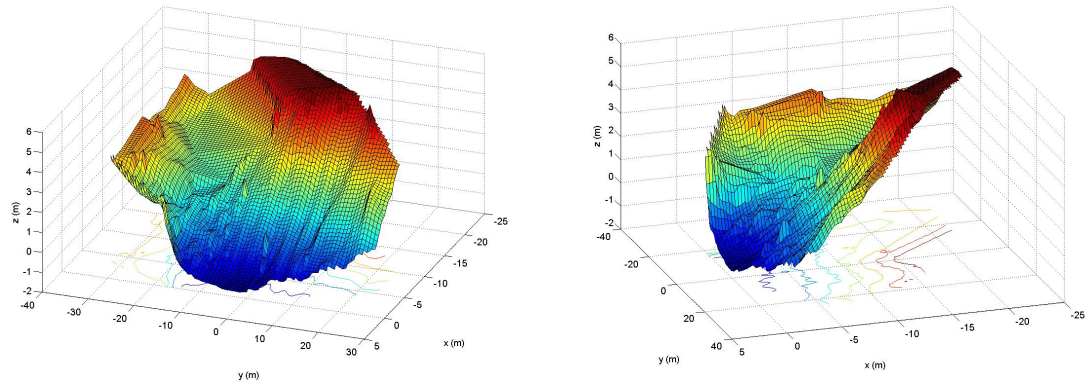


Figure 6.12: Two perspectives of the interpolated contour map of the terrain taken by the 3D laser scanner. *DuAxel* navigated the rocky terrain on the side (Figure 6.7) to climb to the top of the hill and support *Axel* as it rappelled down the steep slope (Figure 6.8).

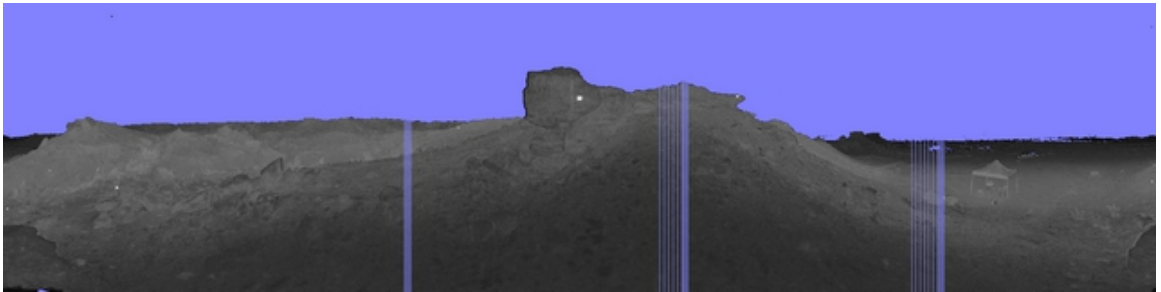


Figure 6.13: Two dimensional panorama image of the terrain traversed during the first day of testing in Arizona using reflected amplitude measurements for brightness. Reflectors appear as bright white spots and the tent in the bottom right corner indicates where *DuAxel* began its traverse.

The laser scanner also has the ability to correlate multiple scans into a single terrain map. By positioning reflectors throughout the terrain and comparing the position of the reflectors across multiple scans, the Riegl can determine its location in absolute coordinates and merge several scans into one. Merging scans from strategic locations around the terrain can eliminate data “shadows” which occur behind rocks and protrusions, generating a complete and highly accurate model of the terrain. Figure 6.13 shows a two-dimensional panorama image of the terrain traversed during the first day of testing in Arizona using the amplitude measurements of the reflected laser beams. The reflectors can be seen as bright white spots on the terrain. Also, note the tent at the bottom right corner of the image, marking where *DuAxel* began its traverse at the bottom of the terrain.

In total, six complete scans were taken of the terrain from the first day of testing in Arizona, following the path of the *Axel* rovers and using reflectors to correlate individual scans with respect to each other. Additional single scans were conducted on each of the two terrains used during the second day of testing. In the future, terrain maps like these can be used to predict wheel traction, avoid high-abrasion and high-tension scenarios, and plan paths so that *Axel* can operate autonomously on

rugged terrain. In short, the processed data will supplement the already remarkable capabilities of the *Axel* and *DuAxel* rovers and greatly enhance their extreme terrain capabilities.

Chapter 7

Conclusion

This dissertation summarized work aimed at developing a new class of rover technology for extreme planetary terrain. The result of this effort, the *Axel* rover, demonstrated a robust ability to descend steep slopes and navigate rocky terrain. Its symmetrical design easily adapted into a winch system and the caster arm provided stability while rappelling. Furthermore, *Axel*'s ability to tumble eliminates a tip-over failure mode, which is what brought an earlier rappelling rover, *Dante II*, to its unfortunate demise.

Chapter 1 provided background and motivation for the work on *Axel*. Chapter 2 explored the trade-offs between different mission architectures for extreme terrain exploration, concluding that a mobile mother-daughter system would offer the largest number of benefits with the fewest number of drawbacks. The *Axel* concept was presented and Section 2.3 detailed early developments leading up to long traversal experiments in the JPL Mars Yard.

Chapter 3 outlined the investigation to optimize *Axel*'s wheels for extreme terrain. Prototype iterations converged on a grouser design capable of surmounting obstacles up to 90% of the wheel diameter. While these wheels were significantly less efficient on flat ground than traditional wheels, the remarkable advantage gained in rocky terrain mobility discouraged abandonment of the grouser concept.

Chapter 4 began by deriving the basic equations of motion which govern the evolution of *Axel*'s state over time. Holonomic and nonholonomic equations relating to tether tension and no-slip constraints were introduced. Finally, slip is modeled using the principles of the power dissipation method, and the resulting equations are applied to a model of the *Axel* rover. Section 4.5 introduced a novel motion planning algorithm for steep-terrain tethered excursions. The algorithm takes advantage of the sleeve construction to compute homotopy classes of ascent/descent paths. The principles of the algorithm were first demonstrated with a simple example and then used to compute a feasible ascent on a high-resolution map of a portion of the Moon's Shackleton crater.

Chapter 5 provided models to predict tether tension while positioned statically on sloped terrain and also while climbing a precipice. The analysis was then validated with experiments conducted in

the laboratory and, in the following chapter, during field tests.

The *DuAxel* rover concept, formed by docking two *Axels* together through a central module, is introduced in Chapter 6. After preliminary docking and mobility tests were performed at JPL, both *Axel* and *DuAxel* were rigorously tested in two separate field tests. The first test, conducted in the Vulcan quarry in Canyon Country, CA, demonstrated the first end-to-end functionality of the *Axel* rover system. The rover successfully rappelled down a 20 m long escarpment and survived collisions with falling rocks.

Axel was then transported to the Arizona desert for a second round of field experiments. The site, near Black Point Lava Flow, closely resembles Martian terrain and is frequently used as a test location for JPL Mars rover technology. *DuAxel* drove several hundred meters over rocky and sloped terrain with up to 35° inclines. Under teleoperation, *Axel* rappelled down both steep and rocky terrains, managing to ascend even when its tether became wrapped around obstacles. A tension sensor mounted in-line with the tether recorded stress forces during the traverse and *Axel* was successfully charged remotely from the anchor point.

7.1 Future Work

Together, *Axel 2* and *DuAxel* demonstrated a robust design that is closer to the goal of a flight-qualified robotic rover capable of exploring extreme terrains on extra-planetary bodies. Future work should focus on three important aspects of the system: central module design, tether management, and autonomous capabilities.

While the central module used in the Vulcan quarry and Arizona field tests proved successful, it was ultimately nothing more than a proof-of-concept prototype designed to demonstrate the feasibility of docking two *Axel* rovers. As a result, there is still a great deal of freedom in the module design that can be explored to further the capabilities of the *DuAxel* system. The Arizona desert experiments demonstrated that the addition of a roll joint in the docking mechanism on one side of the *DuAxel* greatly improved the system's performance in traversing rocky and sloped terrain. Future designs should incorporate both yaw and roll docking joints for each of the rovers, leading to increased turning ability and mobility on rugged terrain.

The current central module design features a large volume of empty space within the structure. Future iterations can take advantage of this space to house electronics and sophisticated scientific instruments. Solar panels can also be affixed to the top of the module, enabling self-charging and extended operation in rugged environments.

Finally, the passive leg-deployment mechanism, which supports the central module while one *Axel* undocks, uses a spring-loaded linkage design that occupies a significant volume. An actuated mechanism has the potential to be smaller, simpler, and more robust. And with batteries conve-

niently located inside the module to provide power, there will be few drawbacks to implementing a motor-driven leg system.

Another important area for future work will be tether management. The design blueprints for the *Axel 2* rover contained plans for both a powered fairlead (to maintain tether tension during reeling) and a reel guide (to evenly distribute the tether across the spool). Unfortunately, time and budget constraints did not allow for the manufacturing of these mechanisms. By precluding knifing, slack tether accumulation, and uneven tether distribution, these systems will greatly increase the robustness of the *Axel* rover, especially during hundred meter rappels.

While traversing extreme terrains, *Axel* must be capable of negotiating a wide range of slope angles where tether tension will play a key role in the rover's mobility. The approach used in all previous experiments was open-loop, i.e., the tether was unreeled at a constant rate while *Axel* maneuvered on the terrain. This approach could cause the tether to become either too loose or too tight, hindering the rover's mobility. Actively sensing the tether tension and adjusting the spool rate will improve *Axel's* efficiency and significantly increase its capabilities on extreme terrain.

Lastly, *Axel's* reliance on teleoperation is a weakness that needs to be addressed if the rover is to be considered flight-qualifiable. The algorithm presented in Chapter 4 lays the foundation for autonomous rappelling operation, and future work should focus on using *Axel's* on-board sensor suite to detect obstacles, compute intermediate anchor points, and plan paths within the sleeve of its descent. Simpler tasks, such as docking and *DuAxel* traversal, can also be automated, making the rover more independent, easier to operate, and more robust.

Extending the motion planning algorithm from simulation to experiment will be a key milestone for the *Axel* rover, and it will require modification of some of the algorithm's specific elements. In particular, modeling the terrain as a set of intersecting two-dimensional planes works well for computer analysis, but experiments will be needed to validate this approach. The rover dynamics and the terrain should also consider topographies with significant cross-slope to more closely approximate real terrains.

Furthermore, predicting the taut tether configuration was simplified by restricting the tether's motion to the plane and assuming frictionless interaction with the terrain. With these simplifications, the taut tether assumes the shape of the shortest homotopic path, which is simply the shortest path in the tether's given sleeve. Given a complex and intricate real-world terrain, however, these assumptions will likely have to be relaxed in order to implement an appropriate motion planning strategy. Autonomous planning in the field will likely have to incorporate a combination of sensors to detect nuances in the terrain and adjust to the tether configuration. For example, three-dimensional laser scanners (see Section 6.4.3) can be used to plan motion prior to rappelling down the slope. Along the way, sensors on the anchor platform and the descending rover can be used to estimate the tether configuration and adapt accordingly. Using a feedback loop in this manner will increase

the algorithm's robustness on real terrains and produce successful navigation when the simplifying assumptions do not hold.

Using these modifications, autonomous *Axel* experiments using the tethered motion planning algorithm can be tested on carefully controlled terrains, such as the artificial lunar crater described in Section 2.3.2. Once the algorithm has been fine-tuned, it can be subjected to increasingly difficult topographies, e.g., steep slopes in the JPL Mars Yard and cliffs in the Arizona desert.

Axel and *DuAxel* have demonstrated remarkable mobility on rugged terrain. Future work will serve to both reinforce and extend its capabilities. While the rover is designed for exploration of extra-planetary bodies, *Axel* also has many potential applications here on Earth, such as search and rescue, mining engineering, and military support. *Axel* is a simplistic and versatile concept, and by changing only a few design parameters the rover can be reconfigured for a variety of tasks. The analysis and experiments presented in this dissertation only scratch the surface of *Axel*'s potential, and future work will hopefully explore all these avenues of research.

Bibliography

- [1] http://www.nasa.gov/mission_pages/mer/.
- [2] <http://marsprogram.jpl.nasa.gov/msl/>.
- [3] http://www.nasa.gov/mission_pages/mars/images/pia09028.html.
- [4] http://www.nasa.gov/mission_pages/mars/images/pia09027.html.
- [5] http://www.nasa.gov/mission_pages/mer/images/pia10210.html.
- [6] <http://lunar.gsfc.nasa.gov/>.
- [7] <http://lunar.gsfc.nasa.gov/lola/>.
- [8] Communications with earth: How fast and how much data the rovers can send back. http://marsrovers.nasa.gov/mission/comm_data.html.
- [9] P. Abad-Manterola, J.W. Burdick, and I.A.D. Nesnas. Axel rover paddle wheel design, efficiency, and sinkage on deformable terrain. In *IEEE Conference on Robotics and Automation*, Anchorage, Alaska, May 2010.
- [10] P. Abad-Manterola, J.W. Burdick, I.A.D. Nesnas, and J. Cecava. Wheel design and tension analysis for the tethered axel rover on extreme terrain. In *IEEE Aerospace Conference*, Big Sky, Montana, March 2009.
- [11] P. Abad-Manterola, J.A. Edlund, J.W. Burdick, A. Wu, T. Oliver, I.A.D. Nesnas, and J. Cecava. Axel: A minimalist tethered rover for exploration of extreme planetary terrains. *IEEE Robotics and Automation Magazine*, 16(4):44–52, December 2009.
- [12] J.C. Alexander and J.H. Maddocks. On the kinematics of wheeled mobile robots. *International Journal of Robotics Research*, 8(5):15–27, October 1989.
- [13] M. Allison and R. Schmunk. Technical notes on mars solar time as adopted by the mars24 sunclock, August 2008. <http://www.giss.nasa.gov/tools/mars24/help/notes.html>.

- [14] D. Apostolopoulos and J. Bares. Locomotion configuration of a robust rappelling robot. *International Conference on Robotics and Automation*, 3:280–284, August 1995.
- [15] N. Atkinson. Mars methane gets even more mysterious. *Universe Today*, September 2010. <http://www.universetoday.com/74091/mars-methane-gets-even-more-mysterious/>.
- [16] S. Badal, S. Ravela, B. Draper, and A. Hanson. A practical obstacle detection and avoidance system. In *2nd IEEE Workshop on Application of Computer Vision*, 1994.
- [17] M. Badescu, X. Bao, Y. Bar-Cohen, Z. Chang, B.E. Dabiri, B. Kennedy, and S. Sherrit. Adapting the ultrasonic/sonic driller/corer for walking/climbing robotic applications. *Proceedings of the SPIE*, 5762:160–168, 2005.
- [18] J. Bares and D. Wettergreen. Dante II: Technical description, results, and lessons learned. *International Journal of Robotics Research*, 18(7):621–649, July 1999.
- [19] P. Bartlett, D. Wettergreen, and W.L. Whittaker. Design of the scarab rover for mobility and drilling in the lunar cold traps. In *International Symposium on Artificial Intelligence, Robotics and Automation in Space*, February 2008.
- [20] S. Baten, R. Mandelbaum, M. Luetzeler, P. Burt, and E. Dickmanns. Techniques for autonomous, off-road navigation. *IEEE Intelligent Systems Magazine*, pages 57–65, 1998.
- [21] M.G. Bekker. *Off-the-Road Locomotion*. Michigan University Press, 1960.
- [22] M. Braukus. Nasa missions uncover the moon’s buried treasures, October 2010. <http://lcross.arc.nasa.gov/observation.htm>.
- [23] R.D. Braun and R.M. Manning. Mars exploration entry, descent and landing challenges. *Journal of Spacecraft and Rockets*, 44(2):310–323, 2007.
- [24] A. Bresser. *CESAR: Crater Exploration and Sample Return*. Technical report, Universität Bremen, 2008. <http://cesar.dfki-bremen.de/blog1.php>.
- [25] A. Broggi, M. Bertozzi, A. Fascioli, C.G. LoBianco, and A. Piazzzi. Visual perception of obstacles and vehicles for platooning. *Transactions on Intelligent Transportation Systems*, 1(3), 2000.
- [26] B. Brogliato. *Nonsmooth Mechanics*. Springer, 1999.
- [27] B. Chazelle. A theorem on polygon cutting with applications. *23rd Annual Symposium on Foundations of Computer Science*, pages 339–349, 1982.
- [28] R.H. Cushman and J. Sniatycki. *Geometry of Nonholonomically Constrained Systems*. World Scientific, 2009.

- [29] M. de Berg, M. van Kreveld, M. Overmars, and O. Schwarzkopf. *Computational Geometry: Algorithms and Applications*. Springer-Verlag, 2008.
- [30] B. Fox, L.S. Jennings, and A.Y. Zomaya. *Constrained Dynamics Computations: Models and Case Studies*. World Scientific, 2000.
- [31] J. Hershberger and J. Snoeyink. Computing minimum length paths of a given homotopy class. *Computational Geometry*, 4:63–97, 1994.
- [32] S. Hert and V. Lumelsky. Moving multiple tethered robots between arbitrary configurations. *International Conference on Robots and Intelligent Systems*, 2:280–285, 1995.
- [33] S. Hert and V. Lumelsky. The ties that bind: Motion planning for multiple tethered robots. *Robotics and Autonomous Systems*, 17(3):187–215, May 1996.
- [34] S. Hert and V. Lumelsky. Planar curve routing for tethered-robot motion planning. *International Journal of Computational Geometry and Applications*, 8(4):437–466, August 1998.
- [35] S. Hert and V. Lumelsky. Motion planning in r^3 for multiple tethered robots. *IEEE Transactions on Robotics and Automation*, 15(4):623–639, August 1999.
- [36] A. Howard, I.A. Nesnas, B. Werger, and D. Helmick. A novel reconfigurable robotic exploratory vehicle for navigation on rough terrain. In *10th International Symposium on Robotics and Applications*, Seville, Spain, June 2004.
- [37] G. Ishigami, A. Miwa, K. Nagatani, and K. Yoshida. Terramechanics-based model for steering maneuver of planetary exploration rovers on loose soil. *Journal of Field Robotics*, 24(3):233–250, 2007.
- [38] R. Kirk, J. Kargel, P. Brandt, and M. Burton. Cassini mission briefing, December 2010. http://www.nasa.gov/mission_pages/cassini/telecon/20101214/.
- [39] E.R. Kraal, M. van Dijk, G. Postma, and M.G. Kleinhans. Martian stepped-delta formation by rapid water release. *Nature*, 451:973–976, February 2008.
- [40] M. Krishna, J. Bares, and E. Mutschler. Tethering system design for Dante II. In *IEEE Conference on Robotics and Automation*, Albuquerque, New Mexico, April 1997.
- [41] S. Lavalle. *Planning Algorithms*. Cambridge University Press, 2006.
- [42] R. Manduchi, A. Castano, A. Talukder, and L. Matthies. Obstacle detection and terrain classification for autonomous off-road navigation. *Autonomous Robots*, 18:81–102, 2005.
- [43] J.E. Marsden and T.S. Ratiu. *Introduction to Mechanics and Symmetry*. Springer-Verlag, New York, 1994.

- [44] S.L. Miller, J.L. Bell, J.E. Graf, and S.E. Matousek. Potential future Mars mission. In *AIAA Proceedings*, July 2000.
- [45] A. Mishkin. *Sojourner: An Insider's View of the Mars Pathfinder Mission*. Berkley Books, New York, 2003.
- [46] E. Mumm, S. Farritor, P. Pirjanian, C. Leger, and P. Schenker. Planetary cliff descent using cooperative robots. *Autonomous Robots*, 16(3):259–272, 2004.
- [47] T.D. Murphey and J.W. Burdick. A local controllability test for nonlinear multiple model systems. In *41st IEEE Conference on Decision and Control*, December 2002.
- [48] T.D. Murphey and J.W. Burdick. The power dissipation method and kinematic reducibility of multiple-model systems. *IEEE Transactions on Robotics*, 22(4), August 2006.
- [49] R.M. Murray, Z. Li, and S.S. Sastry. *A Mathematical Introduction to Robotic Manipulation*. CRC Press, 1994.
- [50] I.A.D. Nesnas. Reconfigurable exploratory robotic vehicles. In *NASA Tech Briefs*, Pasadena, California, July 2001.
- [51] I.A.D. Nesnas, P. Abad-Manterola, J.A. Edlund, and J.W. Burdick. Axel mobility platform for steep terrain excursions and sampling on planetary surfaces. In *IEEE Aerospace Conference*, Big Sky, Montana, March 2008.
- [52] H.B. Niemann, S.K. Atreya, S.J. Bauer, G. R. Carignan, J.E. Demick, R.L. Frost, D. Gautier, J.A. Haberman, D.N. Harpold, D.M. Hunten, G. Israel, J. I. Lunine, W. T. Kasprzak, T. C. Owen, M. Paulkovich, F. Raulin, E. Raaen, and S. H. Way. The abundances of constituents of Titan's atmosphere from the GCMS instrument on the Huygens probe. *Nature*, 438:779–784, December 2005.
- [53] J.P. Ostrowski. *The Mechanics and Control of Undulatory Robotic Locomotion*. PhD thesis, California Institute of Technology, 1996.
- [54] J.G. Papastavridis. *Analytical Mechanics: A Comprehensive Treatise on the Dynamics of Constrained Systems*. Oxford University Press, 2002.
- [55] P. Pirjanian, C. Leger, E. Mum, B. Kennedy, M. Garrett, H. Aghazarian, S. Fanitor, and P. Schenker. Distributed control for a modular, reconfigurable cliff robot. *IEEE Conference on Robotics and Automation*, 4:4083–4088, 2002.
- [56] F. Sciortino. An algorithm to find all paths between two nodes in a graph. *Journal of Computational Physics*, 87(1):231–236, 1990.

- [57] H. Shibly, K. Iagnemma, and S. Dubowsky. An equivalent soil mechanics formulation for rigid wheels in deformable terrain, with application to planetary exploration rovers. *Journal of Terramechanics*, 42:1–13, 2005.
- [58] S. Singh and P. Keller. Obstacle detection for high speed autonomous navigation. *International Conference on Robotics and Automation*, pages 2798–2805, 1991.
- [59] B. Steigerwald. Martian methane reveals the red planet is not a dead planet, January 2009. http://www.nasa.gov/mission_pages/mars/news/marsmethane.html.
- [60] S. Stoeter and N.P. Papanikolopoulos. Kinematic motion model for jumping scout robots. *IEEE Transactions on Robotics and Automation*, 22(2):398–403, April 2006.
- [61] J.R. Taylor. *Classical Mechanics*. University Science Books, 2005.
- [62] T. Watson. Troubles parallel ambitions in nasa mars project. *USA Today*, April 2008. http://www.usatoday.com/tech/science/space/2008-04-13-mars_N.htm.
- [63] D. Wettergreen and C. Thorpe. Developing planning and reactive control for a hexapod robot. *International Conference on Robotics and Automation*, pages 2718–2723, April 1996.
- [64] B. Wilcox and R. Jones. Muses-c nanorover mission and related technology. *IEEE Aerospace Conference Proceedings*, 7:287–295, March 2000.
- [65] B.H. Wilcox, T. Litwin, J. Biesiadecki, J. Matthews, M. Heverly, J. Morrison, J. Townsend, N. Ahmad, A. Sirota, and B. Cooper. Athlete: A cargo handling and manipulation robot for the moon. *Journal of Field Robotics*, 24(5):421–434, 2007.
- [66] T. Williamson and C. Thorpe. A specialized multibaseline stereo technique for obstacle detection. *IEEE Conference on Computer Vision and Pattern Recognition*, pages 238–244, 1998.
- [67] J. Wong. *Terramechanics and Off-Road Vehicles*. Elsevier Science Publishers, 1989.
- [68] P.G. Xavier. Shortest path planning for a tethered robot or anchored cable. *International Conference on Robotics and Automation*, pages 1101–1107, May 1999.
- [69] R. Yong, E. Fattah, and N. Skiadas. *Vehicle Traction Mechanics*. Elsevier Science Publishers, 1984.
- [70] L.C. Young. *Lectures on the Calculus of Variations and Optimal Control Theory*. W.B. Saunders Company, 1969.
- [71] Z. Zhang, R. Weiss, and A.R. Hanson. Qualitative obstacle detection. *IEEE Conference on Computer Vision and Pattern Recognition*, pages 554–559, 1994.